Chair of Applied Geophysics

Master's Thesis

Estimation of Reservoir Properties from Inversion of Electromagnetic and Seismic Data: Case Study from the Johan Castberg Area, Barents Sea, Norway

Nils Sondre Schlichting Olsson

June 2019

AFFIDAVIT

I declare on oath that I wrote this thesis independently, did not use other than the specified sources and aids, and did not otherwise use any unauthorized aids.

I declare that I have read, understood, and complied with the guidelines of the senate of the Montanuniversität Leoben for "Good Scientific Practice".

Furthermore, I declare that the electronic and printed version of the submitted thesis are identical, both, formally and with regard to content.

Date 04.06.2019

Sondre Olsson

Signature Author
Nils Sondre Schlichting, Olsson
Matriculation Number: 01601768


equinor

Preface

This thesis is submitted in partial fulfillment of the requirements for the degree "Master of Science (English)/Diplomingenieur (German)" (MSc/Dipl.-Ing) at the Montanuniversität Leoben (MUL). The thesis has been written in collaboration with Equinor (formerly known as Statoil) at the office in Oslo during the period October 2018 to May 2019. The purpose of the thesis was to investigate the feasibility of combining controlled-source electromagnetic inversion and acoustic seismic full waveform inversion in a petrophysical joint inversion to estimate reservoir properties in petroleum exploration.

Acknowledgment

A big thanks to Univ.-Prof. Dipl.-Geophys. Dr.rer.nat Florian Bleibinhaus for letting me write my thesis in collaboration with Equinor. First and foremost, I would like to thank my supervisor Prof. II. Dr. Ketil Hokstad and my co-supervisor Dr. Torgeir Wiik for generous and insightful support. Without their extraordinary help, this thesis would not have been possible. I would also like to thank the people at Equinor Oslo, especially Dr. Stig-Kyrre Foss, Dr. Hossein Mehdi Zadeh, Marit Stustad Guttormsen, Dr. Anders Sollid, Christopher Spjuth, Anne Olbeck and Bjørn-Arild Gressetvold for valuable discussions in the office. I would like to thank Equinor for the summer internship last summer that gave me this unique opportunity to work on a good and relevant problem based on high quality datasets, as well as letting me continue my thesis work in a new summer internship.

I am forever grateful for all the help from my family letting me study what I wanted and all their support. My family has played a crucial role in my success. Therefore, I dedicate this work to them.

Abstract

Most of the easy oil and gas have now been discovered, and as the petroleum exploration moves towards more frontier areas, it is more important than ever before to combine different methods in order to find the remaining oil and gas. Therefore, this thesis investigates the feasibility of combining controlled-source electromagnetic (CSEM) inversion and acoustic seismic full waveform inversion (FWI) in a petrophysical joint inversion workflow to estimate reservoir properties (fluid saturation and porosity) in petroleum exploration. This is thought to be a candidate to the next generation of reservoir characterization.

A Bayesian rock-physics inversion scheme is used in the joint inversion. Simple petrophysical relationships as Archie equation, Han's model and Gassmann equations are used in the forward model. The developed workflow of this thesis was first tested on synthetic models and afterwards tested on well log data and maps computed from 3D models of vertical resistivity and P-wave velocity from the Johan Castberg area in the Barents Sea.

The developed method shows that the water saturation and porosity could be estimated with high accuracy from synthetic models and well log data. Taking density into account as a third geophysical parameter, improved the inversion results for well log data, especially for the porosity. On the other hand, the method worked for the maps, but the quality of the results are not as good as for the well log data.

Bayesian inversion using a rock-physics inversion scheme shows reliable results for the synthetic models and well log data but the quality of the forward model and the input models of vertical resistivity and P-wave velocity, need to be improved before the results for the maps are reaching the quality of interest.

Keywords: *Full waveform inversion* ; *controlled-source electromagnetic inversion* ; *Bayesian joint inversion* ; *Johan Castberg Field* ; *petrophysics* ; *reservoir characterization.*

Kurzfassung

Da die Meisten einfach zu findenden Erdöl- und Gaslagerstätten bereits erforscht sind und die Erdölaufsuchung sich in immer kompliziertere Fördergebiete wagt, ist es wichtiger als je zuvor, verschiedene Methoden der Aufsuchung zu verknüpfen. Diese Arbeit schlägt eine kombinierte Inversion aus controlled-source elektromagnetischer (CSEM) Inversion und seismischer full waveform Inversion (FWI) vor, mit welcher gesteinsphysikalische Parameter besser abgeschätzt werden können. Diese Methode könnte in Zukunft für eine genauere Charakterisierungen von Lagerstätten verwendet werden.

Ein probabilistischer Bayesian Ansatz wird für die kombinierte Inversion verwendet. Einfache gesteinsphysikalische Beziehungen wie die Archie Gleichung, das Han´s Model und die Gassmann Gleichungen werden für die Vorwärtsmodellierungen verwendet. Der entwickelte Arbeitsablauf wird zuerst an synthetischen Modellen getestet und danach an echten Widerstands- und P-Wellengeschwindigkeitsdaten von Bohrlöchern aus dem Johan Castberg Gebiet in der Barentssee angewendet.

Die entwickelte Methode zeigt, dass Wassersättigungen und Porositäten, sowohl aus den synthetischen als auch den Bohrlochdaten, abgeschätzt werden können. Unter zusätzlicher Verwendung der Dichte als Eingabeparameter wird das Inversionsergebnis der Porosität für die Bohrlochdaten verbessert.

Die Bayessche Inversion zeigt sowohl für die synthetischen als auch die realen Daten vielversprechende Ergebnisse. Um das Inversionsergebnis zu verbessern, muss in Zukunft die Qualität der Eingabeparameter (P-Wellengeschwindigkeit und Gesteinswiderstand) sowie die Vorwärtsmodellierung verbessert werden.

Keywords: *Full waveform Inversion* ; *controlled-source elektromagnetischer Inversion* ; *Bayessche Inversion* ; *Johan Castberg Gebiet* ; *Petrophysik* ; *Reservoircharakterisierung.*

Contents

List of Figures

List of Tables

Nomenclature

β	Biot coefficient
ϕ	Porosity
ρ_b	Bulk density
ρ_g	Gas density
ρ_o	Oil density
ρ_w	Formation water density
ρ_{ma}	Matrix density
a	Turtousity factor
AI	Acoustic Impedance
AVO	Amplitude Versus Offset
BCU	Bottom Cretaceous Unconformity
BFC	Bjørnøyrenna Fault Complex
CSEM	Controlled-source electromagnetics
EM	Electromagnetics
F	Formation factor
Fm	Formation

FTG Full Tensor Gradiometry

FWI Full waveform inversion

GOC Gas Oil Contact

Gp Group

GWC Gas Water Contact

HC Hydrocarbon

K Bulk modulus

K_g Bulk modulus gas

K_o Bulk modulus oil

K_w Formation water bulk modulus

K_{dry} Bulk modulus dry rock

LFP Lithology Fluid Prediction

m Porosity exponent

MAP Maximum a posteriori

MCMC Monte Carlo Markov Chain

MGI Multi Geophysical Inversion

MLH Maximum likelihood

n Saturation exponent

NaN Not a number

NCS Norwegian Continental Shelf

NPD Norwegian Petroleum Directorate

OWC	Oil Water Contact
pdf	Probability density function
PL	Production Licence
PVT	Pressure Volume Temperature
R_h	Horizontal resistivity
R_o	Brine water resistivity
R_t	True resistivity
R_v	Vertical resistivity
R_w	Formation water resistivity
rv	Random variable
S_g	Gas saturation
S_w	Water saturation
SJI	Simultaneous Joint Inversion
SR	Source rock
V_p	P-wave velocity
V_s	S-wave velocity

Chapter 1

Introduction

1.1 Background and motivation

To locate and find hydrocarbon (HC) reservoirs without drilling exploration wells is of high importance for the industry. The exploration is moving into more complex geological areas and makes it more important to look for methods to complement the standard way of work. The standard method being used to solve this are seismic methods, but controlled-source electromagnetic (CSEM) methods have shown the last 15 years promising potential to be a good supplementary method (Ellingsrud et al., 2002). CSEM used in a marine setting, has grown from a technique used to predict plain fluid anomalies in non-complex geological environments, to a technique based on modeling and inversion used in complex geologically environments (Carazzone et al., 2005).

In the late 1990s, Statoil invented the use of CSEM for marine HC identification. The first couple of years starting in year 2000, were used as a test period. The next few years, was an early commercial period with some problems related to receiver calibration. After year 2007, the data quality became better and more advanced methodology (modeling/inversion) became available. During the last years, the data quality and inversion algorithms have been significantly better and is still improving fast (Buland et al., 2011).

The CSEM method can be used to differentiate a reservoir containing HC (high resistivity) and a reservoir containing saline fluids (low resistivity). The lateral extent and boundaries of HC bearing layers can be found with CSEM, and complements the structural information given by seismic (Ellingsrud et al., 2002). Even if the CSEM shows a highly resistive body, this does not necessarily indicate HC. CSEM interpretation has some pitfalls, where other sources than HC can give rise to high resistivity (false positive). Typical false positives could be salt, carbonates, source rocks (SR) or cemented sandstones (because of lost porosity). Stefatos et al. (2014) discuss examples from the Norwegian Sea where CSEM gave a false positive anomaly of highly resistive targets. Two of the wells drilled were dry and gave a negative picture of CSEM, because CSEM data were available before they drilled the dry wells. In this case, sabkha evaporite showed high resistivity (false positve), but the true positive interpretation is HC filled reservoir in erosional products near Bottom Cretaceous Unconformity (BCU) (Stefatos et al., 2014). This makes it clear that by trusting the CSEM data too much is not a good idea, because of all the pitfalls related to the method. In order to minimize the likelihood of introducing false positives, the combination with other geophysical methods such as seismic is then preferred. Figure 1.1 demonstrates this in an understandable way.

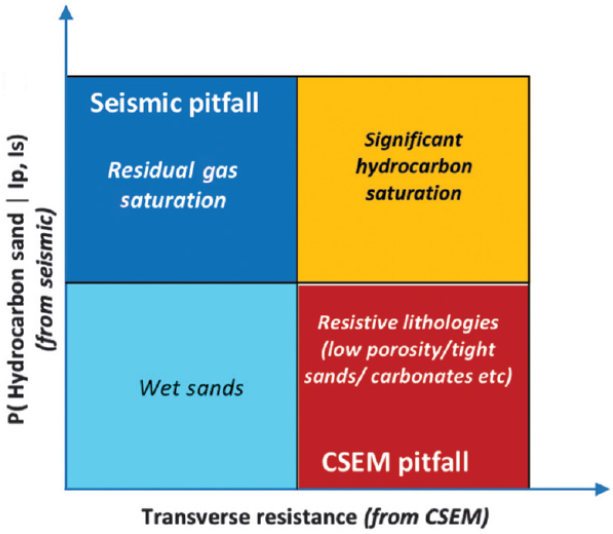

Figure 1.1: Electric/elastic crossplot showing the typical pitfalls of seismic and CSEM. The significant HC saturation is separated from the pitfalls of the two methods (Alvarez et al., 2018).

In general, to get the whole potential of a geophysical dataset, the data has to be combined with other geological and geophysical datasets. Seismic and electromagnetic data complements each other in terms of changes in rock fluid and lithology. The real advantage by doing joint inversion comes when the acoustic impedance from seismic inversion is combined with pore fluid resistivity information from CSEM inversion and would be important for reservoir appraisal and evaluation applications. For this reason, the methods seismic Amplitude Versus Offset (AVO) inversion and CSEM inversion were and still are, combined in order to make a joint petrophysical inversion for reservoir properties detection. This thesis will investigate the feasibility of combining acoustic seismic full waveform inversion (FWI) and CSEM inversion, and the idea is that, within 10 years, joint inversion of seismic AVO and CSEM is replaced by full elastic seismic FWI and CSEM inversion. The thesis will test this next generation of reservoir characterization using acoustic FWI instead of AVO inversion, as one step on the way towards the joint inversion of fully elastic FWI and CSEM inversion. The main purpose by doing this, is that FWI gives a better velocity model than AVO inversion. In the past, and at present, FWI has mainly utilized turning waves and refractions, with an acoustic seismic forward model. Currently a lot of research is done on elastic FWI, possibly including attenuation. Therefore, it is expected that within a few years, better seismic velocity models, with higher resolution, will be obtained by FWI. This gives a better and more precise estimate of the reservoir properties, because a more correct velocity model is used in the joint inversion, as well as that the limitations of each method can be overcome and the strength of each method exploited. This can be useful in terms of exploration, as well as during production. First and foremost, accurate velocity models are crucial for resolving prospectivity in complex geology. FWI is the most advanced data driven approach and is under continuous development and refinement in the industry. The business value is linked to reduced turnaround, improved imaging, shallow hazard identification and improved interpretation. It may, in other words, reduce the risk of drilling dry wells (save money), help to calculate the total volume of HC in charge and help to understand the reservoir even better and therefore also be a possible candidate to maximize the production.

Figure 1.2 shows why performing joint inversion based on velocities from FWI is an advantage. In seismic migration, the frequencies used are typically in the range of 10-60 Hz, while CSEM has frequencies between 0.1 and 15 Hz. This indicates that there is just a small overlap between the frequency contents of seismic and CSEM. At this point, FWI will be advantageous because it will fill this gap in frequencies between 2 and 10 Hz. This will give better velocity models for further work and is of big importance.

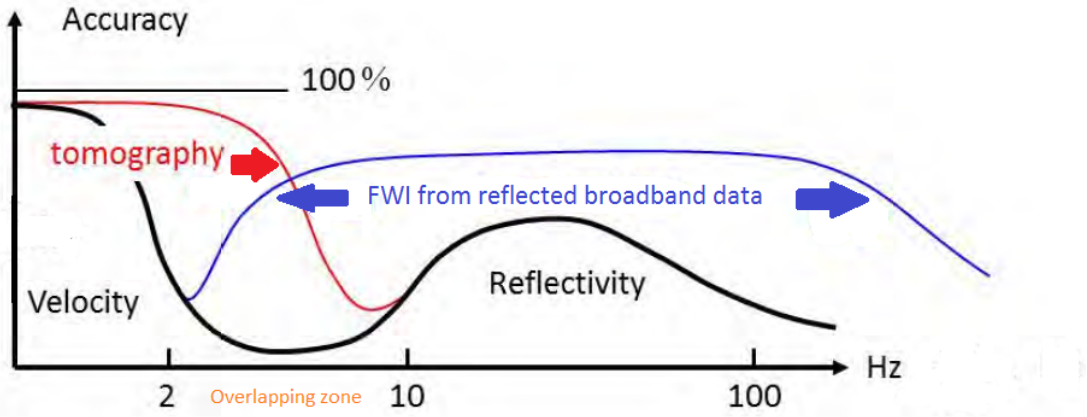

Figure 1.2: Illustration of resolution expected from velocity analysis (velocity), imaging (reflectivity), tomography and FWI from reflected broadband data. Tomography and FWI are filling the mid frequency range of 2 to 10 Hz and make up the overlapping zone. Along the x axis is the frequency, while the y axis shows the accuracy (modified after Claerbout (1985)).

The thesis will focus on the inversion for porosity and saturation. Other properties that can in principle be inverted for are net erosion/uplift, pressure, volume estimation, cementation, fracturing and 4D pressure versus saturation changes.

1.2 Research objectives

The main purpose with the thesis is to investigate the feasibility of using a combination of CSEM inversion and acoustic seismic FWI to estimate fluid saturation in petroleum exploration. The other reservoir property intestigated is porosity. The Johan Castberg area in the Barents Sea will be used as case area. The developed code will be tested on synthetic models, well logs data and map models computed from 3D cubes (from seismic FWI and CSEM inversion) in order to predict the most important reservoir properties.

1.3 Study area

An overview over the area status of the Norwegian Continental Shelf (NCS) as of June 2018 from the Norwegian Petroleum Directorate (NPD) is shown in Figure 1.3 (NPD, 2019b). The NCS consists of the North Sea, Norwegian Sea and Barents Sea. The Barents Sea is part of the Arctic Ocean and is located north of the Norwegian and Russian mainland, between the Norwegian Sea in the west, Novaya Zemlya and the Kara Sea in the east, Svalbard in the northwest and Franz Josef Land in the northeast (Dore, 1995).

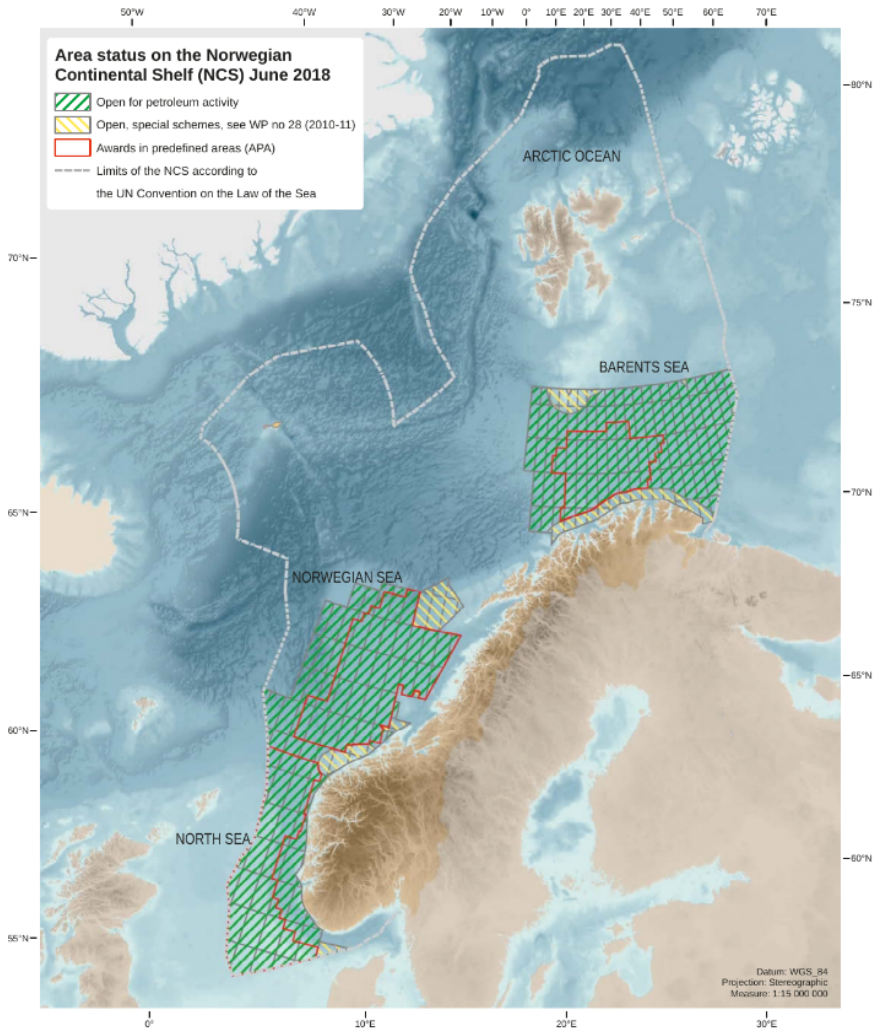

Figure 1.3: Area status of the NCS as of June 2018. The green areas represent areas open for petroleum activity, yellow areas are open, special schemes and the red areas are awards in predefined areas (APA). The grey dotted line is the border of the NCS (NPD, 2019b).

The study area is located in the Bjørnøya Basin in the southwestern Barents Sea, around 100 km northwest of the Snøhvit field. As for the Barents Sea in general, the study area has undergone uplift and erosion and this had a big influence on the amount of HC in the structures today. A lot of HC has leaked due to uplift and erosion, which means, unfortunately, that the potential was much higher some 10 million years ago. The potential to find big discoveries is still huge. A map showing the location of the Johan Castberg project is shown in Figure 1.4. The water depth here is between 360 and 390 m. It is part of the production license (PL) 532 and Equinor (50 %) is operator. The partners in PL 532 are Vår Energi (30 %) and Petoro (20 %). There is made several discoveries in the area, among them, the discoveries Skrugard and Havis that were discovered in 2011 and 2012, respectively. The proven volume estimates ranges from 400 to 650 million barrels of oil. The planned production start is in 2022 and will produce for 30 years (Equinor, 2018).

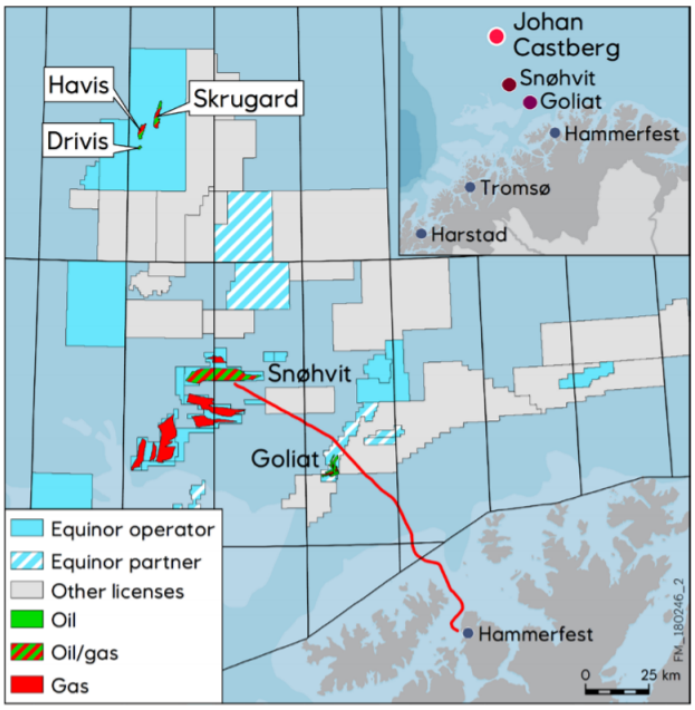

Figure 1.4: Geographical location of the Johan Castberg area with the different proven discoveries. Gas is marked with red and oil with green. The blue areas are Equinor operated (Equinor, 2018).

A 3D version of the Johan Castberg project is given in Figure 1.5, and shows the three discoveries Skrugard, Havis and Drivis.

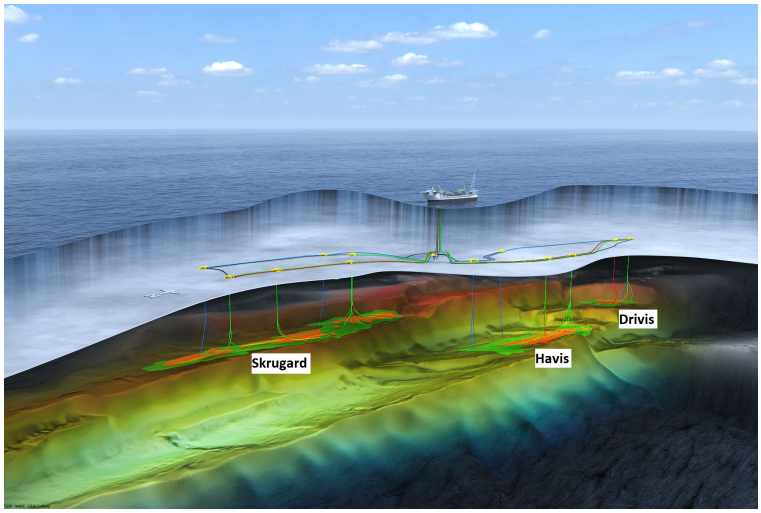

Figure 1.5: 3D view of the Johan Castberg Field in rotated fault blocks in the Bjørnøyrenna Fault Complex (BFC). The field development will consist of an Floating Production, Storage and Offloading (FPSO) and subsea structures (modified after Statoil (2017)).

Exploration activity in this area has shown prolific oil and gas plays (Upper Triassic to Middle Jurassic age) in the flank on the east side of the Bjørnøya Basin (well 7220/8-1, 7220/7-1 and 7220/7-3S). In other words, the Johan Castberg project. In the western part of the Loppa High (see Figure 2.1 for the location), karstified/fractured carbonate plays (Permian age) have been proven. A couple of discoveries are being made here (Gohta 7120/1-3 from 2013 and Alta 7220/11-1 from 2014) (Blaich et al., 2017). Due to restrictions, only the southern part (south of 74°30' N) is currently open for petroleum activities (Ohm et al., 2008). Figure 1.6 shows the locations of the three studied wells (7220/8-1, 7220/7-1 and 7219/9-1T2).

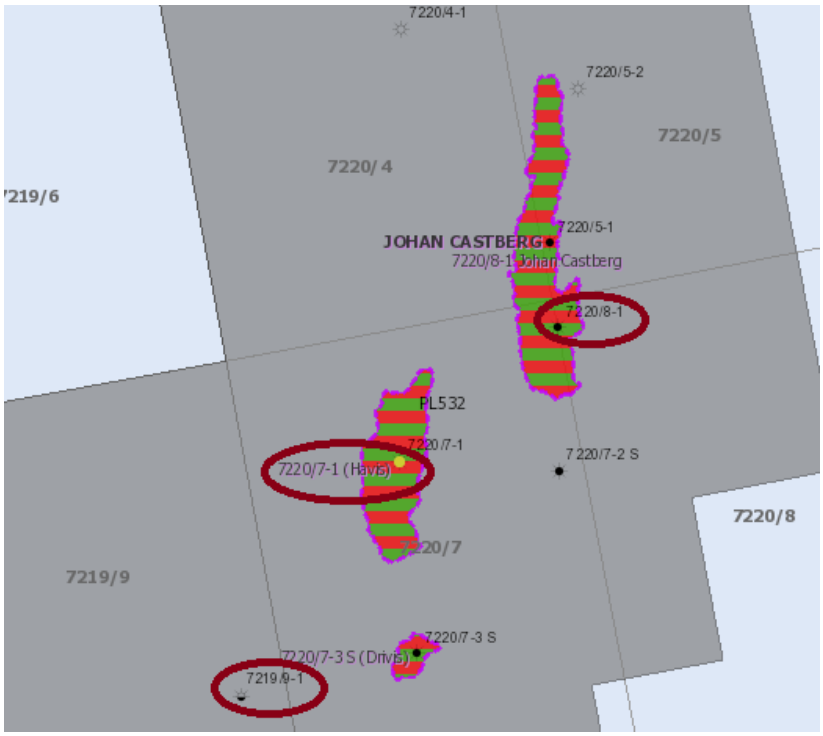

Figure 1.6: Location of the three wells taken into account in this study (modified after NPD (2019a)).

Proven discoveries, already mentioned, are Skrugard, Havis and Drivis. In October 2018, a new discovery in PL 532 was made by Equinor. The name of this discovery is Skruis (well 7220/5-3) and is located 8 km north of the 7220/8-1 discovery well (see Figure 1.7). The wildcat well proved oil. The primary exploration target was to prove the petroleum content in the Stø and Nordmela formations (Fm). Volume estimations so far indicate between 2 and 4 million standard cubic metres (Sm^3) of recoverable oil. It is a rather small discovery, but could still be economic attractive when the infrastructure is in place. The plan is that this can be linked up to the other proven discoveries, and then increase the Johan Castberg volumes (Statoil, 2018). This indicates the potential of the area and further exploration is recommended to do.

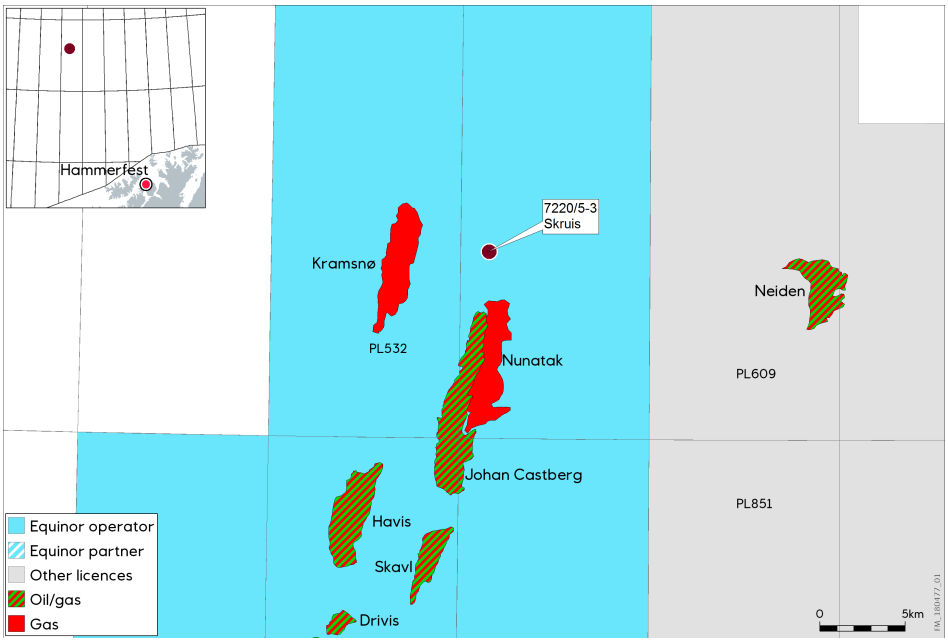

Figure 1.7: Location of the Skruis discovery. The plan is to tie it up to the Johan Castberg project in the south (Statoil, 2018).

As mentioned in the beginning, CSEM has a potentially high influence in petroleum exploration. Figure 1.8 shows vertical resistivity (R_v) anomalies together with the wells 7220/8-1 and 7219/9-1. It is clearly visible that the resistivity model shows that the well 7220/8-1 is drilled through a highly resistive anomaly, while well 7219/9-1 is not. Even if high resistivity areas are existing, in this case due to HC, there is no guarantee that it is always like this, as discussed by (Stefatos et al., 2014).

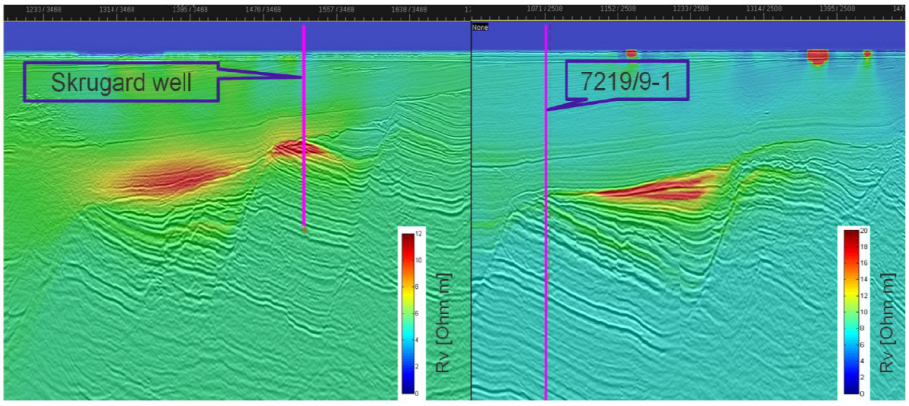

Figure 1.8: CSEM showing R_v anomalies of the Johan Castberg area. The Skrugard well (7220/8-1) drilled through a high resistive anomaly, while well 7219/9-1 was drilled off the anomaly (Nordskag et al., 2013).

A 3D view of the resistivity anomalies and the well positions are presented in Figure 1.9. A seismic line is included to show the geological structures.

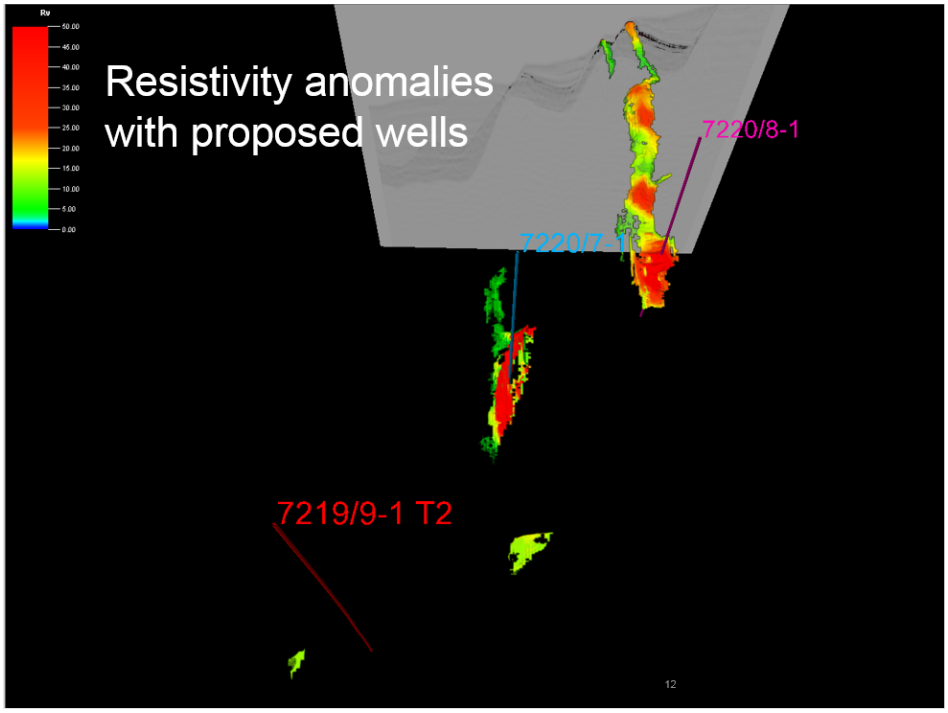

Figure 1.9: 3D visualization, showing the resistivity anomalies and the wells studied. In the background, a seismic section shows the big structures in the area (Statoil, 2013).

Figure 1.10 shows a seismic cross-section of Skrugard showing two flat spots (gas cap and oil leg) and gives a good example of flat spots.

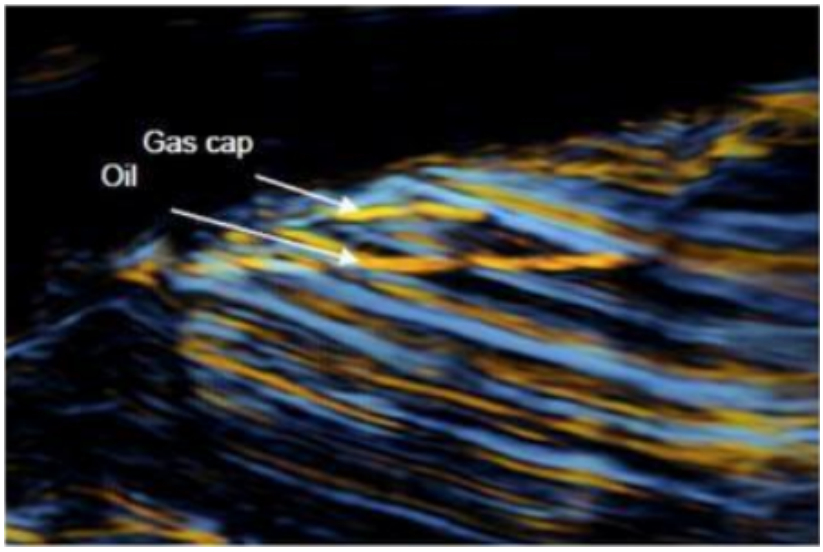

Figure 1.10: Skrugard seismic cross-section with flat spots (Statoil, 2013).

1.4 Database and software

The programming language Matlab was the only software used and was applied to develop the code.

An overview showing the most important information for the studied wells in the study area is given in Table 1.1. Table 1.2 gives an overview over the well logs being used. The wells 7220/8-1 (Skrugard) and 7220/7-1 (Havis) are proven discoveries, while well 7219/9-1T2 is dry. The reason for taking a dry well into account is to test the code on both discovery wells, as well as a dry well. The goal is to indicate HC zones in the discovery wells and indicate water saturated zones in the dry well. Maps computed from 3D cubes with FWI velocities and resistivities from CSEM inversion are provided based on work from Maaø et al and Wiik et al, respectively.

Table 1.1: General information of the studied wells (NPD, 2019a).

Facts	7219/9-1T2	7220/7-1	7220/8-1
NS degrees	72° 24' 0.78" N	72° 27' 37.53" N	72° 29' 28.92" N
EW degrees	19° 57'1.68" E	20° 9' 8.59" E	20° 20' 2.25" E
Year completed	1988	2012	2011
Content	Shows (Dry)	Oil/Gas	Oil/Gas
Purpose	Wildcat	Wildcat	Wildcat
(Discovery) name	-	Johan Castberg (Havis)	Johan Castberg (Skrugard)
Current activity status	-	Approved for production	Approved for production
1. level with HC, age	-	Middle Jurassic	Middle Jurassic
1. level with HC, formation	-	Stø Fm	Stø Fm
2. level with HC, age	-	Early Jurassic	Early Jurassic
2. level with HC, formation	-	Nordmela Fm	Nordmela Fm
GOC [m]	-	1828	1312
OWC [m]	-	1956	1395
Top Stø Fm [m]	1950	1781	1276
Top Nordmela Fm [m]	2062	1857	1354
Water depth [m]	356.0	365.0	374.0

Table 1.2: Well logs used. SOT = total oil saturation, SGT = total gas saturation, VCL = clay volume fraction, PHIT = total porosity, VP = P-wave velocity, RT = true resistivity, RW = formation water resistivity, RHOB = bulk density, RHOG = gas density, RHOW = formation water density, KFLW = formation water bulk modulus.

Well log	SOT	SGT	VCL	PHIT	VP	RT	RW	RHOB	RHOG	RHOW	KFLW

Chapter 2

Geological setting

2.1 Structure

The Barents Sea is located in the northwestern part of the Eurasian continental shelf. The Cenozoic opening of the Norwegian-Greenland Sea and the Eurasia Basin created passive margins in the western and northern part of the Barents Sea, while in the west, thick sequences of Upper Palaeozoic to Cenozoic rocks that consists of three separated regions were created. The regions are marked with the numbers 1-3 in Figure 2.1. The regions are the Svalbard Platform, a basin province between the Svalbard Province and the Norwegian Coast, and the continental margin. The Svalbard Platform contains flat-lying Triassic sediments. Highs and sub-basins characterize the basin province. In the basins, sediments of Jurassic-Cretaceous and Palaeocene-Eocene (in the west) age are preserved. Three major segments constitutes the continental margin (Senja Fracture Zone, rift complex southwest of Bjørnøya and Hornsund Fault Zone).

Three major rift phases occured in the western Barents Sea (Late Devonian-Carboniferous, Middle Jurassic-Early Cretaceous and Early Tertiary). Most of the Barents Sea was affected by crustal extension in Late Palaeozoic time. Continued extension gave westward rifting, and rift and pull-apart basins were developed in the southwest and strike-slip faults were developed in the north (Faleide et al., 2015).

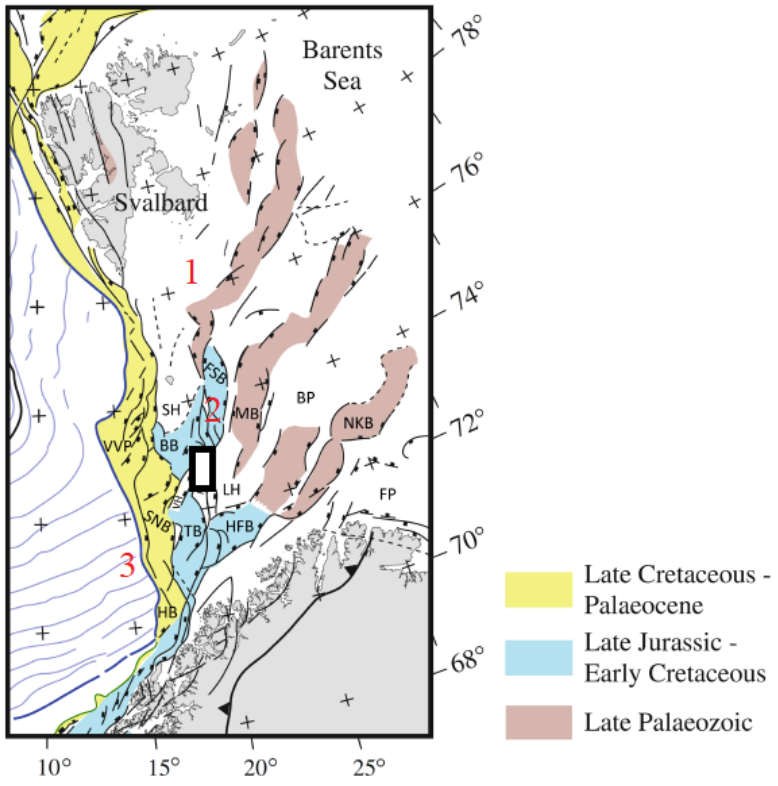

Figure 2.1: Major rifting events. The black rectangle indicates the study area (modified after Faleide et al. (2015)). The numbers 1-3 indicate the three main regions in the western Barents Sea. BB = Bjørnøya Basin, FSB = Fingerdjupet Sub-basin, SH = Stappen High, HB = Harstad Basin, BP = Bjarmeland Platform, MB = Maud Basin, VVP = Vestbakken Volcanic Province, NKB = Nordkapp Basin, LH = Loppa High, SNB = Sørvestsnaget Basin, TB = Tromsø Basin, HFB = Hammerfest Basin.

2.2 Southwestern Barents Sea

Figure 2.2 shows a reflection seismic profile of the southwestern Barents Sea. The main structural setting and mega-sequences of this part of the Barents Sea are visible on the section. The orientation of the profile is shown in the bottom right corner, which indicates a NNW-SSE orientation. The main tectonic elements shown here are of Late Paleozoic, Mesozoic and Cenozoic age. The interpretation of the section indicates that the Bjørnøya Basin is a big half-graben structure. In the southeast, the basin is bounded by the BFC (big boundary faults). To the northwest, it is bounded by the Knølegga Fault Zone. The orientation of the faults in the BFC and the Knølegga Fault Zone is dipping to the west (Blaich et al., 2017).

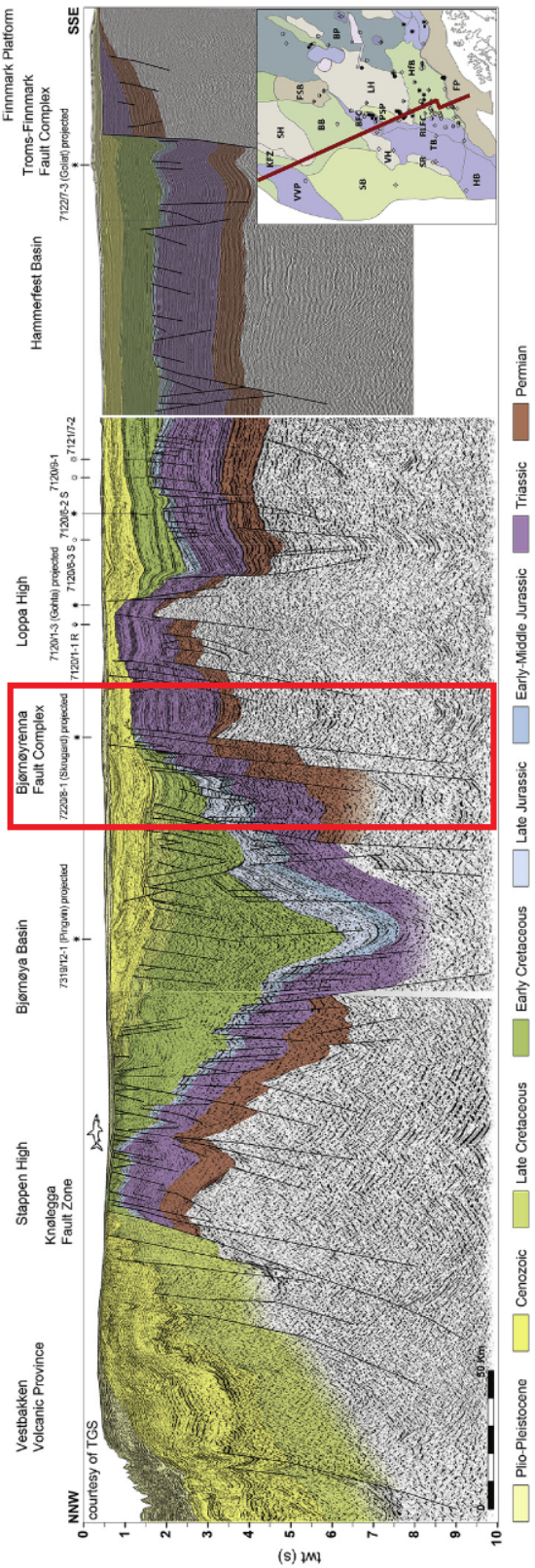

Figure 2.2: Seismic reflection profile and regional interpretation of the southwestern Barents Sea. Marked in red is the BFC with the Skrugard well. Modified after Blaich et al. (2017).

2.3 Uplift and erosion

In the Barents Sea, it has been difficult to find commercial quantities of HC, because of different uplift and erosion episodes from Paleocene (Ohm et al., 2008). The Barents Sea has experienced up to 3000 m of net erosion (difference between maximum burial depth and present day burial depth for a specific horizon), while the southwestern Barents Sea had a net erosion up to 1000-1500 m (Faleide et al., 2015). Uplift and erosion constitute big consequences for the petroleum systems. The processes affects many important petroleum system elements, among them, reservoir quality, maturity of the SR and the migration of HC. Due to changes in pressure volume temperature (PVT) conditions in a HC-filled structure, the processes will make the chances of leakage higher and the gas cap in the structure will expand. It has shown big importance to understand and know when the uplift and re-migration of the HC happened (Henriksen et al., 2011). Figure 2.3 shows how uplift and net erosion affect the petroleum system elements.

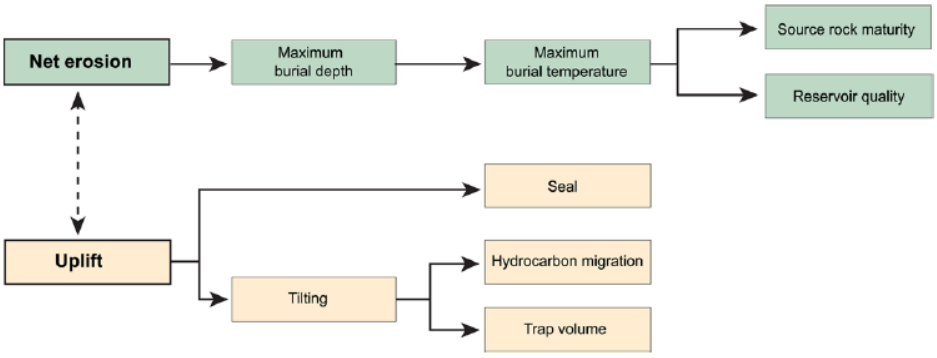

Figure 2.3: The connection between uplift and net erosion, and the elements that are important for petroleum prospectivity (Henriksen et al., 2011).

2.4 Reservoir formations

The Realgrunnen Group (Gp) consists of four formations (Fm), the Fruholmen Fm, Tubåen Fm, Nordmela Fm and Stø Fm. The two main reservoir formations in the study area are the Stø Fm and Nordmela Fm (Halland et al., 2013).

2.4.1 Stø formation

The main reservoir unit in the Johan Castberg area is the Stø Fm and is of early to middle Jurassic age (see Figure 2.4). It consists of sandy sequences and is located above the Nordmela Fm. It is mainly mature and contains moderately to well sorted sandstone. In between the sandstone, thinner layers of siltstone and shale can be found. The thickness vary and the formation is generally thickest in the southwest, while it shows a thinning to the east. The below lying Nordmela Fm follows the same thickness pattern. The whole Stø Fm can be divided into 3 depositional sequences. The formation sands were deposited in prograding coastal regimes, and various clastic coast lithofacies are visible. The siltstone and shale layers indicates regional transgressive episodes.

2.4.2 Nordmela formation

The minor reservoir target in the Johan Castberg area is the Nordmela Fm and is of early Jurassic age (see Figure 2.4). It consists of interbedded sediments containing siltstones, sandstones and claystone, as well as minor coal layers. Towards the top of the unit, the sandstones becomes more common. As for the Stø Fm, it thickens to the southwest. The dopositional environment was tidal flat to flood plain. The sandstone layers of the unit, represents estuarine and tidal channels (Dalland et al., 1988).

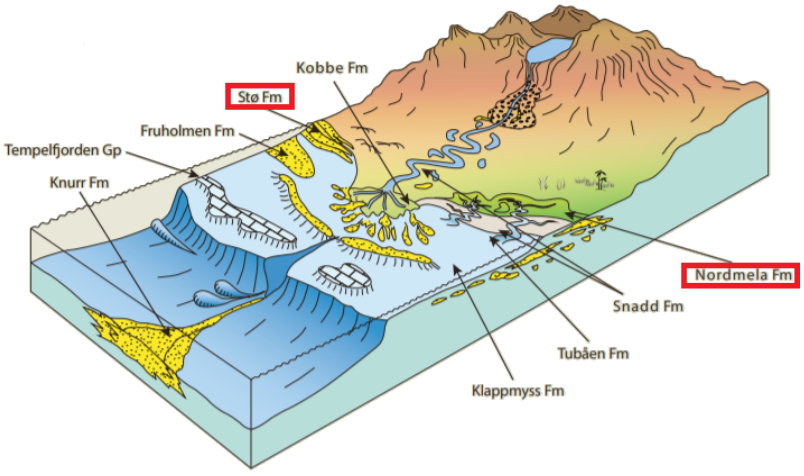

Figure 2.4: Depositional environments of the various reservoir formations in the southwestern Barents Sea. The main (Stø Fm) and minor (Nordmela Fm) reservoir targets are marked with red. Modified after Halland et al. (2013).

2.5 Stratigraphy

The lithostratigraphy in the western Barents Sea is presented in Figure 2.5. The Stø and Nordmela formations are marked in red. The Hekkingen Fm (shale) is the main SR and cap rock in the area and is marked in blue.

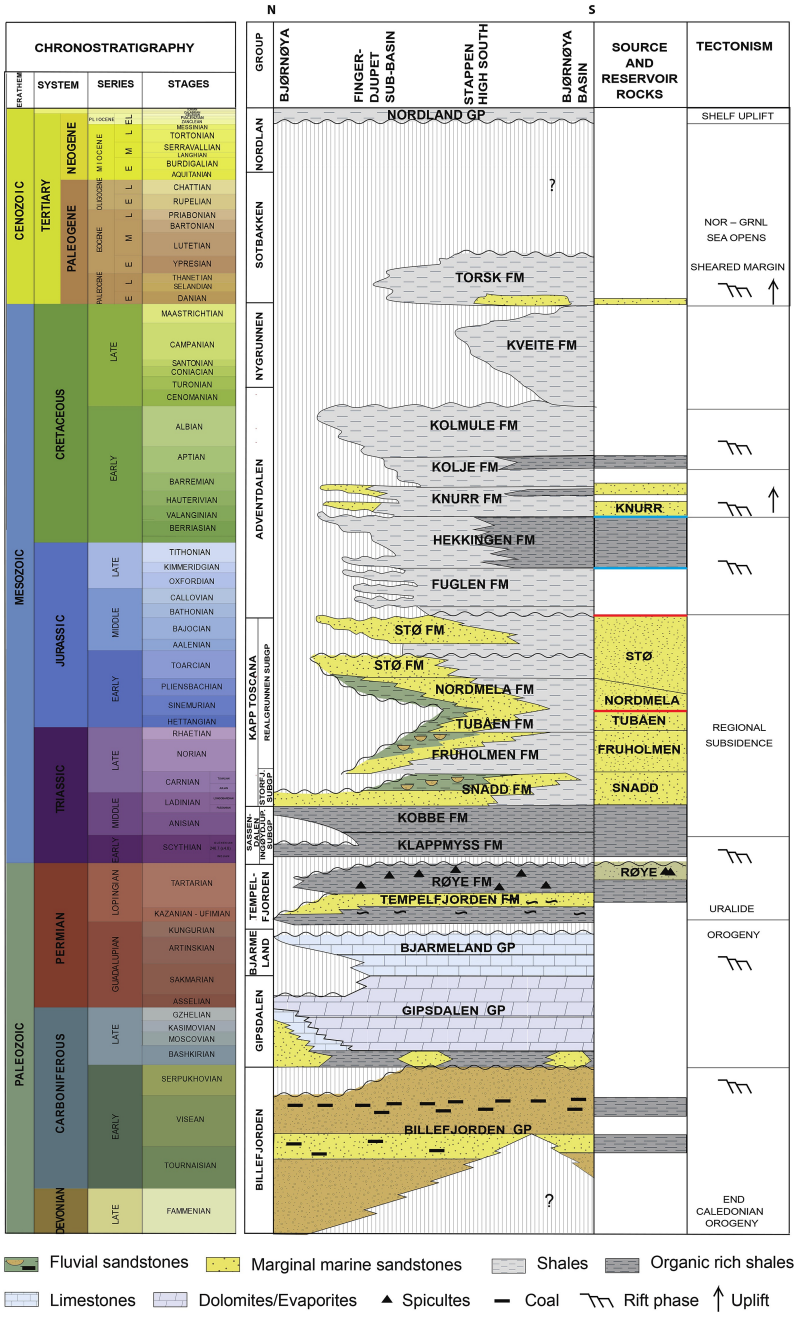

Figure 2.5: Lithostratigraphic column for the western Barents Sea. Marked in red are the Stø and Nordmela reservoir formations, and in blue the main source rock/cap rock the Hekkingen Fm. Modified after Blaich et al. (2017).

Chapter 3

Theory

3.1 Matrix-vector formulation of adjoint state

This section will deal with a joint theory part that is applicable for both seismic FWI and CSEM inversion. Both the forward problem and the inverse problem will be described. Vectors and matrices are marked with bold, to better see the difference between scalars and vectors/matrices.

3.1.1 The forward problem

Matrix notations are introduced to describe the partial-differential operators of the wave equation ((Marfurt, 1984); (Carcione et al., 2002)). The time domain formulation of the forward problem is given by

$$\mathbf{M}(\mathbf{x})\frac{d^2\mathbf{u}(\mathbf{x},t)}{dt^2} = \mathbf{A}(\mathbf{x})\mathbf{u}(\mathbf{x},t) + \mathbf{s}(\mathbf{x},t), \tag{3.1}$$

where the matrices **M** and **A** are mass density and stiffness for the elastic problem, and susceptibility and conductivity (inverse of resistivity) for the electromagnetic problem, while **u** (seismic/electromagnetic wavefield) and **s** (source term) are vectors. The time is given by t and the spatial coordinates are denoted by **x**. The wave equation consists, in the frequency domain, of a system of linear equations. In this case, the source is found on the right part of equation 3.2 and the solution is the wavefield.

The forward problem can be defined in the frequency domain as

$$\mathbf{B}(\mathbf{x},\omega)\mathbf{u}(\mathbf{x},\omega) = \mathbf{s}(\mathbf{x},\omega), \tag{3.2}$$

where **B** is the impedance matrix, ω is the angular frequency and is given by (Marfurt, 1984)

$$\mathbf{B} = \omega^2\mathbf{M} - \mathbf{A} \tag{3.3}$$

The matrices **M**, **A** and **B** contain the coefficients of interest in order to quantify the properties of the subsurface. The model parameters and the wavefield have a nonlinear relationship and can be connected through the operator in time or frequency domain as follows

$$\mathbf{u} = \mathbf{G}(\mathbf{m}), \tag{3.4}$$

where **G** is the operator and **m** is the model parameters.

3.1.2 Least-squares local optimization

The data misfit vector ($\Delta\mathbf{d}$) can be defined as

$$\Delta\mathbf{d} = \mathbf{d}_{obs} - \mathbf{d}_{cal}(\mathbf{m}), \tag{3.5}$$

by the differences at the receiver positions between the observed data ($\mathbf{d}_{obs}$) and the calculated data ($\mathbf{d}_{cal}$) for every pair of source and receiver in the survey. The model parameters are physical parameters of the subsurface.

3.1.3 Misfit function

It is now time to define a norm defined of the misfit vector and refer to it as the misfit function. The least-squares (L2) norm of the misfit vector is defined as

$$\Phi = \frac{1}{2}\Delta\mathbf{d}^H\Delta\mathbf{d}, \tag{3.6}$$

where Φ is the misfit norm and H is the transpose conjugate.

Equation 3.6 is a simplified misfit function without any weights or regularization (Tarantola, 1987).

3.1.4 Gauss-Newton - normal equations

The calculated data is defined as

$$\mathbf{d}_{cal} = \mathbf{F}(\mathbf{m}), \tag{3.7}$$

where **F** is the forward operator and is defined as

$$\mathbf{F}(\mathbf{m}) \simeq \mathbf{F}(\mathbf{m}_0) + \mathbf{J}\Delta\mathbf{m}, \tag{3.8}$$

where $\mathbf{m}_0$ is the initial model, $\Delta\mathbf{m}$ is the model misfit and **J** is the Jacobian matrix.
Now it is possible to find the misfit function expressed with the forward operator, by linearizing the forward model

$$\Phi \approx \frac{1}{2}(\mathbf{d}_{obs} - \mathbf{F}(\mathbf{m}_0) - \mathbf{J}\Delta\mathbf{m})^H(\mathbf{d}_{obs} - \mathbf{F}(\mathbf{m}_0) - \mathbf{J}\Delta\mathbf{m}) \tag{3.9}$$

The next step is to find $\mathbf{m} = \mathbf{m}_0 + \Delta\mathbf{m}$ such that $\frac{\partial\phi}{\partial\Delta\mathbf{m}} = 0$

$$\frac{\partial\phi}{\partial\Delta\mathbf{m}} = -\mathbf{J}^H(\mathbf{d}_{obs} - \mathbf{F}(\mathbf{m}_0) - \mathbf{J}\Delta\mathbf{m}) = 0 \tag{3.10}$$

The expression for Gauss-Newton is then given as

$$\mathbf{J}^H\mathbf{J}\Delta\mathbf{m} = \mathbf{J}^H\Delta\mathbf{d} \tag{3.11}$$

$$\mathbf{m}^{(n+1)} = \mathbf{m}^{(n)} + \Delta\mathbf{m} \tag{3.12}$$

The data is modeled up if $\mathbf{J}^H\mathbf{J}$ or $\mathbf{J}\mathbf{J}^H$ can be inverted as follows

$$\Delta\mathbf{m} = (\mathbf{J}^H\mathbf{J})^{-1}\mathbf{J}^H\Delta\mathbf{d} \tag{3.13}$$

$$\Delta\mathbf{m} = \mathbf{J}^H(\mathbf{J}\mathbf{J}^H)^{-1}\Delta\mathbf{d} \tag{3.14}$$

Equation 3.13 and 3.14 are expressed as least squares and minimum norm, respectively (Virieux and Operto, 2009).

3.2 Introduction to joint seismic full waveform inversion and controlled-source electromagnetic inversion

In the oil and gas exploration, as well as reservoir characterization and reservoir monitoring applications, both seismic and electromagnetics (EM) have played a crucial role. When dealing with formation evaluation, two of the most important aspects to evaluate are the porosity and fluid saturation (water/oil/gas) distributions in the reservoir. Due to improvements in rock physics, it is now possible to make a connection between seismic data and reservoir properties ((Gassmann, 1951); (Nur, 1992); (Wang, 2001)). Due to previous work from Archie (1942) and Waxman and Smits (1968), EM data has been become a standard tool for quantifying fluid saturations based on resistivity logs.
Seismic and EM represents differences in the fundamental physics and they are therefore sensitive to different physical parameters. The main idea behind the joint inversion is, by performing the joint inversion, make it possible to invert for different reservoir parameters at the same time. This will make the characterization of the reservoir even better compared to doing the inversions separately.

It exists two ways to combine the methods. In geophysics in general, inversion methods are often performed in order to extract the geophysical properties of the earth based on measurements. To combine seismic FWI and CSEM inversion is not a trivial thing to do, because the seismic FWI produce velocity and the CSEM inversion resistivity (elastic versus electric) (Harris

et al., 2009). One way to do the joint inversion, is to use petrophysical relationships to connect velocity and resistivity together (Hoversten et al., 2006). By using petrophysical approaches, such as the Archie and Waxman-Smits equations, makes it possible to connect resistivity, porosity and water saturation together, while the fluid substitution equations from Gassmann, makes the connection between velocity, porosity and fluid saturations. In practice, these relationships are derived from cores being analysed from the area of interest. That constitutes the main drawback of the joint petrophysical inversion approach.

One alternative approach is the cross-gradient approach. This was introduced by Gallardo and Meju (2003) and the method looks at the structural similarity between resistivity and seismic velocity for the region under investigation. A cross-gradient regularization is brought into the cost function. A minimum value of the cross-gradient will be found when the structural similarity between resistivity and velocity reaches their maximum.

3.3 Petrophysical relationships

3.3.1 Han's model

Han et al. (1986) found empirical regressions connecting velocities together with porosity and clay content. Those regressions were based on 70 consolidated sandstones from the Gulf Coast, with porosities from 3% to 30% and clay volume from 0% to 55%. Han found out that the velocities of clean sandstones can be connected empirically alone very accurate. On the other hand, when clay is present, the empirically correlation with porosity is quite poor, but gets very accurate if clay volume also gets involved in the regression. The regressions between P-wave velocity (V_p), S-wave velocity (V_s), porosity (ϕ) and clay volume fractions (C) for the confining stresses 5, 10, 20, 30 and 40 MPa, are summarized in Table 3.1. These relations can be used to relate velocity, porosity, and clay content empirically in shaley sandstones.

Table 3.1: Han's empirical relations between V_p and V_s in km/s with ϕ and C. This is valid for water saturated shaley sandstones and is determined from 70 samples.

Confining stress [MPa]	V_p regression	V_s regression
40	$V_p = 5.59 - 6.93\phi$-2.18C	$V_s = 3.52 - 4.91\phi$-1.89C
30	$V_p = 5.55 - 6.96\phi$-2.18C	$V_s = 3.47 - 4.84\phi$-1.87C
20	$V_p = 5.49 - 6.94\phi$-2.17C	$V_s = 3.39 - 4.73\phi$-1.81C
10	$V_p = 5.39 - 7.08\phi$-2.13C	$V_s = 3.29 - 4.73\phi$-1.74C
5	$V_p = 5.26 - 7.08\phi$-2.02C	$V_s = 3.16 - 4.77\phi$-1.64C

This gives the following equations for estimating velocities (V_p and V_s):

$$V_p = A_p - B_p\phi - C_p V_{cl}, \tag{3.15}$$

$$V_s = C_s - D_s\phi - E_s V_{cl}, \tag{3.16}$$

where A-E are constants depending on the confining stress (see Table 3.1).

There exists a couple of limitations concerning the regressions mentioned above:

- Even if the relations are empirical, they should extend to other consolidated sandstones as well. The most important result is that the clay content plays a crucial role in determining the velocity. The regression coefficients should be recalibrated from cores or logs from the study area.
- The regression coefficients are relatively stable above 10 MPa, but below they vary more.

3.3.2 Gassmann equations

Some of the most important equations to calculate the V_p and V_s velocities are presented below. The remaining equations can be found in Appendix C.

Equation 3.17 gives the density of the pore fluids as

$$\rho_{fl} = S_w \rho_w + S_{HC} \rho_{HC}, \tag{3.17}$$

where ρ_{fl} is the density of the pore fluids, ρ_w is the density of water, ρ_{HC} is the hydrocarbon density, S_w is the water saturation and S_{HC} is the hydrocarbon saturation ($S_{HC} = 1 - S_w$).
Bulk density is a simple volumetric average of the rock constituent densities and is closely related to porosity by

$$\rho_b = (1 - \phi)\rho_0 + \phi \rho_{fl}, \tag{3.18}$$

where ρ_b is the bulk density, ρ_0 is the density of mineral grains and ϕ is porosity (Castagna et al., 1993).
Thus, the assumptions of a homogeneous fluid, uniformly distributed throughout the pore space, allows the bulk modulus of the fluid mixture to be calculated via the Reuss average

$$K_{fl} = \left[\sum_{i=1}^{n} \frac{S_i}{K_i} \right]^{-1}, \tag{3.19}$$

where K_{fl} is the bulk modulus of the fluid mixture, K_i is the bulk modulus of the individual phases, and S_i is their saturation (Smith et al., 2003).
By modeling the dry rock as a porous elastic solid, then with great generality it is possible to write the dry rock bulk modulus as

$$K_{dry} = K_0(1 - \beta), \tag{3.20}$$

where K_{dry} and K_0 are the bulk moduli of the dry rock and mineral and β is Biot's coefficient (Krief et al., 1990).
A swap variant of the Gassmann equation is used in the thesis, where substitution of the fluid with Han's model as a brine reference is performed. The goal is to find the changes when one fluid is substituted with another fluid. One way to do this is to transform the moduli from the starting fluid saturation to the dry state, and then directly transform from the dry moduli to the new state of fluid saturation. By doing so, the dry-rock bulk modulus disapears.

The saturated-rock moduli K_{sat1} and K_{sat2} are written as two fluid bulk moduli K_{fl1} and K_{fl2} given by

$$\frac{K_{sat1}}{K_0 - K_{sat1}} - \frac{K_{fl1}}{\phi(K_0 - K_{fl1})} = \frac{K_{sat2}}{K_0 - K_{sat2}} - \frac{K_{fl2}}{\phi(K_0 - K_{fl2})}, \tag{3.21}$$

where K_{sat1} is the bulk modulus of the brine saturated rock, K_{fl1} is the bulk modulus of the brine, K_{sat2} is the bulk modulus of the HC saturated rock and K_{fl2} is the bulk modulus of the HC.

The velocities for P- and S-waves can be written as

$$V_p = \sqrt{\frac{K + \frac{4}{3}\mu}{\rho}}, \tag{3.22}$$

$$V_s = \sqrt{\frac{\mu}{\rho}}, \tag{3.23}$$

where V_p is the P-wave velocity, V_s is the S-wave velocity, K is the bulk modulus and μ is the shear modulus (Gassmann, 1951; Biot, 1956).

3.3.3 Archie's equation

Archie's law created the foundation for modern well log interpretation, because it connects borehole electrical resistivity measurements together with S_{HC}. It is a purely empirical equation describing electrical resistivity flow in clean (no clay), consolidated sandstones, with varying intergranular porosity. Archie's equation connects the *in-situ* electrical resistivity of a rock together with its porosity and brine saturation (Mondol, 2015).

The Archie equation can be written as

$$S_w^n = \frac{R_o}{R_t} = \frac{FR_w}{R_t} = \frac{aR_wR_t}{\phi^m}, \tag{3.24}$$

where a is turtousity, n is saturation exponent, m is the porosity exponent, R_o is resistivity of the water-saturated formation, R_t is the true resistivity, R_w is the water resistivity and F is the formation factor (Archie, 1942).

By solving equation 3.24 for R_t, it can be written as

$$R_t = \frac{aR_w}{\phi^m S_w^n} \tag{3.25}$$

To get the logarithmic resistivity, the following formula is used

$$logR_t = log(R_t) \tag{3.26}$$

Table 3.2 shows how to get the different parameters used in Archie's equation to calculate S_w.

Table 3.2: Sources of data for calculation of S_w by Archie's equation. Modified after (Mondol, 2015).

Parameter	Source
R_t	Deep resistivity tool
R_w	SP log. Calculated from water zone
ϕ	Neutron, density, sonic, nuclear magnetic resonance (NMR)
F	Guess
m	Measured in the lab. Guess.
n	Measured in the lab. Guess.

Winsauer et al. (1952) modified the formation factor after Archie (1942) to the following

$$F = \frac{a}{\phi^m} \tag{3.27}$$

The formation factor is a function of the porosity and permeability of the rock and is an expression of rock properties independent of the conductivity of the pore water. Typical values for m varies from 1 (porous rock) to 3 (very well cemented rock), where 2.0 is an average value (Archie, 1942). It expresses how much the pore network increases the resistivity. It is normally assumed to be independent on temperature. Keller (1982) showed that m depends on the lithology, porosity, age, the degree of compaction and degree of cementation. An increase in consolidation, compaction and cementation makes the irregularity of the grains higher. If the grains have a more angular shape, m will increase (Salem and Chilingarian, 1999).

The saturation exponent gives information on the dependency on the presence of non-conductive fluids (like HC) in the pore-space, and is related to the wettability of the rock. Rocks that are water-wet will, for low S_w values, get a continuous film along the pore walls and makes the rock conductive. Oil-wet rocks will have non-continuous droplets of water within the pore space, and therefore the rock gets less conductive. Typically, the values are close to 2 (Mondol, 2015).

3.3.4 Waxman-Smits equation

The Waxman-Smits formula (Waxman and Smits, 1968) is given as

$$\sigma = \frac{1}{F}(\sigma_w + BQ_v), \tag{3.28}$$

$$B = 4.6\left(1 - 0.6e^{-\sigma_w/1.3}\right), \tag{3.29}$$

$$Q_v = \frac{CEC(1-\phi)\rho_0}{\phi}, \tag{3.30}$$

where CEC is the cation exchange capacity, B is the average mobility of the ions, Q_v is the charge per unit pore volume and σ_w is the water conductivity. CEC is a measure of the excess charges. In general, clays have a negative electrical charge within the sheet-like particles. Positive counterions at the outside surface compensates for this negative electrical charge and is a property of the dry clay mineral (Clavier et al., 1984).

3.4 Sensitivity of seismic and controlled-source electromagnetics

After giving some theory about velocity and saturation, Figure 3.1 shows some important aspects about the sensitivities of CSEM and seismic. It indicates that CSEM has high sensitivity for low S_w (high S_{HC}), while seismic has high sensitivity for high S_w (low S_{HC}). CSEM and seismic have their high sensitivities in each end of the S_w scale, and therefore, compliments each other. None of the methods have high sensitivity for S_w between 30% and 80%.

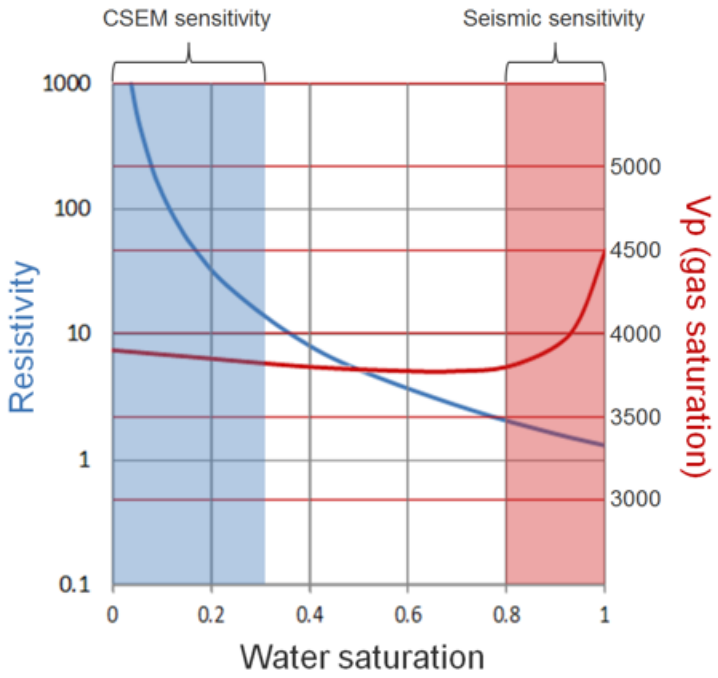

Figure 3.1: Connection between the Archie and Gassmann equations. None of the methods can determine medium high S_w in a good way (modified after Constable (2010)).

3.5 Transverse resistance

One important parameter to have in mind when interpreting the CSEM models, is the transverse resistance, given by

$$TR = \sum_{i=1}^{n} h_i R_i, \tag{3.31}$$

where TR is the transverse resistance, h is the thickness of the layer and R is the resistivity. The unit is Ωm^2. From equation 3.31, it is clear that it is not possible to distinguish between a thin high resistive layer and a thick low resistive layer, and is a main drawback (Zohdy et al., 1974).

3.6 Well logs

Logging is a method to record the rock properties in a well. A borehole is measured by pulling a tool into the well bore after the drilling has completed. There exists many types of well logs and some are being used even while drilling (Bjørlykke, 2015). A short description of the logs used in the thesis are presented. Only LFP-logs are being used. The LFP-logs have been through petrophysical modifications and are being proved by the petrophysicists. The details here are being omitted. The porosity, saturation and shale volume are calculated from other logs and not being measured directly by logs in the well. Only resistivity, density and velocity well logs are being described.

3.6.1 Resistivity

Resistivity is normally easy to measure and has the unit Ωm. The well log R_w measures the resistance of the formation water in the rocks, while R_t measures the resistivity of the rock partly saturated with formation water. By knowing the resistivity of the mud used while drilling, it is possible to calculate the porosity from the resistivity of the rock which is invaded by the drilling mud. Water has a much lower resistivity than oil and gas. That is why resistivity logs are used to find the oil water contact (OWC), gas water contact (GWC) or gas and oil contact (GOC).

3.6.2 Density

The density logs measure the density of both the rocks and their pore fluid and the unit is g/cm^3. Gamma rays from either cobolt-60 or cesium-137 are being used and the attenuation of the gamma rays collided with the electrons are being measured. This gives indications of how high the electron density is and is closely related to the density of the rock. By knowing the density of the formations, it makes it possible to identify different lithologies. By knowing the density of the minerals, bulk rock density and fluid density, the porosity can be found. The density of gas is given by ρ_g, density of formation water is ρ_w and ρ_b is the bulk rock density.

3.6.3 Velocity

A probe is lowered into the wellbore and sends out acoustic pulses that travel through the rock around the well and ends up in the other end of the probe. The velocity is calculated from the interval transit time (time the pulses use to travel the distance). The velocity is the inverse of the interval transit time and has the unit m/s. The velocity measured (V_p and/or V_s), depends a lot on the porosity (inversely proportional). The reason for this is that the velocity in porewater is significantly lower than in the rock matrix, but is not always the case. When the rock is cemented, the velocity is high even if the porosity is high too (Bjørlykke, 2015).

3.7 Basic statistics

This chapter is based on the book of Devore and Berk (2012).

3.7.1 Probability density function

A probability density function (pdf) of X is a function such that for any two numbers a and b with $a \leq b$,

$$P(a \leq X \leq b) = \int_a^b f(x)\,dx \tag{3.32}$$

3.7.2 Mean

The mean value of a continuous random variable (rv) X with pdf $f(x)$ is expressed as

$$\mu = \int_{-\infty}^{\infty} x f(x)\,dx, \tag{3.33}$$

where μ is the mean.

3.7.3 Variance

The variance of continuous rv X with pdf $f(x)$ and mean value μ is defined as

$$\sigma^2 = \int_{-\infty}^{\infty} (x-\mu)^2 f(x)\,dx, \tag{3.34}$$

where σ^2 is the variance.

3.7.4 Standard deviation

The standard deviation is defined as

$$\sigma = \sqrt{\int_{-\infty}^{\infty} (x-\mu)^2 f(x)\,dx}, \tag{3.35}$$

where σ is the standard deviation.

The standard deviation is the same as the square root of the variance and is a measure of the spread of the data. The standard deviation is an estimator for the variance for a given data set.

3.7.5 Normal distribution

A continuous rv X has a normal distribution with parameters μ and σ, where $-\infty < \mu < \infty$ and $0 < \sigma$, if the pdf of X is

$$f(x;\mu,\sigma) = \frac{1}{\sqrt{2\pi\sigma}} e^{-\frac{(x-\mu)^2}{(2\sigma^2)}}, \tag{3.36}$$

where $-\infty < x < \infty$. The statement that X is normally distributed with parameters μ and σ^2 is often abbreviated $X \sim N(\mu,\sigma^2)$.

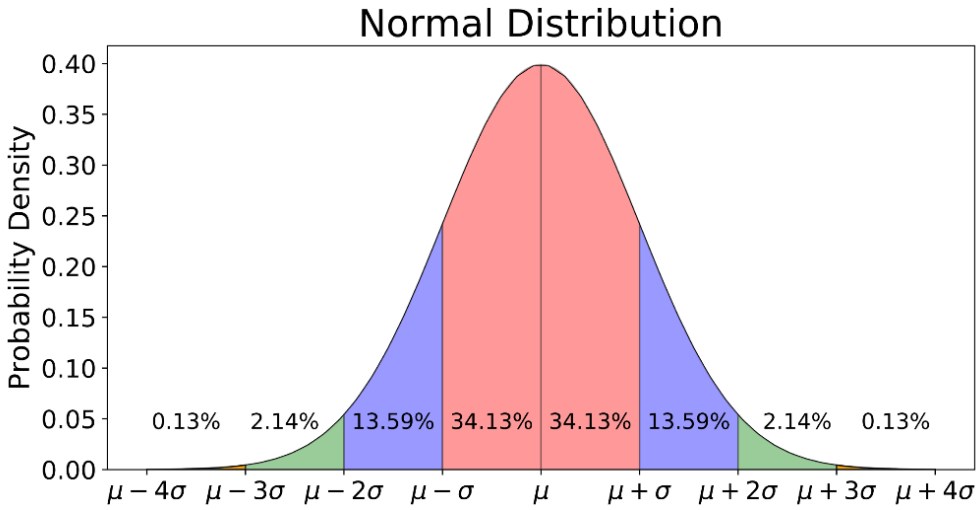

Figure 3.2: Normal distribution with the corresponding standard deviations. The pink, purple and green areas are the 1σ, 2σ and 3σ, respectively.

In this case,

- Around 68% of the values are within 1σ of the mean.
- Around 95% of the values are within 2σ of the mean.
- Around 99.7% of the values are within 3σ of the mean.

3.7.6 Marginal distribution

The probability of an event defined only by X, is given by the marginal pdf of X

$$f_X(x) = \int_{-\infty}^{\infty} f(x,y)\,dy, \tag{3.37}$$

where $-\infty < x < \infty$. Similarly the marginal pdf of Y is

$$f_Y(y) = \int_{-\infty}^{\infty} f(x,y)\,dx, \tag{3.38}$$

where $-\infty < y < \infty$.

3.8 Bayesian inversion

A and B represents two different events. The discrete probability of the events are given by $P(A)$ and $P(B)$. The probability that both A and B are happening, constitutes the Bayes' theorem, and is formulated as

$$P(A,B) = P(A|B)P(B) = P(B|A)P(A), \tag{3.39}$$

where $P(A|B)$ and $P(B|A)$ are both conditional probabilities. $P(A|B)$ is the probability of A happening, given that B has already happened and $P(B|A)$ is the probability of B happening, given that A has already happened.

Based on equation 3.39, it is possible to write Bayes' theorem even more simple as

$$P(B|A) = \frac{P(A|B)P(B)}{P(A)}. \tag{3.40}$$

Bayes' theorem (equation 3.40) can be formulated based on pdf's given as

$$p(X|m) = \frac{p(m|X)p(X)}{p(m)}. \tag{3.41}$$

The pdf $p(X)$ is called the prior pdf and symbolizes the probability of the property X independent of the given models. In other words, it gives the information on the property prior to the joint inversion. The assumption is that the property is linear and has a Gaussian distribution $N(\mu,\sigma^2)$ (Sen and Stoffa, 1996). The factor $p(m|X)$ is called the likelihood function. Before the joint inversion, $p(m|X)$ is the pdf related to possible model realizations for a fixed X. After the joint inversion being performed, $p(m|X)$ has an another meaning. It is the likelihood of getting the property as a function of the parameter vector X (posterior result). In other words, Bayes's rule is a powerful tool to update the knowledge at a given time with new measurements. The joint connection of CSEM and seismics are done when calculating the product of the likelihoods of resistivity and P-wave velocity. Maximum likelihood (MLH) is a point estimation of the likelihood function and gives the maximum of the likelihood function.

The factor $p(X|m)$ is the posterior pdf. This factor is the distribution of the property parameters posterior to the model m, or in other words, the probability that the property is correct given a

set of models m. By finding $p(X|m)$, it is the same as answering "What is the probability that the property is correct, given a certain set of models?". The probability of the models m, is a constant, and make it possible to write $p(m) = \int p(m|X)p(X)dX$ to make sure that $p(m)$ integrates to one (as it should for pdf's). Maximum a posteriori (MAP) is a point estimation of the posterior distribution and finds the maximum of the posterior distribution (which equals the mean of the posterior distribution), is given by

$$MAP = argmax_X p(X|m), \tag{3.42}$$

where argmax is the maximum argument of X given m (Ulrych et al., 2001).
By looking at equation 3.41, it is easy to see that the posterior pdf is the product of the likelihood function(s) and the prior pdf. For a uniform prior pdf, the posterior pdf is obtained mainly by the likelihood function. In some rare situations, it is possible to have a situation where the prior pdf will dominate the likelihood function and have the biggest influence on the posterior pdf. In general, the prior pdf dominates a subspace of the parameter space, while the likelihood function dominates other (and usually larger) subspaces (Sen and Stoffa, 1996).

Figure 3.3 and 3.4 show the relation between the prior, likelihood and posterior. It is clearly visible that the posterior (green) is proportional to the product of the prior (red) and the likelihood (blue). Figure 3.3 also shows that the variance of the prior distribution is the uncertainty, and the variance of the likelihood function is the noise in the models obtained. Figure 3.4 shows the relationship between the higher probability distributions and the multivariate normal distributions (contour lines).

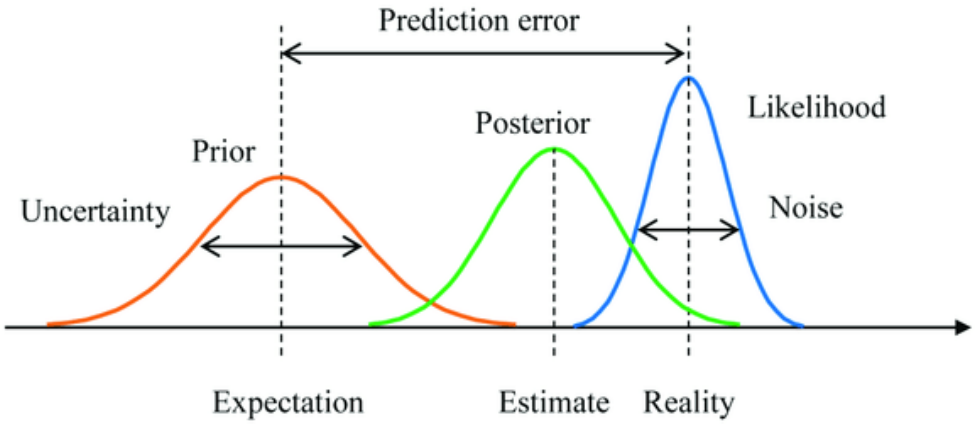

Figure 3.3: A prior distribution, likelihood function and posterior distribution are shown. The difference between the prior expectation and the peak of the likelihood function is known as prediction error. The uncertainty of the prior distribution is the same as the variance, while noise is the variance of the likelihood function (Yanagisawa et al., 2019).

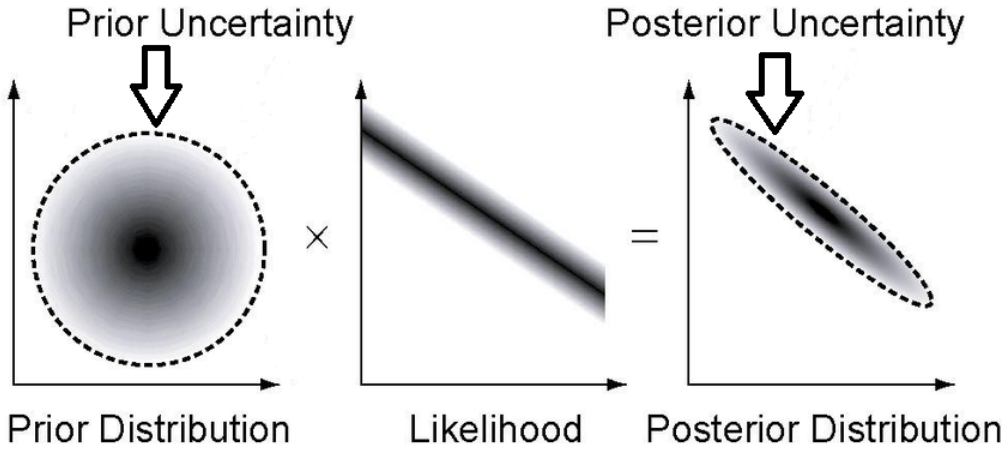

Figure 3.4: The product of prior distribution and likelihood function gives the posterior distribution, which defines uncertainty as soon as both prior information and models are taken into account. Higher probability distributions are marked with darker areas, while the dashed lines are the contours of the multivariate normal distributions. Modified after Malinverno et al. (2002).

Chapter 4

Methodology

4.1 Workflow

A statistical model (see Figure 4.1) is made for the dependence of geophysical model parameters on fluid saturation and porosity, as well as the dependence of geophysical data on geophysical model parameters (CSEM and seismic).

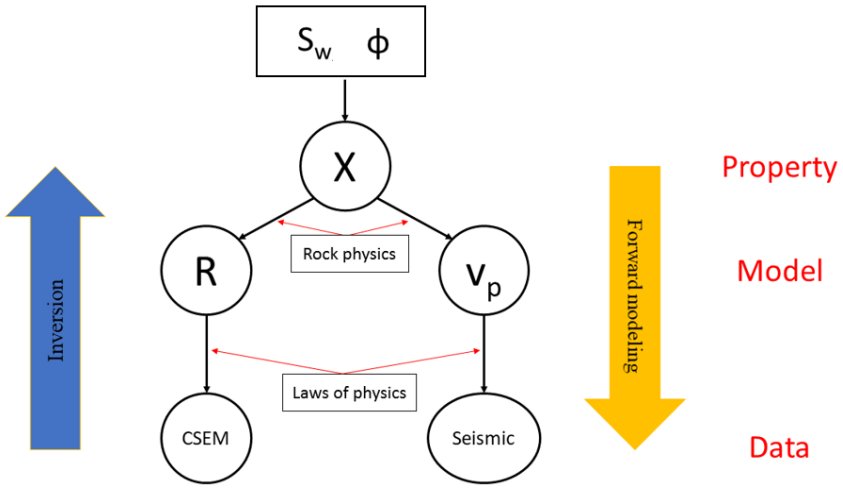

Figure 4.1: The workflow used for the computed maps (from the cubes) as a Bayesian network representing petrophysical joint inversion of resistivity (R) and velocity (V_p). X is the property being inverted for (fluid saturation and porosity in this case). The input to the Bayesian network are CSEM and seismic data. The inversion of these data gives the models of resistivity and velocity. The joint inversion of these models gives the properties. The forward modeling of the properties is based on rock-physics, while the forward modeling of the models is based on laws of physics (modified after Hokstad et al. (2017)).

A bayesian framework is chosen in order to account for the model uncertainty and the main idea behind this algorithm is that every node in the Bayesian network, has a specific probability and is conditional independent.
There is conditional independence between the different data types (seismic and CSEM), because it is possible to assume that the noise in the different data sets are independent. That means, the different data types meets on the node they are conditional on at the top of the network. For example, the noise in the CSEM data is independent from the noise in the seismic data collected some years earlier. This is a reasonable assumption and the only assumption needed to be taken to get the Bayesian network. Bayesian networks have also other applications, such as medical diagnostics, artificial intelligence and machine learning. The algorithm is very powerful and has a wide range of applications. This thesis will use the simplest version, called naive Bayes. That means, applying the Bayes' theorem with the naive assumption of conditional independence between the different data types.

The dependency between the properties and models can be summarized as

$$X = (S_w, \phi, V_{cl})$$
$$V_p(S_w, \phi, V_{cl})$$
$$R(S_w, \phi, V_{cl})$$
$$\rho(S_w, \phi, V_{cl}),$$

which shows the dependencies between properties and models, where V_{cl} is the clay volume.

Before going further, there are some important terms that need more focus. The inversion result of the measured data are models. The inversion of the models are properties. The forward modeling of the properties are models. The misfit between measured properties (from well logs) and properties found by inversion is the property misfit. The misfit between the models from inversion of the data and the models from the forward modeling of the properties is the model misfit. This means that velocity, resistivity and density depend on saturation, porosity and clay content. This is the whole idea behind the joint inversion, namely that it is possible to invert jointly, because the models and properties depends on each other. If this was not the case, it would not be possible to do joint inversion either. In the thesis, V_{cl} is considered deterministic,

while ϕ and S_w are considered stochastic.

The first set of dependencies are based on petrophysical relations (forward modeling). The 2nd set of dependencies comes from differential equations like Maxwell equations of electromagnetics (CSEM inversion) and the elastic wave equation (seismic FWI). These dependencies are indicated in Figure 4.1.
When moving from the top to the bottom of the Bayesian network, forward modeling is being performed. Synthetic geophysical models and data are computed (given saturation and porosity distributions). The interesting part is the inversion part (going from the bottom to the top). The purpose of inversion, is to calculate the model parameters and the properties (saturation and porosity), based on the measured geophysical data (Hokstad and Tänavsuu-Milkeviciene, 2017). By performing CSEM measurements, the magnitude and phase of the electromagnetic field is being measured. On the other hand, measurements done with seismics, measure the traveltimes the seismic waves use to travel their pathways. Performing inversion of the CSEM data, the starting point is magnitude/phase information of the electromagnetic field and the result is resistivity contrasts, while inversion of the seismic data, the traveltimes are resulting in velocity. From CSEM inversion and seismic FWI (the data), models of resistivity and velocity, respectively, are obtained. The inversions for CSEM and seismic are done separately. In comparison, the petrophysical joint inversion, going from models to properties, is performed simultaneously as Simultaneous Joint Inversion (SJI).

The first stage, is to invert geophysical data and create geophysical models (going from measured data to model parameters). The second stage, is to estimate the reservoir properties as fluid saturation and porosity by inversion of the geophysical model parameters (result of the first inversion). This second stage is actually a petrophysical (rock physics) inversion, given as a statistical inversion scheme. In the petrophysical joint inversion, Bayes' theorem (equation 3.39) is used as the main equation. The first step in the petrophysical joint inversion is to define the prior distributions for the reservoir properties (saturation and porosity). Then the maximum likelihood function is calculated and, finally, the posterior distributions of the properties are calculated. In this context, the first stage in the Bayesian network consist of the CSEM inversion and seismic FWI, and the outputs from this geophysical inversion are used as inputs for

the second stage statistical petrophysical inversion (going from models to parameters) (Hokstad et al., 2017).

Figure 4.2 presents the workflow presented in Figure 4.1 from another point of view and summarize the above mentioned workflow.

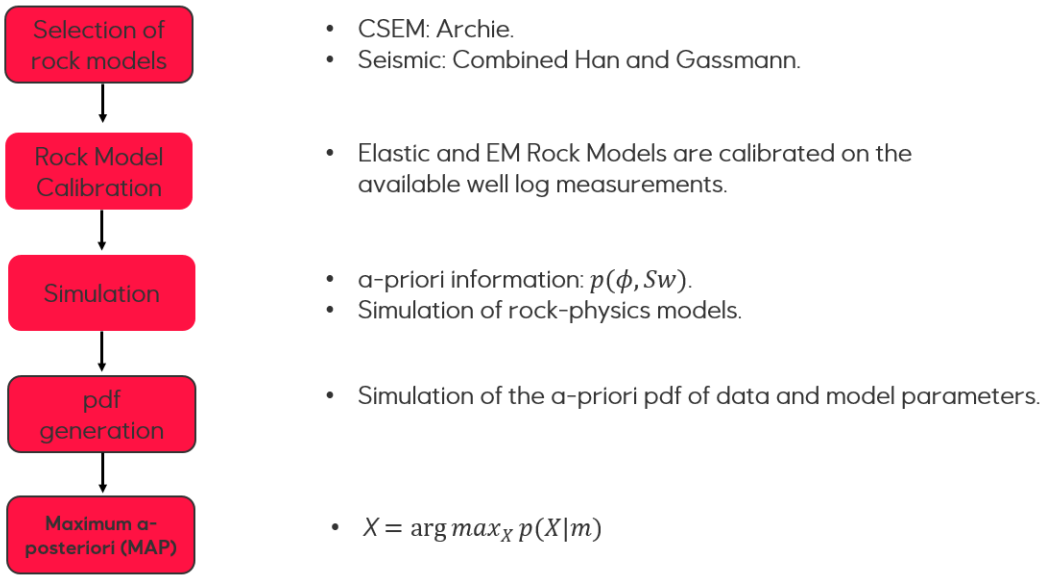

Figure 4.2: Workflow showing the 5 main steps in the Bayesian joint inversion.

Recalling the Bayes' theorem (equation 3.41), it can be written for the properties ϕ and S_w, as

$$p(\phi, S_w|m) = \frac{p(m|\phi, S_w)\,p(\phi, S_w)}{p(m)} \tag{4.1}$$

From the Bayesian network in Figure 4.1, the posterior distribution for X (S_w or ϕ), given one or more geophysical model parameters m_i, can be written as

$$p(X|m_1, ..., m_n) = C \prod_{i=1}^{n} p(m_i|X)\,p(X), \tag{4.2}$$

where C is the normalisation factor, and $p(X)$ is the prior distribution for X (S_w or ϕ) (Cowell et al., 2007; Lundteigen and Rausand, 2008).

The expressions for both the posterior μ and σ^2, are given in equation 4.3 and 4.4

$$\mu_{X|m_i} = \int X p(X|m_i) dX \tag{4.3}$$

$$\sigma^2_{X|m_i} = \int (X - \mu_{X|m_i})^2 p(X|m_i) dX \tag{4.4}$$

In this setting, $m_i = \{R_v, V_p\}$. By assuming Gaussian errors ($e = F_i(X) - m_i$), each of the likelihood functions $p(m_i|X)$ on the right side of equation 4.2, can be formulated as

$$p(m_i|X) = \frac{1}{\sigma_{ei}\sqrt{2\pi}} e^{\frac{-[m_i - F_i(X)]^2}{2\sigma^2_{ei}}} \tag{4.5}$$

where σ_{ei} is the error variance for model parameter m_i, and $F_i(X)$ are petrophysical (rock-physics) models connecting the S_w or ϕ to geophysical model parameters. It is important to note that petrophysical (rock physics) models are forward models. One or more geophysical parameters can be used to calculate the posterior distribution for X. The product of two (or more) likelihood functions creates the posterior distribution more narrow, and gives better posterior mean and smaller variance. It is always a question about how to do the relative weighting of the inversion parameters in the inversion, and the error variances of the posterior distribution can also be used to decide this relative weighting (Hokstad et al., 2017).

In this thesis, the focus has been on the rock-physics inversion, and FWI and CSEM inversions done by Equinor are being used directly without any further work.

All though not strictly correct, Equinor is using a pragmatic approach to the full joint inversion problem, by handling the FWI and CSEM inversions and the rock-physics inversion as separate steps. Then inversion models obtained from different service providers and using different methods can be combined in the rock-physics inversion, giving fast project turn around. An overview showing the typical prior information, data/model types and posterior results are shown in Figure 4.3.

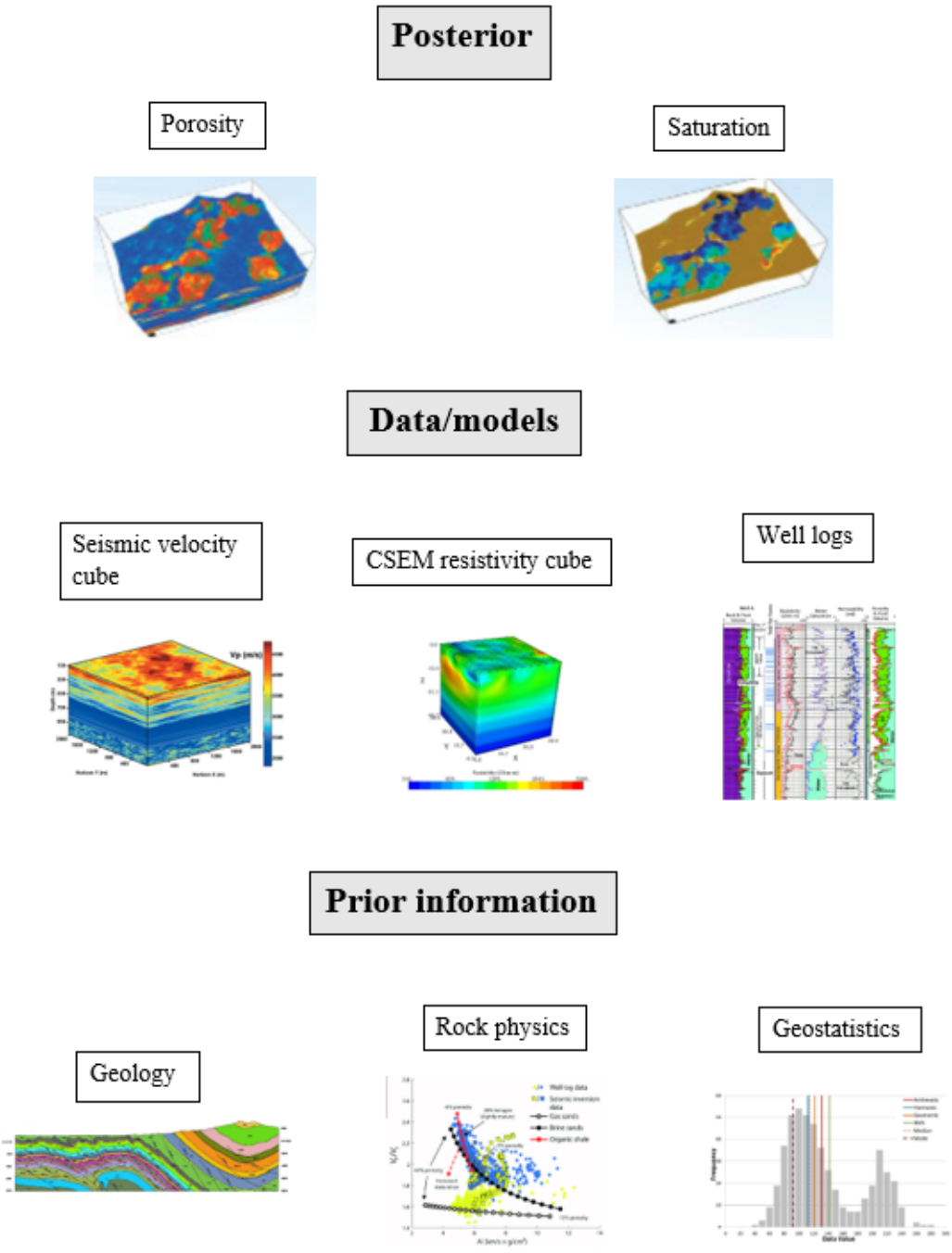

Figure 4.3: Examples of prior information, data/models and posterior results.

Depending on the type of data/models (synthetic, well logs or maps), there are some differences in the code. This is described in the next subsections. The most important Matlab codes are attached in Appendix C, where the rest is being omitted.

4.2 Synthetic testing

The whole idea to start with synthetic data is that the true values are known and the goal is to get as close as possible with the inversion results to those values. A simple model was created with the dimensions of depth (z) ranging from 800 m to 1600 m and offset (x) ranging from 0 m to 800 m. A reservoir zone at 1150-1250 m depth was defined. The offset increment length (dx) was set to 25 m and the depth increment length (dz) was set to 12.5 m. In the reservoir, the ϕ was set to 20% and the S_w to 20%, while outside the ϕ is 12% and S_w is 100%. The model parameters are summarized in Table 4.1.

Table 4.1: Model parameters used for synthetic testing. dx = offset increment, dz = depth increment, x = offset, z = depth, ϕ = porosity, S_w = water saturation, res = reservoir zone.

dx [m]	dz [m]	x [m]	z [m]	ϕ res [-]	ϕ [-]	S_w res [-]	S_w [-]
25	12.5	0-800	800-1600	0.2	0.12	0.2	1.0

In the forward modeling, the Archie and Gassmann equations (clean sandstone case) were used to calculate $logR_v$ and V_p, respectively. The value of the parameters used in the Archie and Gassmann equations are based on the well logs to make it similar to the actual situation in the Johan Castberg area.

Some noise (5%) was added to the properties (S_w and ϕ) to make it more realistic to the real world. A random number generator was also introduced in order to give random numbers for the properties. Minimum S_w and ϕ were set to 0.01 and the maximum values were set to 1 for S_w and 0.5 for ϕ.

Then, prior μ and σ for the properties (ϕ and S_w), as well as σ and μ errors for the models ($logR_v$ and V_p) were defined. The next step was to calculate the likelihood functions (product of the likelihood functions of $logR_v$ and V_p) and find the MLH. The MLH was then normalized. In the end, the posterior distributions are calculated based on the priors for the properties and the normalized MLH. MAP, μ and σ are being calculated for the posterior distributions.

4.3 Well logs testing

After being sure that the code worked well for the synthetic cases, the next step was to apply the code on well logs. At this point, the pre defined models are replaced by real data in terms of well logs. The code is similar to the code for synthetic data, and the main differences will be described below.

The las files of the well logs needed to be imported into Matlab before the code could be tested. Only LFP (Lithology Fluid Prediction) logs created by Equinor's petrophysics group were used. Well tops were introduced in order to indicate the different formations in the wells. Then, the logs were blocked in two different ways (into the same blocking size as for the 3D cubes (25-50 m) and averaged on the formations). When blocking high frequent well logs, the well logs get the same resolution (sampling) as the cubes and is reliable when comparing the well logs with cubes (due to the problem with different resolution). Depth below seabed was used as depth (z) and kelly bushing was taken into account to get the correct depth. Depth below seabed is the same as the sum of the kelly bushing and water depth subtracted from the actual measured depth. No noise added as for synthetic data, since the logs are real measurements were noise already exists.

Input to the petrophysical model was set to 50% oil and 50% gas among the fluid that was not water. Input to the forward modeling are now S_o, S_g, ϕ, V_{cl}, CEC and z. The V_{cl} log was computed from the GR log using the simple relation

$$V_{cl} = \frac{GR_{log} - GR_{min}}{GR_{max} - GR_{min}} \tag{4.6}$$

where GR_{log} is the GR log value, GR_{min} is the gamma ray for clean sand and GR_{max} is the gamma ray for shale (Mavko et al., 2009). Density was introduced in order to show the potential of adding density data in addition to $logR_v$ and V_p in the joint inversion as a third geophysical parameter.

4.4 Calibration of forward modeling

The calibration of the rock-physics modeling was a lot of work. The forward modeling needed to be tuned in to the three wells. Some important plots from the rock-physics modeling are given in Appendix A. Figure A.1-A.4 compare the brine, virgin and model logs for the studied wells. Some rock-physics relations of ϕ, V_p and V_s are presented in Figure A.5-A.9. Some important well logs of the three wells are given in Figure A.10-A.12. The tuning parameters with the corresponding values and other important forward modeling parameters are given in Table A.1 and A.2, respectively. In the forward modeling part, Archie and a combination of Han's model and Gassmann equations were used. The combined Han-Gassmann model was created for several reasons. First, to account for shale content for V_p calculation, second, because of the missing matrix shear modulus lfp-log and third, to get rid of the bulk modulus of the dry rock (K_{dry}) because it is hard to estimate without measure it from cores in the lab.

A temperature dependence on the dry shear modulus was included in the Han-Gassmann combined model to get a correct shear modulus. This was done to obtain a single rock-physics model fitting all the three wells, which has jurassic reservoir zones at different depths. The wells are sitting in different down-faulted blocks. This temperature effect on the dry shear modulus (μ_{dry}) is given by

$$\mu_{dry} = (1-\beta) s_{temp} \mu_{ma} \tag{4.7}$$

where β is the Biot coefficient, s_{temp} is a temperature dependency and μ_{ma} is the shear modulus of the matrix. This formula was defined during the thesis, in order to account for the temperature dependency of the dry shear modulus. The code was tested on the three wells mentioned in chapter 1 (7219/9-1T2, 7220/7-1 and 7220/8-1). The well logs for R_w, K_w, ρ_g and ρ_w were used to improve the forward modeling code in order to tune in the code for the specific geology in the Johan Castberg area.

4.5 Maps testing

After getting good inversion results from the well testing, the code was applied to maps computed from 3D cubes of R_v and V_p. The reasons for using maps instead of 3D cubes are, because the FWI and CSEM inversion cubes have low depth resolution, the depths are not fully consistent and the inversion runs much faster than on cubes. The maps are more than a horizon and that is why words like time/depth/horizon slice are avoided. The maps show average R_v and V_p for the Jurassic reservoir. When computing maps, the interval of interest can be extracted from the cubes and therefore influence the different resolution by taking out a thicker interval (500 m) from the CSEM cube compared to the FWI cube (50 m). The interpreted horizon of the Top Realgrunnen Gp (see Figure B.1 and B.2) was used as reference horizon. An interval of 200 m up and 300 m down around Top Realgrunnen Gp was used from the CSEM cube and 50 m down around Top Realgrunnen Gp was ued from the FWI cube (based on how the cubes looked like around the Skrugard well). The forward modeling code was still the same as for the well testing part, but also here, different priors and standard deviation were tested out in order to get a small model misfit and property misfit. Input data as interpretation of Top Realgrunnen Gp, seabed, R_v map and V_p map were imported into Matlab and used as input data. Easting and northing were also considered and imported. The difference between Top Realgrunnen Gp and the seabed constitutes the burial depth of today.

Chapter 5

Results

5.1 Synthetic models

The synthetic model testing consisted of two different cases, namely one non reservoir case scenario (overburden) and one reservoir case scenario. The depth for the non reservoir case is 1000 m below seabed, while the reservoir case is located at 1212.5 m depth. The two cases will be compared in terms of the inversion results and model misfits to show how they differ for both S_w and ϕ. The values for μ and σ for prior of S_w and ϕ, as well as measuring errors for the input models are given in Table 5.1. Wide priors and small noise variance for the input models are chosen. That means, the models are trusted and therefore controls the posterior distributions.

Table 5.1: Values of μ and σ for the priors (ϕ and S_w) and the models ($logR_v$ and V_p).

Parameter	ϕ [-]	S_w [-]	$logR_v$ [Ω m]	V_p [m/s]
μ prior	0.2	0.7		
σ prior	0.3	0.5		
μ error model			0	0
σ error model			0.2	50

Figure 5.1 a and b shows the models for $logR_v$ and V_p, respectively. These models will be slightly different for every time the code is tested, because 5% noise which gives rise to slightly different values is added. The $logR_v$ values in the reservoir are ca 1.5 Ωm and ca 0.5 Ωm in the overburden. The V_p values in the reservoir are ca 2350 m/s, while in the overburden it is ca 2900 m/s. The $logR_v$ and V_p are the forward models of the true values of ϕ and S_w.

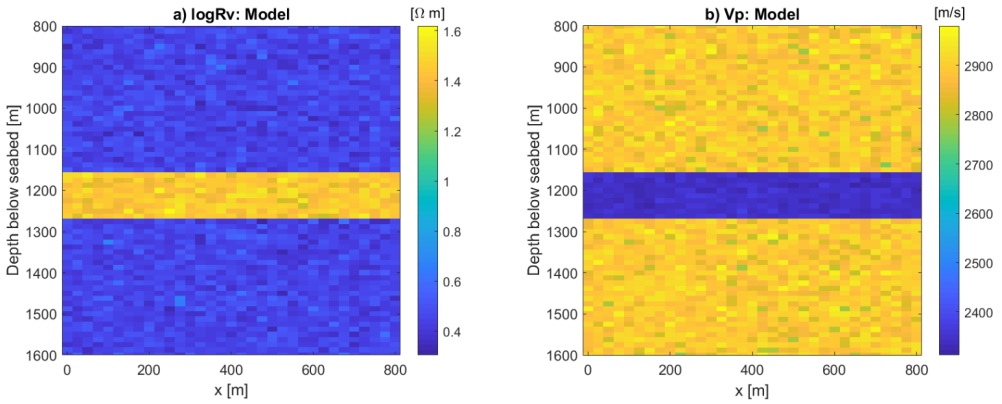

Figure 5.1: Forward models of $logR_v$ og V_p. The reservoir is located at 1150-1275 m depth.

The S_w and ϕ values for true, posterior μ, posterior σ and the property misfit are presented in Figure 5.2 a-h. By looking at the property misfits of S_w and ϕ (Figure 5.2 d and h), the misfit in the reservoir is ca 0.02 for S_w and -0.07 for ϕ, while 0.03-0.07 for S_w and 0 for ϕ in the overburden. The posterior σ for S_w is 0.05-0.07 for both the reservoir and overburden (Figure 5.2 c). The posterior σ for ϕ in the reservoir is 0.1 and in the overburden it is 0.01 (Figure 5.2 g).

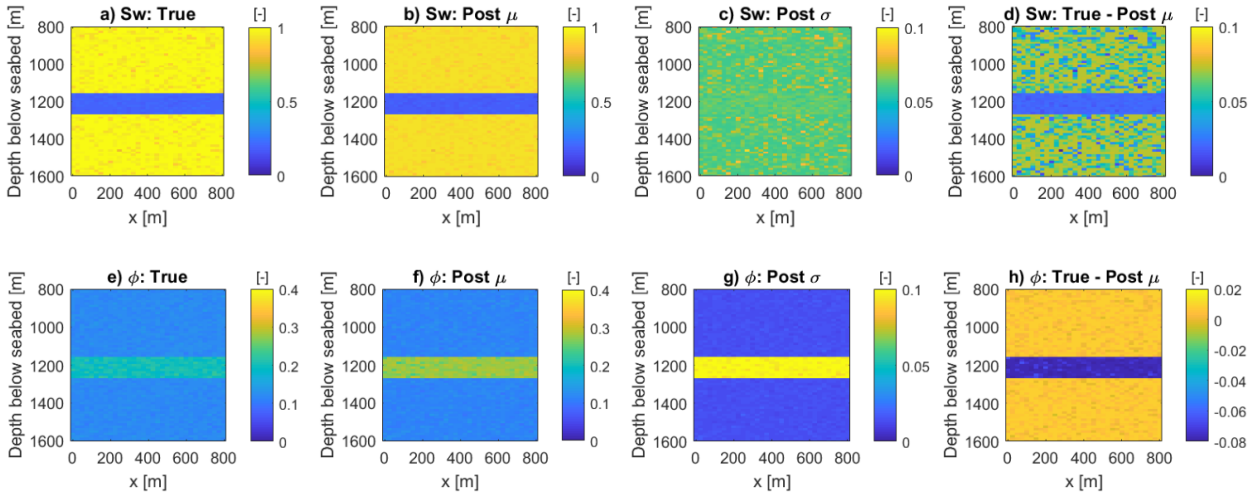

Figure 5.2: True, posterior μ, posterior σ and property misfits for S_w (top) and ϕ (bottom).

Figure 5.3 and 5.4 show the marginal likelihood probability distributions of the $logR_v$ and V_p in the overburden and within the reservoir for both S_w and ϕ. The maximum value of the marginal likelihood distributions is the MLH and indicates which value the model ($logR_v$ or V_p) predicts for either S_w or ϕ at a given depth. A black star is shown and informs about the true value of S_w and ϕ for the given depth. The $logR_v$ MLH function at 1000 m depth is closer to the true value

for ϕ than for S_w, while at reservoir depth, the MLH function is closer to the true value for S_w than for ϕ. The V_p MLH function for S_w at 1000 m depth, is not within the defined range of S_w, while the MLH function for ϕ is relatively close to the true value. At 1212.5 m, the MLH function of S_w is closer to the true value compared to ϕ.

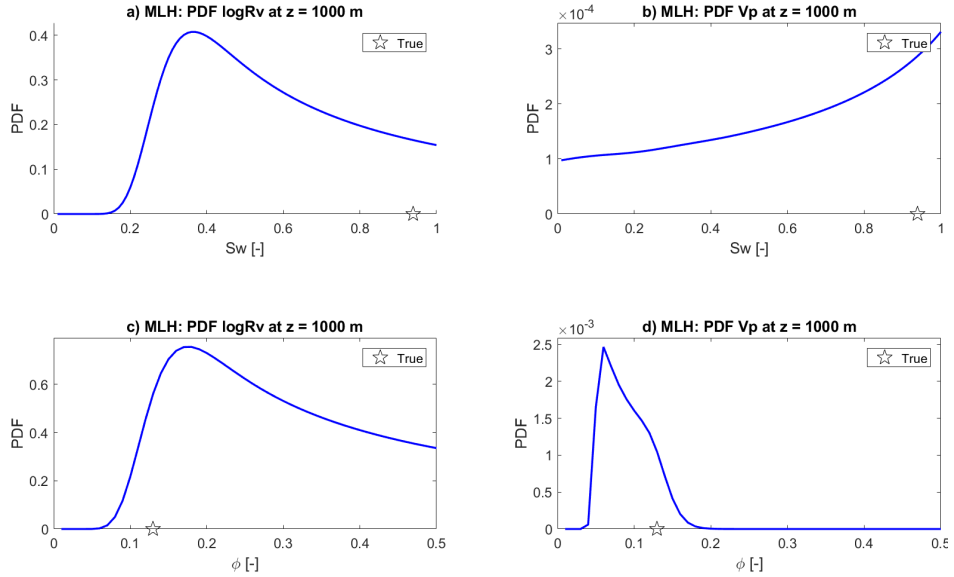

Figure 5.3: MLH pdf's at 1000 m depth. The true value is marked with a black star. a) $logR_v$ for S_w, b) V_p for S_w, c) $logR_v$ for ϕ and d) V_p for ϕ.

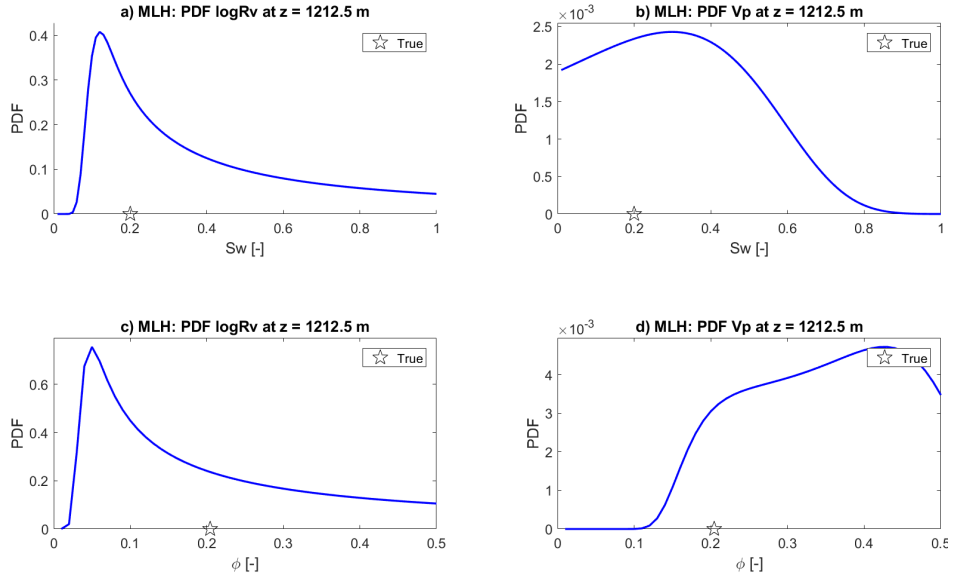

Figure 5.4: MLH pdf's at 1212.5 m depth. The true value is marked with a black star. a) $logR_v$ for S_w, b) V_p for S_w, c) $logR_v$ for ϕ and d) V_p for ϕ.

The connection between the prior, likelihood and posterior for S_w and ϕ at the two depths are presented in Figure 5.5. The MLH in Figure 5.5 a-d, is the product of the likelihood contributions from $logR_v$ and V_p models at the same depth for the investigated property (S_w or ϕ). At 1000 m depth, the posterior and likelihood distributions are almost the same for S_w, while they are the same for ϕ. The priors are very broad and has little influence on the posterior distributions. At 1212.5 m depth, the posterior and likelihood distributions are more different for S_w and ϕ, compared to at 1000 m depth. The priors are still wide, but has more influence on the posterior distributions compared to the overburden. Note the global and local maxima of the MLH curve for ϕ at reservoir depth (see Figure 5.5 d). Figure 5.5 d is the only case where the true, μ and MAP values are not close to the same value.

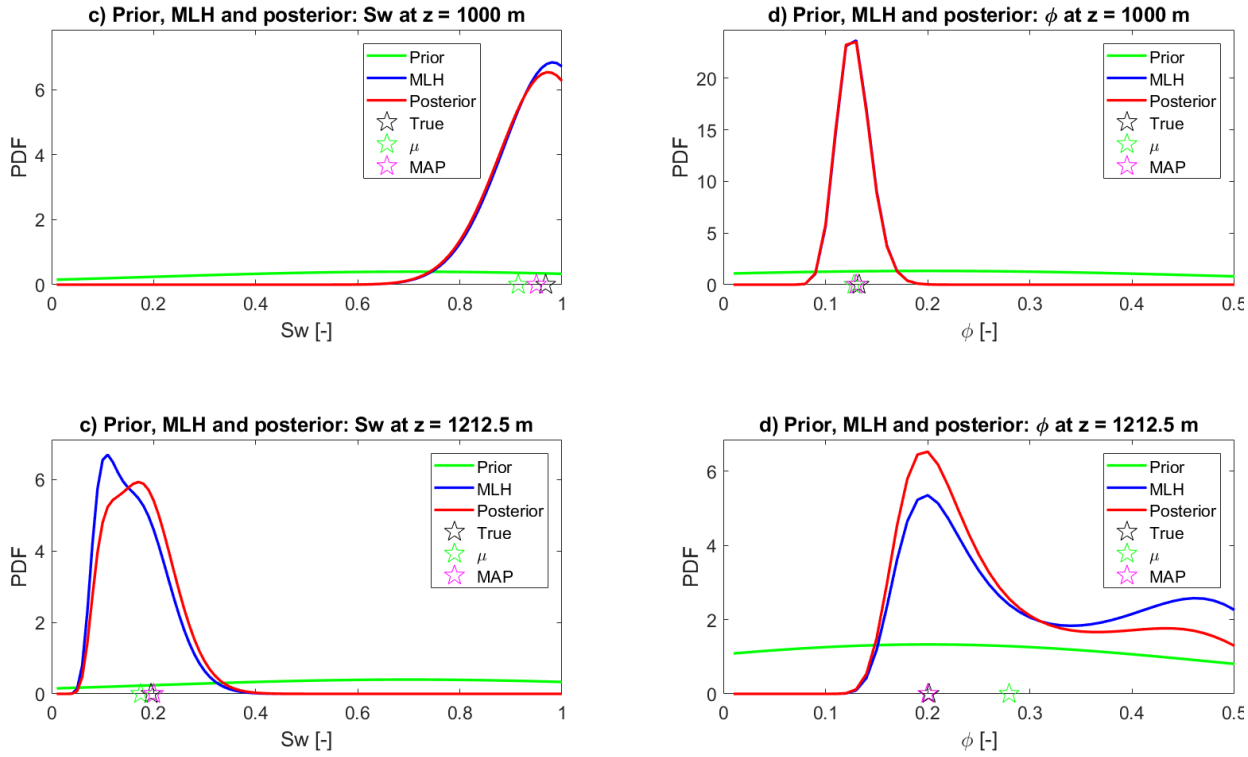

Figure 5.5: Prior (green), MLH (blue) and posterior (red) at 1000 m and 1212.5 m depth. The true, μ and MAP values of S_w and ϕ are marked with black, green and pink stars, respectively. a) S_w at 1000 m, b) ϕ at 1000 m, c) S_w at 1212.5 m and d) ϕ at 1212.5 m.

Figure 5.6 shows the MLH for the $logR_v$ and V_p at both depths for all combinations of S_w and ϕ. Yellow indicates the highest probability for what the S_w and ϕ should be at a specific depth and the probability is the same as long the colour is the same. The $logR_v$ MLH for the two depths have similar shapes, while the shapes of V_p are completely different. Depending on the depth and the model ($logR_v$ or V_p), Figure 5.6 a-d are covering different ranges of S_w and ϕ. Figure 5.6 a is not covering low S_w and low ϕ, while Figure 5.6 b do not cover ϕ above ca 10%. Only the lowest S_w is missing in Figure 5.6 c, while Figure 5.6 d does not include ϕ below 15% and S_w above 80%.

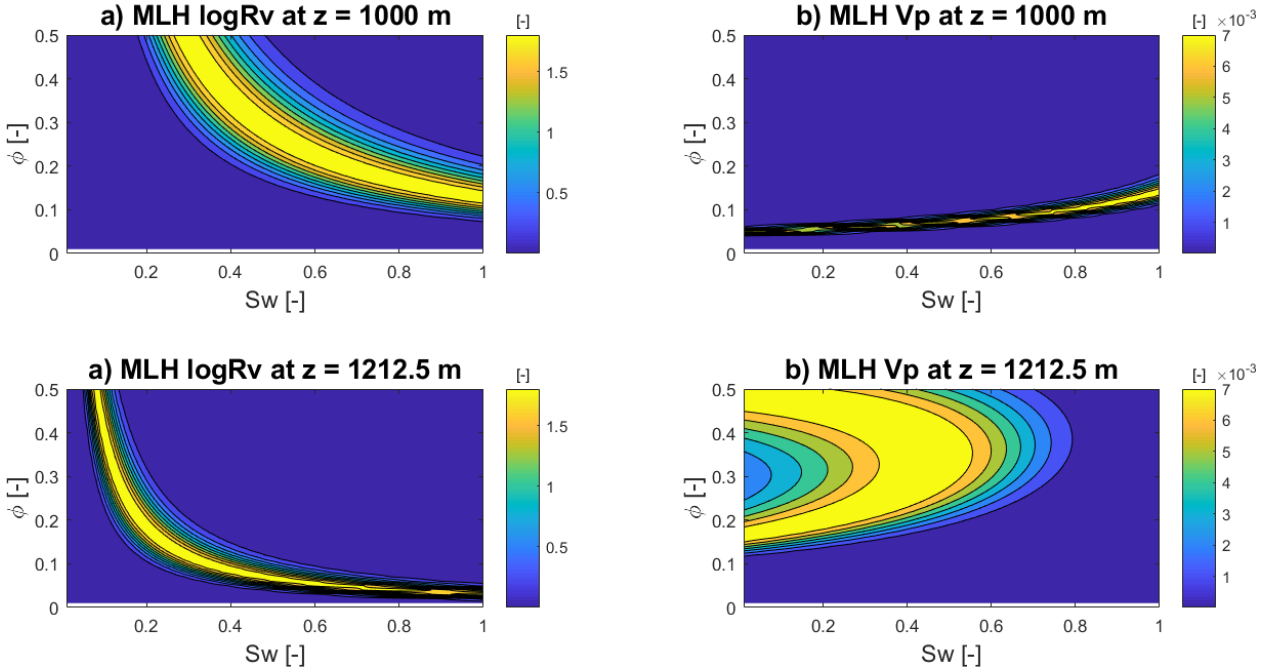

Figure 5.6: MLH functions for all combinations of ϕ and S_w. Contributions to likelihood distributions from a) $logR_v$ at 1000 m, b) V_p at 1000 m, c) $logR_v$ at 1212.5 m and d) V_p at 1212.5 m.

Figure 5.7 illustrates the prior, MLH and posterior for the two depths. The prior is the same for both depths (only one defined prior), while the MLH and posterior differ for the different depths. The MLH distributions in Figure 5.7 are the product of the MLH distributions given in Figure 5.6 (product of $logR_v$ and V_p at the same depth). In other words, Figure 5.7 b is the product of Figure 5.6 a and b, while Figure 5.7 e is the product of Figure 5.6 c and d. When comparing the MLH and posterior at 1000 m, they look very much the same. At reservoir depth, the MLH and posterior also look similar, but in Figure 5.7 e, the global and local maxima once again appear as already seen in Figure 5.5 d. In Figure 5.7 f, the most probable (global maxima) point is chosen as the posterior result. At 1000 m depth, it is most probable to find S_w of 96% and ϕ of 11%, while at 1212.5 m depth both S_w and ϕ have 21%. Taking those numbers into account and comparing them with the pre defined true values for ϕ and S_w (see Table 4.1), makes it clear that the property misfit is very small for both properties.

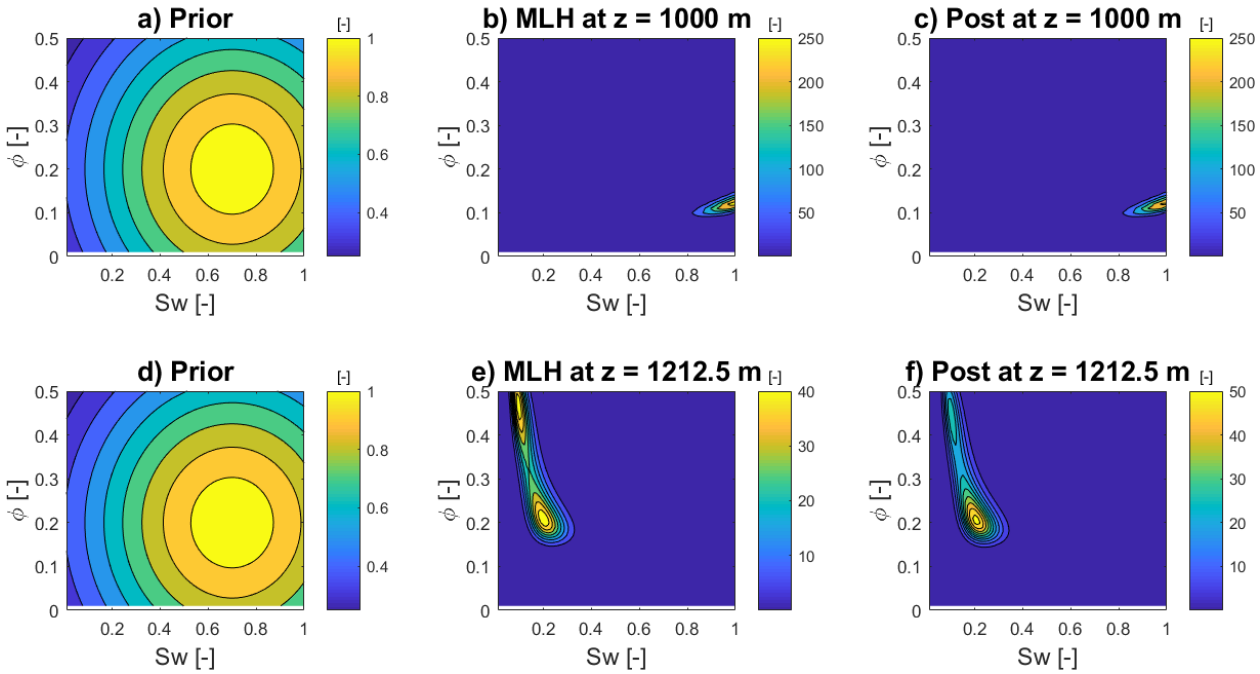

Figure 5.7: Prior, MLH and posterior for overburden and reservoir depth. a) and d) Prior for all combinations of ϕ and Sw, b) MLH at 1000 m, c) Posterior at 1000 m, e) MLH at 1212.5 m and f) Posterior at 1212.5 m.

5.2 Well log data

In this chapter, the well log results are presented. Only blocked logs, both averaged on formations and regular, will be shown. In addition, the contribution of including ρ as a third geophysical parameter will be presented. The future possibility to use Full Tensor Gravity (FTG) data to obtain estimates of ϕ, in particular in the case of shallow gas reservoirs, was foreseen. Wide priors are chosen, as well as a small noise variance for the input data, are presented in Table 5.2. The data control the posterior distributions, but the prior for S_w is narrower and the likelihoods wider than compared to the synthetic case. The prior for ϕ is the same as for the synthetic case, because this gave a much better result than to decrease σ for ϕ to 0.2. This would be natural to do, because real data is now considered instead of synthetic models. The reason for choosing wider likelihoods, is that working with real data has higher uncertainty compared to synthetic models. Well tops for the formations Top Hekkingen, Top Stø, Top Nordmela, Top Tubåen and Top Fruholmen are marked on all the well log plots. The ϕ and S_w plotted are the MAP value at each data point.

Table 5.2: Values of μ and σ for the priors (ϕ and S_w) and the data ($logR_v$, V_p and ρ).

Parameter	ϕ [-]	S_w [-]	$logR_t$ [Ωm]	V_p [m/s]	ρ [g/cm^3]
μ prior	0.2	0.9			
σ prior	0.3	0.3			
μ error data			0	0	0
σ error data			0.5	150	50

Figure 5.8 a and b presents regular and formation blocked logs for the well 7219/9-1T2, respectively. The V_p has an increasing trend with depth and has a bigger model misfit in the overburden and the Hekkingen Fm than in the Realgrunnen Gp. In the Realgrunnen Gp, the virgin log and the modeled $logR_t$ follows the same trend where the modeled log is overestimating in the interval of interest. Even in the overburden, there is a rather small model misfit. No sudden increase of $logR_t$ is observed. There are property misfits bigger than 1σ in the Hekkingen Fm, in the Torsk Fm and Kolmule Fm in the overburden for ϕ and S_w, but less than 1σ in the Realgrunnen Gp. The ϕ decreases in general with depth. The measured S_w is mostly above 90%.

The Havis well results are presented in Figure 5.9. Figure 5.9 a is regular blocked, while Figure 5.9 b is blocked over the formations. The V_p increases with depth, while the $logR_t$ has a sudden change in the Stø and Nordmela formations. The model misfits for V_p and $logR_t$ are small, especially for V_p. The model misfit of V_p is biggest in the overburden and the Hekkingen Fm, while the $logR_t$ has higher model misfit in the overburden and the Stø and Nordmela formations. The inversion results are in general good in the reservoir zones, especially for the ϕ. The inversion results for both ϕ and S_w are less good in the Hekkingen Fm, where the property misfit is larger than 1 σ. The ϕ decreases and increases with depth, depending on where in the stratigraphy the actual measuring point is located. The S_w has significantly lower values in the Stø and Nordmela formations than outside. The property misfits are within one σ significance from Top Stø and downwards for ϕ and from lower part of Stø Fm and downwards for S_w.

The Skrugard well results are presented in Figure 5.10 and 5.11. In addition to comparing regular blocked and formation blocked well logs, ρ is included as a third geophysical parameter to show how it will affect the inversion results. The V_p increases with depth, while the $logR_t$ has a sudden change in the Stø Fm. The V_p and $logR_t$ model misfits are small, except in the Stø Fm for the $logR_t$ and in the overburden for V_p. The model misfit of ρ is very small in both the overburden and the reservoir. The width of the 1σ significance is much narrower when including ρ. The inversion results are in general good, but adding density make the ϕ much better and improves S_w a bit. It is a misfit larger than 1σ for the ϕ in the Fuglen Fm and above, while S_w has a bigger misfit than 1σ in the Stø Fm and from Top Fuglen Fm and above. The ϕ increases in the Fuglen, Stø and bottom Nordmela formations, and decreases in the Nordmela and Tubåen formations. The S_w has significantly lower values in the Stø and Nordmela formations than in the rest.

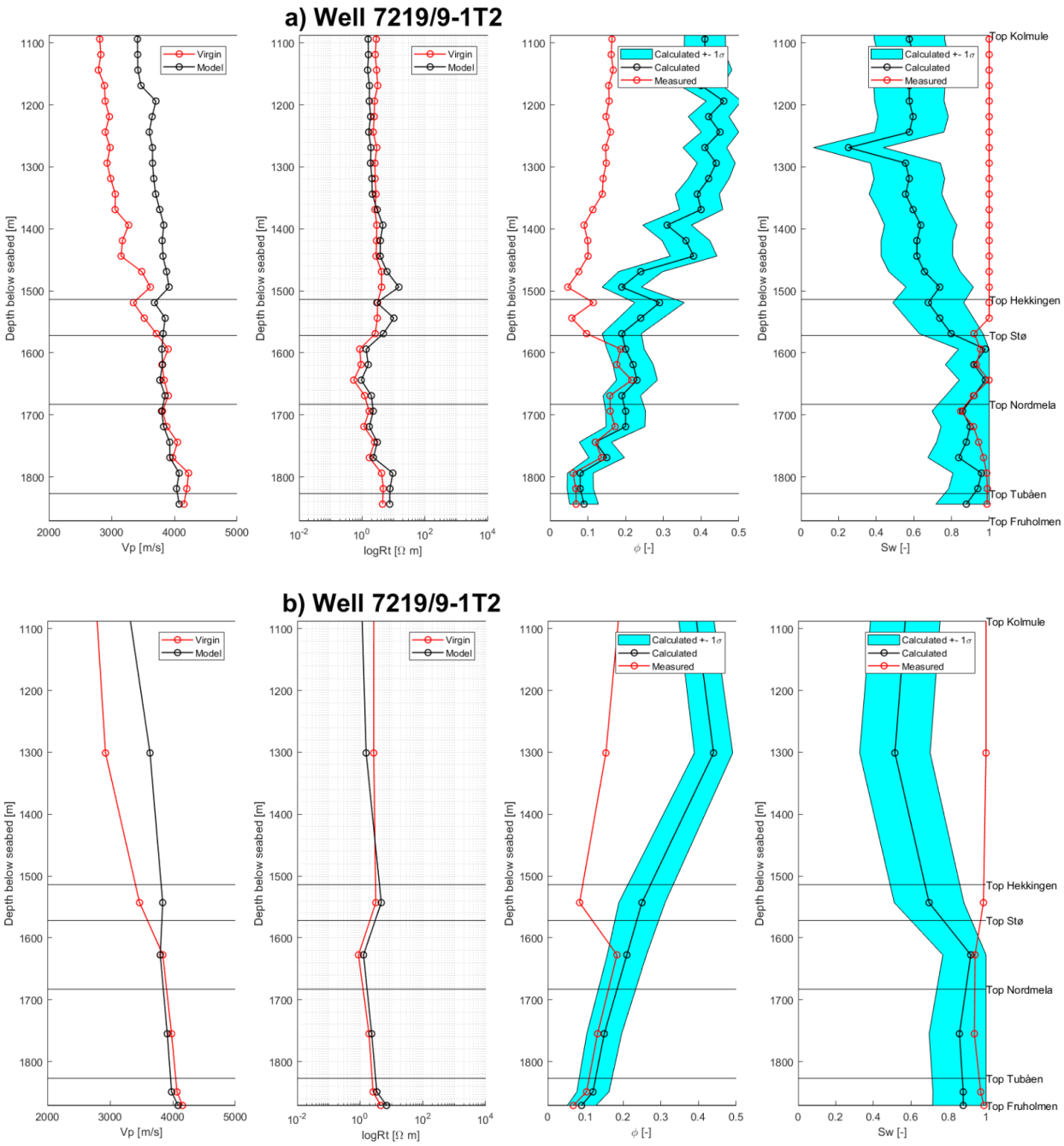

Figure 5.8: Well 7219/9-1T2 showing a) regular blocked well logs and b) blocked over formations. Left: Virgin well logs (red) and modeled well logs (black) for V_p and $logR_t$. Right: Measured well logs (red), inversion results of ϕ and S_w (black) and the 1 σ significance of the properties (turquoise).

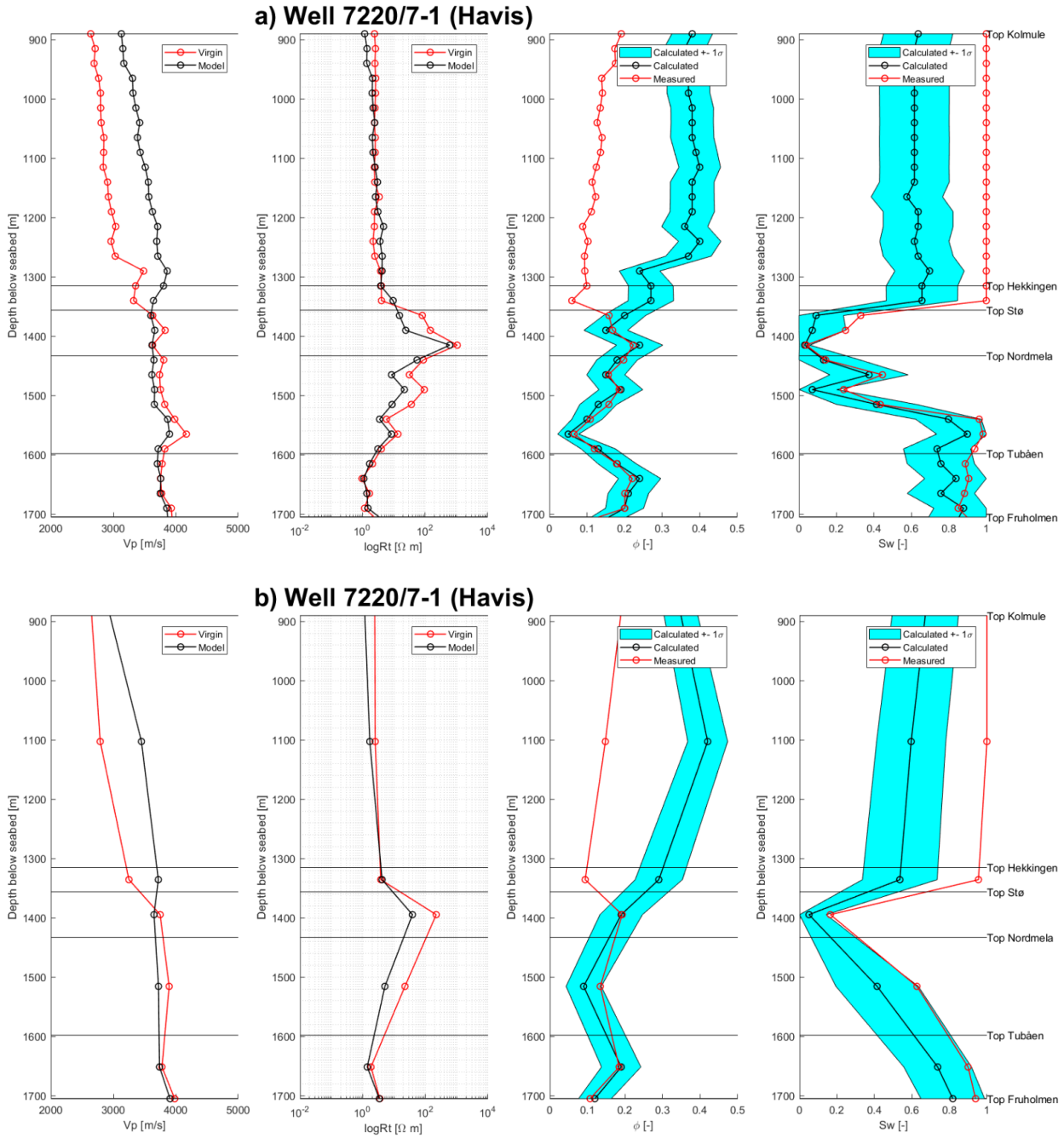

Figure 5.9: Well 7220/7-1 showing a) regular blocked well logs and b) blocked over formations. Left: Virgin well logs (red) and modeled well logs (black) for V_p and $logR_t$. Right: Measured well logs (red), inversion results of ϕ and S_w (black) and the 1 σ significance of the properties (turquoise).

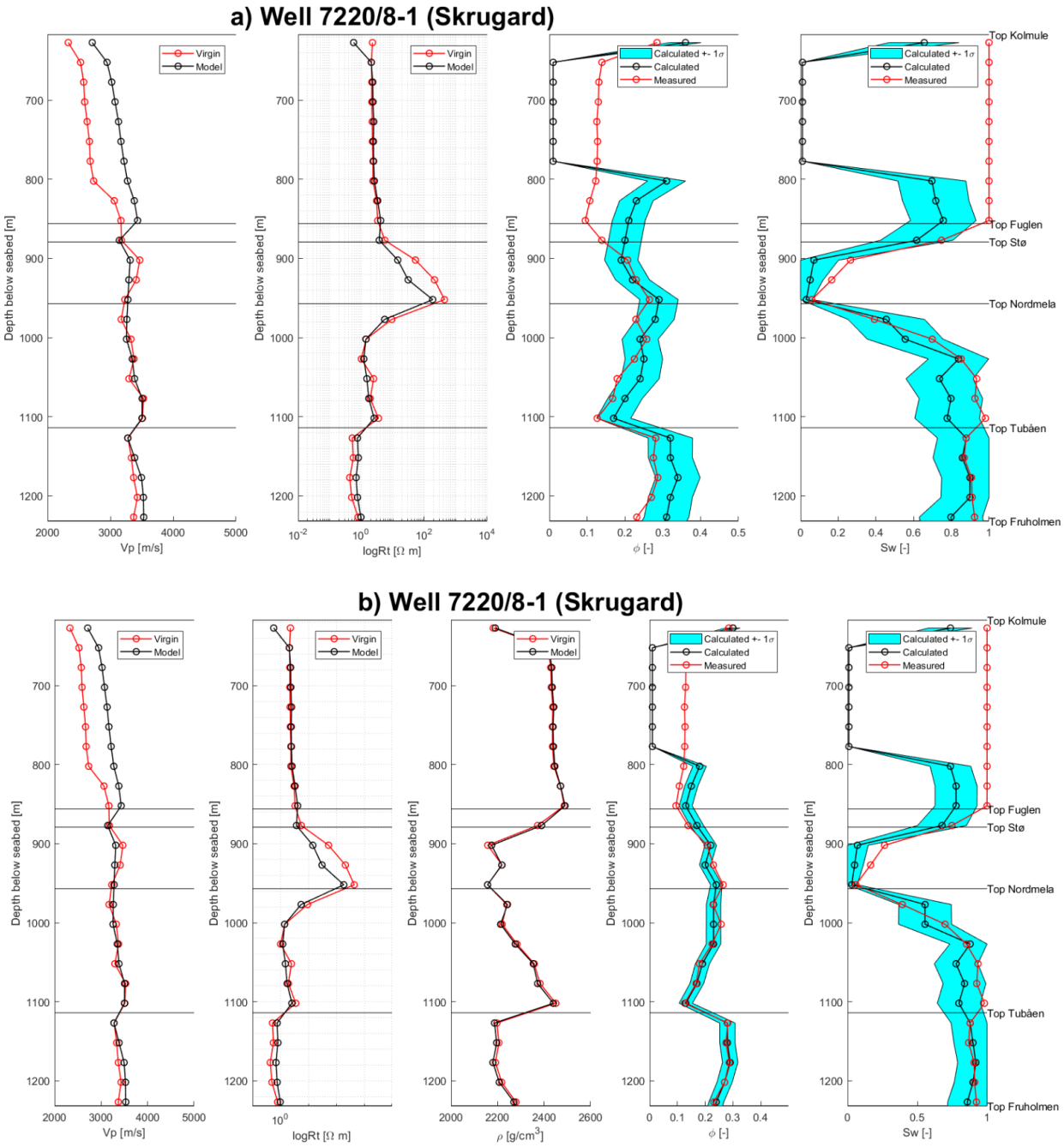

Figure 5.10: Well 7220/8-1 showing regular blocked well logs for a) without ρ and b) with ρ. Left: Virgin well logs (red) and modeled well logs (black) for V_p and $logR_t$. Right: Measured well logs (red), inversion results of ϕ and S_w (black) and the 1 σ significance of the properties (turquoise).

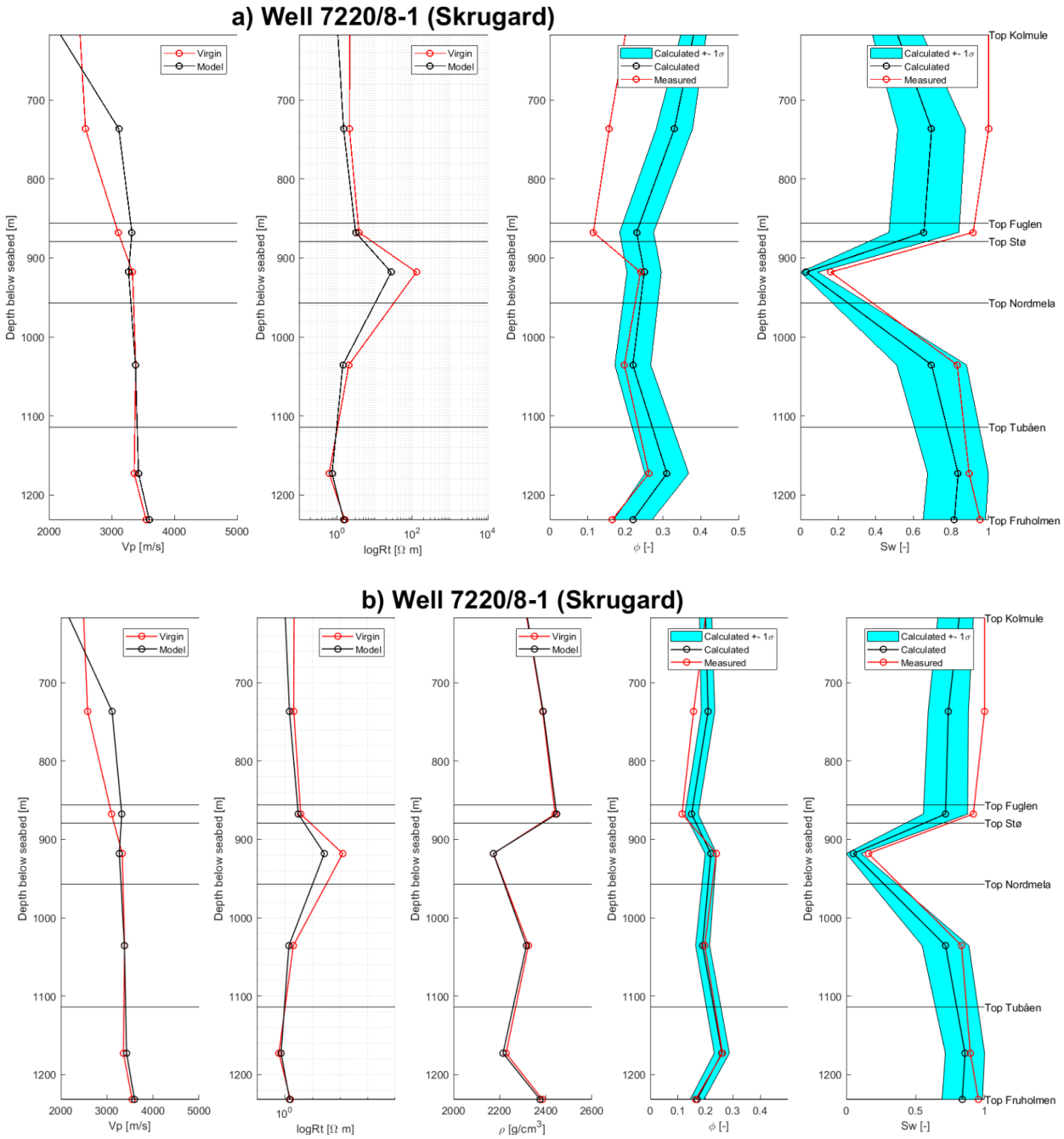

Figure 5.11: Well 7220/8-1 showing formation blocked well logs for a) without ρ and b) with ρ. Left: Virgin well logs (red) and modeled well logs (black) for V_p and $logR_t$. Right: Measured well logs (red), inversion results of ϕ and S_w (black) and the 1 σ significance of the properties (turquoise).

Figure 5.12 and 5.13 show the prior, posterior and likelihood distributions for a chosen depth in the reservoir zone (827 m depth) and overburden (952 m depth) using the Skrugard well as example, as well as with and without ρ as a third geophysical parameter. Note that the MLH is now a product of three data types. The overburden case is not calibrated to the wells. This depth is chosen of two reasons. First, to see how a depth outside the reservoir is affected by ρ as a third geophysical parameter. Second, to see how ρ will affect the posterior distributions for a depth that is not calibrated to the wells. The ϕ starts, as for the synthetic testing, at 1%. This is why there is no data for $\phi = 0$. The prior is of course the same for all the four cases, because only one prior is defined that is valid both in the overburden and in the reservoir.

The MLH at 827 m depth without ρ shows that the highest probability is to find S_w of 50% and ϕ of 22% (see Figure 5.12 b). The corresponding MAP values for S_w and ϕ are 72% and 23%, respectively (see Figure 5.12 c). Figure 5.12 e and f give the results for the same depth when including ρ. The MLH indicates that the highest probability is to find S_w of 60% and ϕ of 15%. The MAP of the S_w is 78% and the ϕ is now 15%. The MLH and posterior are shifted to lower ϕ and higher S_w compared to the case without ρ.

Figure 5.13 a-c show the results for a depth of 952 m (in the reservoir zone) without ρ. The MLH shows that the highest probability is to find S_w of 3% and ϕ of 29%. The MAP of the S_w is 3% and the ϕ is 29%. Fig 5.13 d-f give the results for the same depth with ρ. The MLH shows that the highest possibility is to find S_w of 3% and ϕ of 24%. The MAP of S_w is 3% and ϕ is 24%. The MLH and posterior are shifted to lower ϕ compared to the case without ρ. The S_w is still the same.

Taking ρ into account, shifted the the posterior distributions to lower ϕ and higher S_w in the overburden, while at reservoir depth the S_w was unchanged and the ϕ became lower. Also, the ρ made the value of the MLH and posterior much higher compared to the case without (both in the overburden and the reservoir).

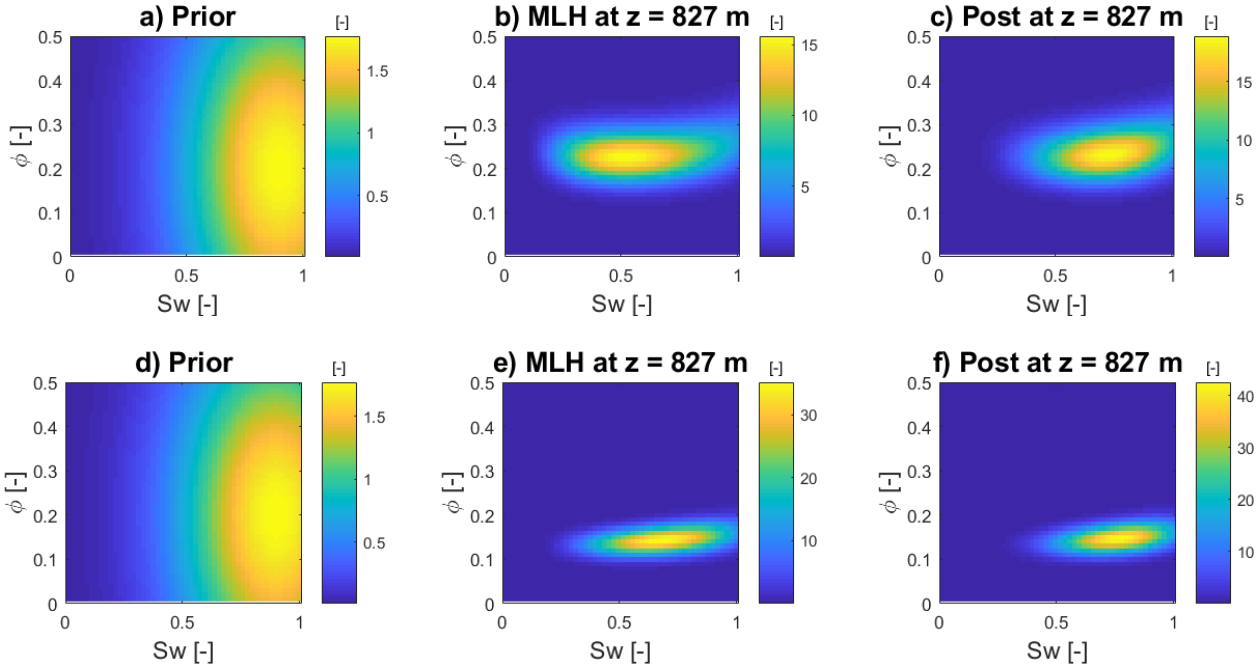

Figure 5.12: Overburden case at 827 m depth in well 7220/8-1. b) and c) are without ρ, while e) and f) are with ρ. Note the differences in MLH and posterior in b) and c) compared to e) and f).

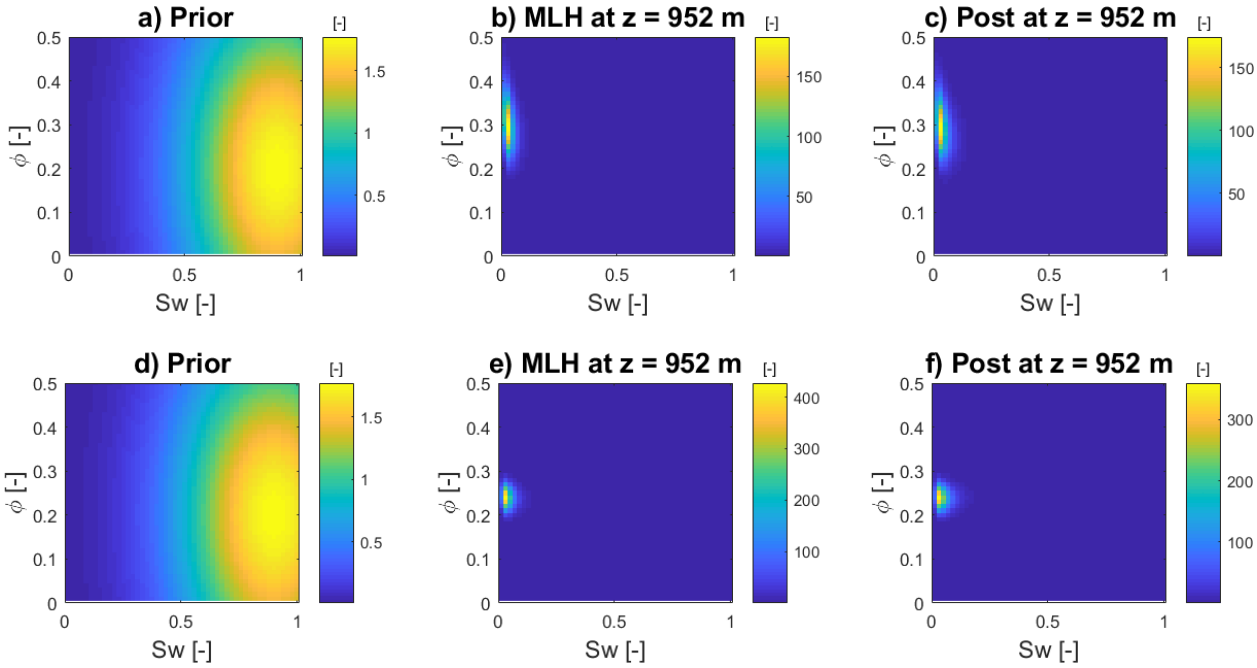

Figure 5.13: Reservoir case at 952 m depth in well 7220/8-1. b) and c) are without ρ, while e) and f) are with ρ. Note the differences in MLH and posterior in b) and c) compared to e) and f).

5.3 Map models

As seen in the previous chapter about well log data, the S_w and ϕ were estimates with small property misfits, while V_p and $logR_t$ had small model misfits. The exciting part comes now, when the method is applied on map models.

On all the maps in this chapter, the three wells are marked. The area of the computed maps are ca 215 km^2. Figure 5.14 a-c show maps of the burial depth of today, as well as $logR_v$ and V_p from the CSEM inversion and FWI, respectively. The burial depth of today vary between 540 m and 2800 m. Deep buried areas are marked with yellow and shallow buried areas with blue. Three main high resistive areas are visible (one next to each of the wells) in Figure 5.14 b. Some areas in Figure 5.14 c have much higher V_p than other areas. By comparing those high V_p zones with the burial depth of today, a connection between the high V_p zones and deep buried rocks could be observed.

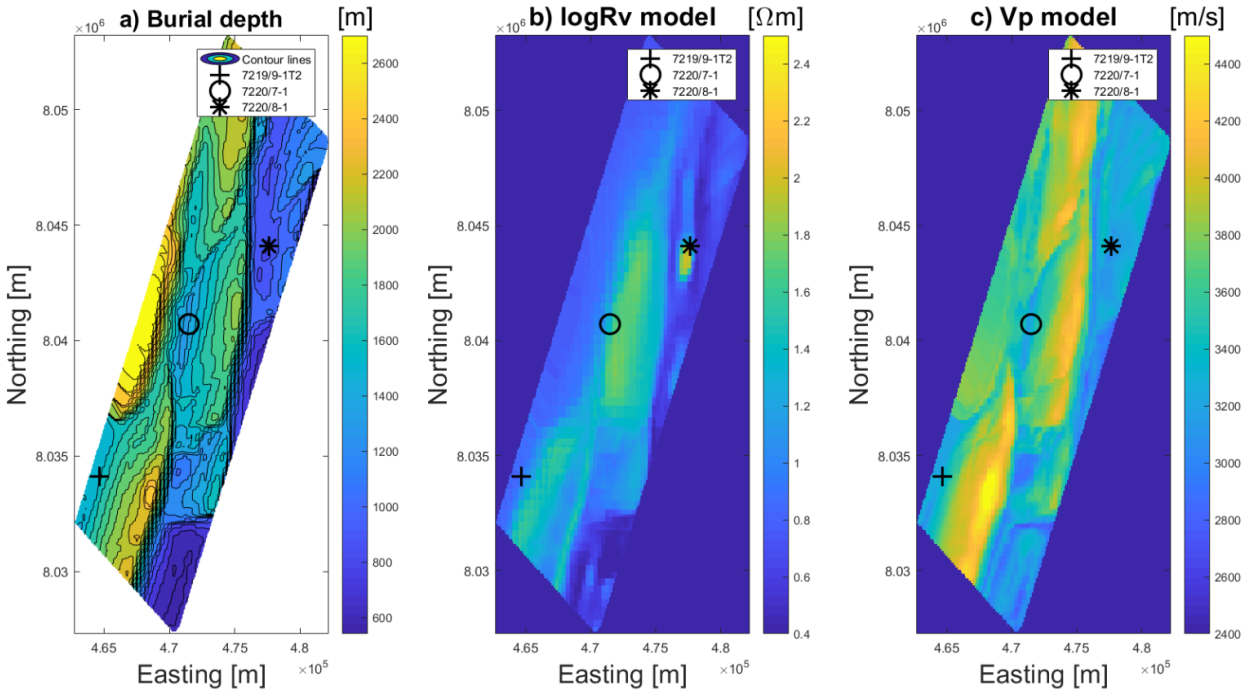

Figure 5.14: a) Burial depth of today, b) model of $logR_v$ and c) model of V_p.

In total, five different cases will be presented, based on various combinations of the prior and likelihood. The reason for doing so, is to show how different prior and likelihood distributions affect the posterior distributions. For the map testing, wide priors are defined as σ = 0.5 for S_w and σ = 0.2 for ϕ, and narrow priors as σ = 0.3 for S_w and σ = 0.05 for ϕ. Wide likelihoods are defined as σ = 350 m/s for V_p and σ = 1.0 Ωm for $logR_v$, and narrow as σ = 150 m/s for V_p and σ = 0.5 Ωm for $logR_v$. Similar priors and likelihoods as chosen in the well log testing, were also used in the maps testing, but in general the (σ) error of the models need to be higher compared to the well log data. The uncertainty of the models ($logR_v$ and V_p) from the CSEM inversion and FWI, respectively, are significantly higher compared to well log data. With well logs, the parameters are measured directly in the well bore, while working with models from the first stage of the inversion (see Figure 4.1), nothing are measured directly. Two factors make it challenging to find suitable values for σ for $logR_v$. First, resistivity is logarithmic and the R_t in the wells vary from 0 to 1000 Ωm. The variation is so big and makes it therefore difficult to choose appropriate σ for it. Second, comparing $logR_t$ and $logR_v$ directly should be avoided, because they measure the horizontal and vertical resistivity, respectively. Even by knowing what the R_t are in the wells, it is difficult to find appropriate values for the σ of $logR_v$, because it is hard to say what the values for $logR_v$ are in this case (without knowing the anisotropy). It is easier to find appropriate values for the σ of V_p, because V_p can be directly compared between the value from the model at the well locations with the measured value in the well. Table 5.3-5.7 illustrate the chosen values for the prior and likelihood for the different cases. The results for the five cases are shown in Figure 5.15-5.19 (a and b present the model misfits of $logR_v$ and V_p, while c and d present the inversion results of S_{HC} and ϕ), respectively. Table 5.8-5.13 present the results at the well locations.

Table 5.3: Case 1: Values of μ and σ for the priors and models.

Parameter	ϕ [-]	S_w [-]	$logR_v$ [Ωm]	V_p [m/s]
μ prior	0.2	0.9		
σ prior	0.2	0.5		
μ error model			0	0
σ error model			0.5	150

Table 5.4: Case 2: Values of μ and σ for the priors and models.

Parameter	ϕ [-]	S_w [-]	$logR_v$ [Ωm]	V_p [m/s]
μ prior	0.2	0.7		
σ prior	0.2	0.3		
μ error model			0	0
σ error model			1.0	150

Table 5.5: Case 3: Values of μ and σ for the priors and models.

Parameter	ϕ [-]	S_w [-]	$logR_v$ [Ωm]	V_p [m/s]
μ prior	0.2	0.9		
σ prior	0.05	0.5		
μ error model			0	0
σ error model			0.5	350

Table 5.6: Case 4: Values of μ and σ for the priors and models.

Parameter	ϕ [-]	S_w [-]	$logR_v$ [Ωm]	V_p [m/s]
μ prior	0.2	0.7		
σ prior	0.05	0.3		
μ error model			0	0
σ error model			1.0	350

Table 5.7: Case 5: Values of μ and σ for the priors and models.

Parameter	ϕ [-]	S_w [-]	$logR_v$ [Ωm]	V_p [m/s]
μ prior	0.2	0.9		
σ prior	0.05	0.3		
μ error model			0	0
σ error model			0.5	250

In case 1, the prior distributions are wide and the likelihood functions narrow (see Table 5.3). The model misfits and inversion results for case 1 are presented in Figure 5.15. The model misfit for $logR_v$ lies between -0.3 Ωm and 0.23 Ωm, while the model misfit for V_p lies between -246 m/s and 110 m/s. The ϕ has a minimum of 4% and maximum of 48%. The S_{HC} lies between 0% and 93%.

In case 2, the prior for ϕ and the likelihood for $logR_v$ are wide, while the prior for S_w and the likelihood for V_p are narrow (see Table 5.4). Figure 5.16 shows the model misfits and inversion results for case 2. The model misfit for $logR_v$ lies between -1.5 Ωm and 0.65 Ωm, while the model misfit for V_p lies between -240 m/s and 92 m/s. The ϕ ranges from 3% to above 48%. The S_{HC} lies between 22% and 59%.

In case 3, the prior for ϕ and likelihood for $logR_v$ are narrow, while the prior for S_w and likelihood for V_p are wide (see Table 5.5). The model misfits and inversion results for case 3 are given in Figure 5.17. The model misfit for $logR_v$ lies between -0.26 Ωm and -0.06 Ωm, while the model misfit for V_p lies between -633 m/s and 631 m/s. The ϕ ranges from 16% to above 24%. The S_{HC} lies between 14% and 89%.

In case 4, the prior for ϕ, the prior for S_w and the likelihood for $logR_v$ are narrow, while the likelihood for V_p is wide (see Table 5.6). Figure 5.18 shows the model misfits and inversion results for case 4. The model misfit for $logR_v$ lies between -1.3 Ωm and 0.06 Ωm, while the model misfit for V_p lies between -623 m/s and 613 m/s. The ϕ ranges from 16% to above 24%. The S_{HC} lies between 28% and 55%.

In case 5, the priors and the likelihood for $logR_v$ are narrow, while the likelihood for V_p is something between narrow and wide (see Table 5.7). Figure 5.19 shows the model misfits and inversion results for case 5. The model misfit for $logR_v$ lies between -0.68 Ωm and -0.11 Ωm, while the model misfit for V_p lies between -505 m/s and 554 m/s. The ϕ ranges from 12% to above 26%. The S_{HC} lies between 10% and 87%.

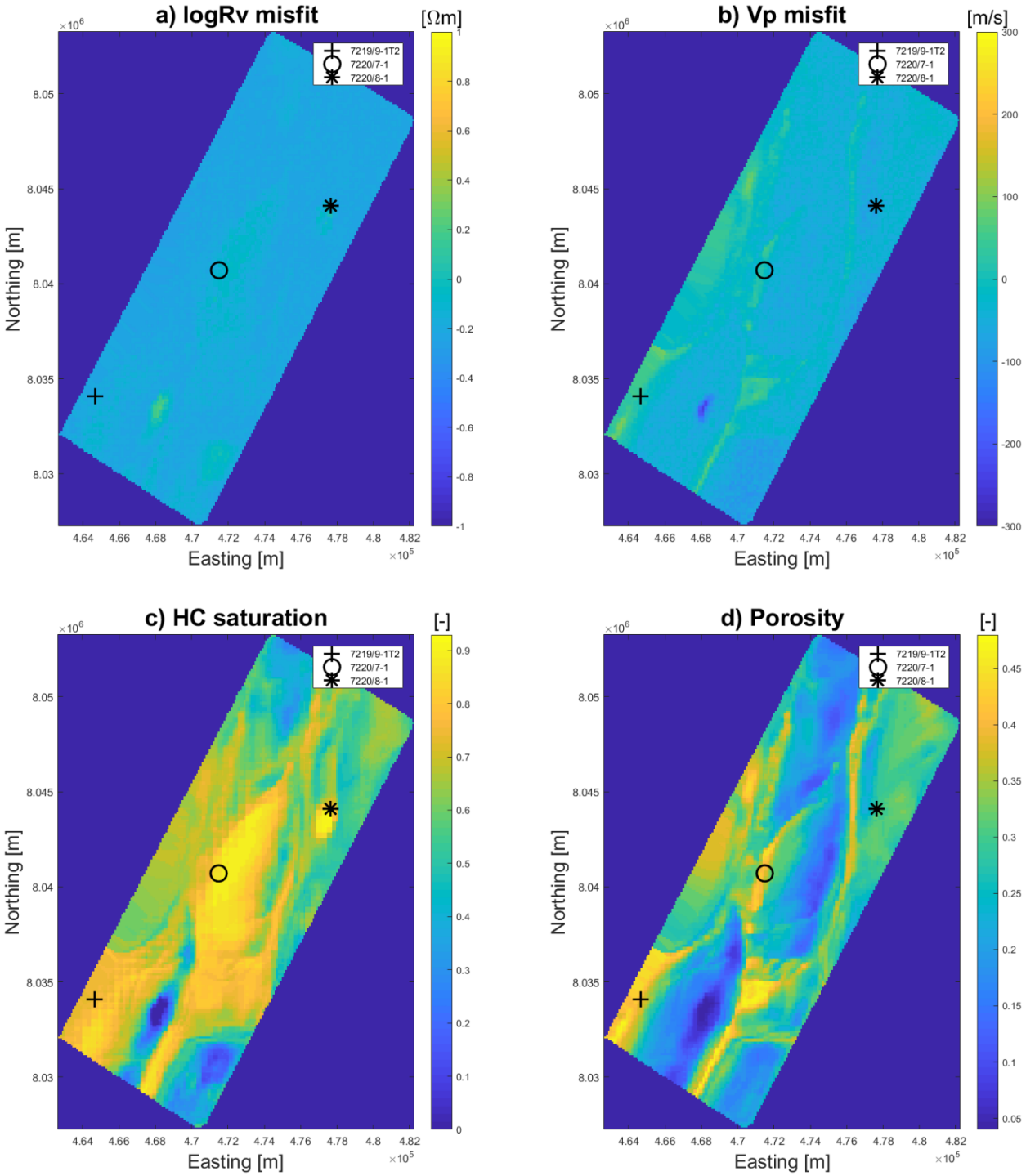

Figure 5.15: Model misfits and inversion results for case 1. a) $logR_v$ misfit, b) V_p misfit, c) S_{HC} and d) ϕ.

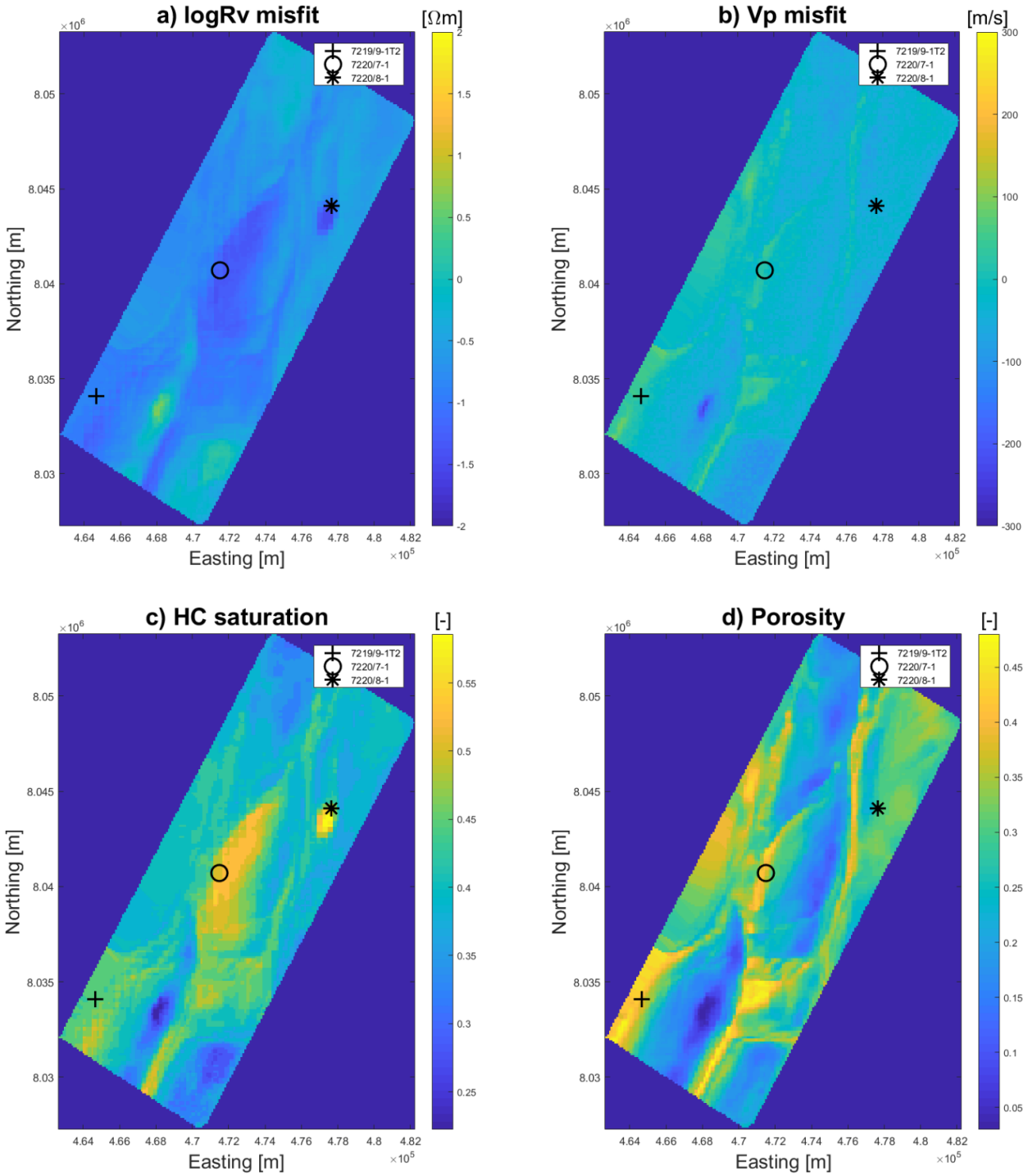

Figure 5.16: Model misfits and inversion results for case 2. a) $logR_v$ misfit, b) V_p misfit, c) S_{HC} and d) ϕ.

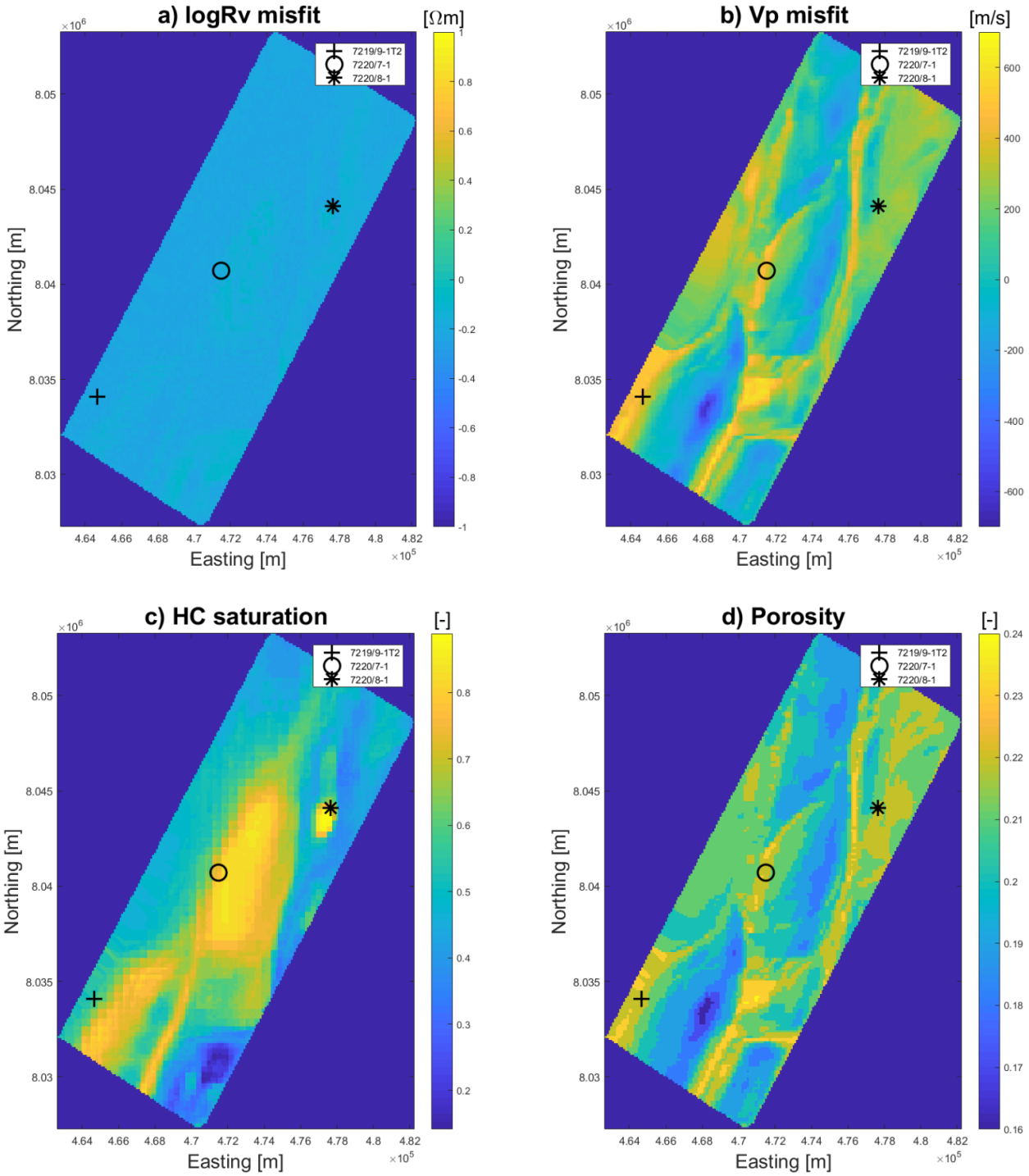

Figure 5.17: Model misfits and inversion results for case 3. a) $logR_v$ misfit, b) V_p misfit, c) S_{HC} and d) ϕ.

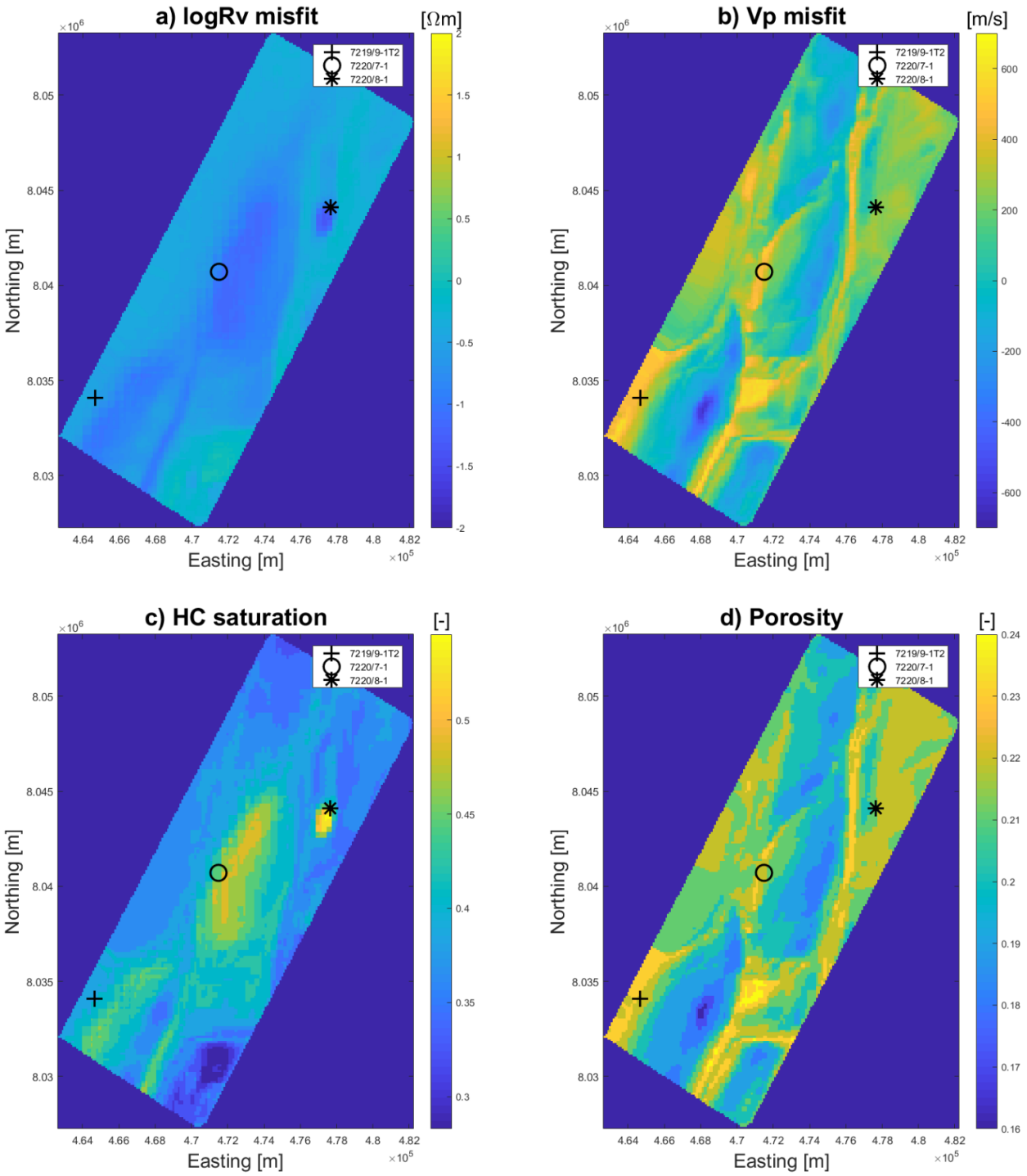

Figure 5.18: Model misfits and inversion results for case 4. a) $logR_v$ misfit, b) V_p misfit, c) S_{HC} and d) ϕ.

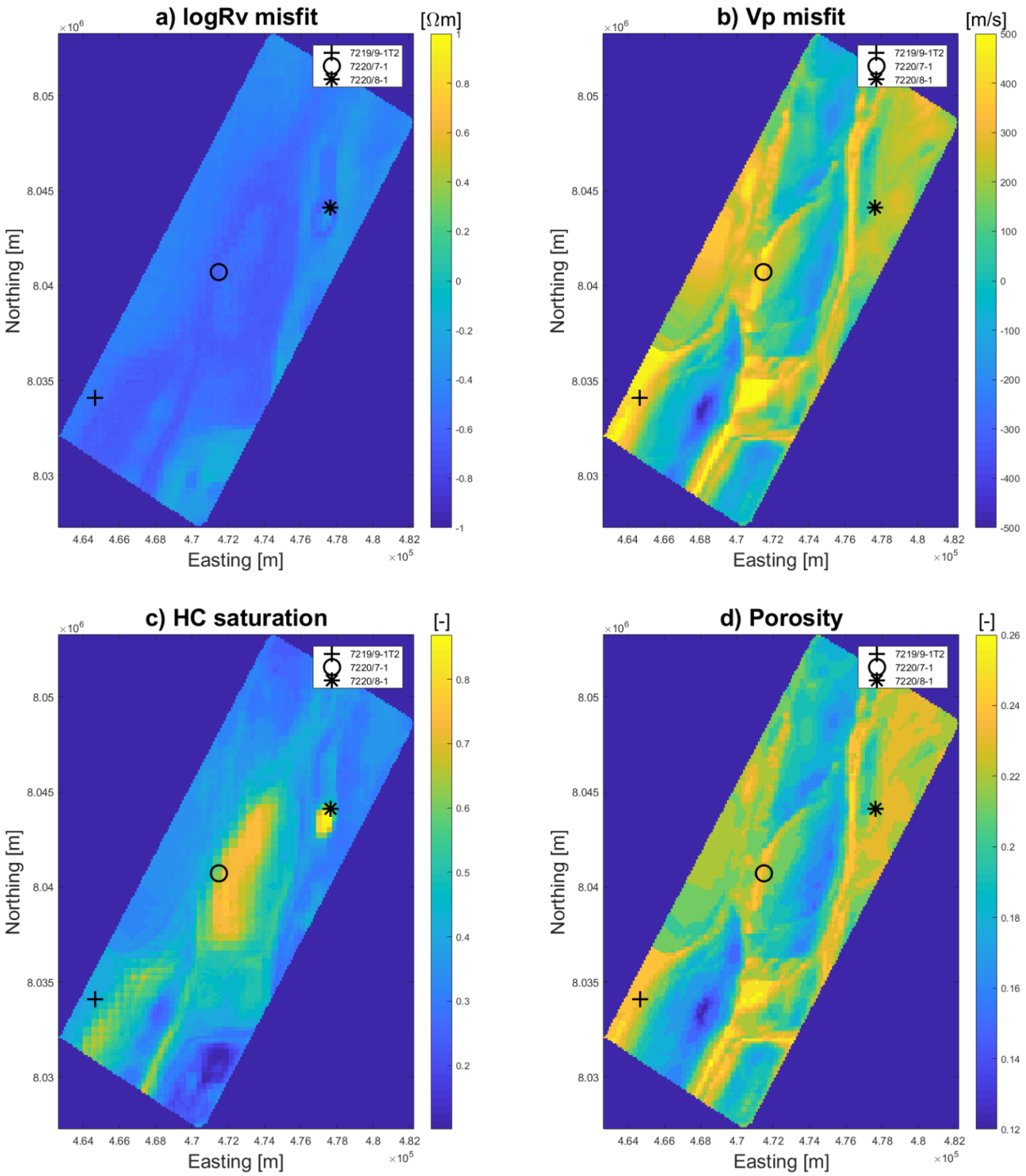

Figure 5.19: Model misfits and inversion results for case 5. a) $logR_v$ misfit, b) V_p misfit, c) S_{HC} and d) ϕ.

Table 5.8 shows the values for the virgin well log of V_p and calculated TR based on the R_t well log, lfp well logs for ϕ and S_{HC} and modeled values for both V_p and TR at the well locations. It also shows the misfit between what the well log measured and the value at the well location for the models from CSEM inversion and FWI. The V_p from the virgin log in the well 7220/8-1 is the slowest, 7220/7-1 has higher and 7219/9-1T2 has the highest V_p. The deepest well (7219/9-1T2) has the biggest V_p difference between the well log and the V_p model (from inversion), while the shallowest well (7220/8-1) has the smallest V_p difference. For $logR_v$, well 7219/9-1T2 has the smallest difference, while well 7220/7-1 has the biggest. The TR from well logs and lfp log S_{HC} are averaged from the interval from 200m above Top Realgrunnen Gp (Top Stø) down to 300 m below it (same extracted depth interval as from the R_v cube). Formula 3.31 is used to calculate the TR based on the $logR_t$. Virgin log V_p and lfp log ϕ are the average in the interval from Top Realgrunnen Group and down to 50 m below (same interval as from the V_p cube). Modeled R_v and V_p are taken directly from the well locations on the map. The model misfits TR and V_p are the difference between modeled (synthetic) and models from the CSEM inversion and FWI, respectively.

Table 5.9 to 5.13 show the modeled values and the model misfits for TR and V_p, as well as the property misfits for ϕ and S_{HC} in the well locations for the five cases. For both model and property misfits, the values from this work are subtracted from the values from the provided maps and well logs.

In case 1, the smallest model misfit of TR is observed in well 7219/9-1T2 and the largest misfit in 7220/8-1. The biggest misfit of V_p is in 7220/8-1, while the smallest is in 7219/9-1T2. Well 7219/9-1T2 has the largest property misfit for ϕ, while 7220/8-1 has the smallest. The biggest property misfit for S_{HC} is observed in 7219/9-1T2, and the smallest in 7220/8-1. In general, both the ϕ and S_{HC} are overestimated.

In case 2, the largest model misfit of TR is observed in well 7220/8-1 and the smallest misfit in 7219/9-1T2. The biggest misfit of V_p is in 7220/8-1, while the smallest in 7220/7-1 (no misfit). Well 7219/9-1T2 has the largest property misfit for ϕ, while 7220/8-1 has the smallest. The biggest property misfit for S_{HC} is observed in 7219/9-1T2, and the smallest in 7220/7-1. In general, both the ϕ and S_{HC} are overestimated, except the S_{HC} for the wells 7220/7-1 and 7220/8-1.

In case 3, the largest misfit in TR are observed in well 7220/8-1, while the smallest misfit is in 7219/9-1T2. The biggest misfit of V_p is in 7219/9-1T2, while the smallest in 7220/8-1. Well 7219/9-1T2 has the largest property misfit for ϕ, while 7220/8-1 has the smallest. The biggest property misfit for S_{HC} is observed in 7219/9-1T2, and the smallest in 7220/8-1. In general, both the ϕ and S_{HC} are overestimated, except the S_{HC} and ϕ in the well 7220/8-1.

In case 4, the largest misfit in TR is observed in well 7220/8-1 and the smallest misfit in 7219/9-1T2. The biggest misfit of V_p is in 7219/9-1T2, while the smallest in 7220/8-1. Well 7219/9-1T2 has the largest property misfit for ϕ, while 7220/8-1 has the smallest. The biggest property misfit for S_{HC} is observed in 7220/8-1, and the smallest in 7220/7-1. The ϕ is overestimated in 7219/9-1T2 and 7220/7-1, while the S_{HC} is overestimated in 7219/9-1T2.

In case 5, the largest misfit in TR is observed in well 7220/8-1 and the smallest misfit in 7219/9-1T2. The biggest misfit of V_p is in 7219/9-1T2, while the smallest in 7220/8-1. Well 7219/9-1T2 has the largest property misfit for ϕ, while 7220/8-1 has the smallest. The biggest property misfit for S_{HC} is observed in 7219/9-1T2, and the smallest in 7220/7-1. The ϕ is overestimated in 7219/9-1T2 and 7220/7-1, while the S_{HC} is overestimated in 7219/9-1T2.

Table 5.14 shows which case that gives the biggest and smallest model and property misfits, as well as showing if the input models were trusted or not. Case 1 gives the smallest TR model misfit, while the ϕ and S_{HC} property misfits are the biggest. The input models were trusted. Case 2 gives the biggest misfit for TR and the smallest for V_p. Only the V_p model is trusted. Case 3 gives the smallest property misfit for the ϕ. Only the $logR_v$ model is trusted. Case 4 gives the biggest V_p model misfit and the smallest property misfit for ϕ. None of the input models are trusted. Case 5 is a mix case and gives the smallest S_{HC} property misfit. The $logR_v$ model is trusted, while the V_p model is partly trusted.

Taking both ϕ and S_{HC} property misfits into account, case 1 gives the worst average posterior results and case 5 the best. When letting the priors affect the posterior results, the inversion results are good, while when letting the models control the posterior results, the inversion results are bad. This shows clearly that in this case, it's impossible to achieve both small model misfits and small property misfits. When one of the misfits (either model or property) is small is the other big and opposite.

Table 5.8: Comparing V_p and TR from well logs with V_p and TR models from inversion at the well locations in the map. The values for ϕ and S_{HC} from the well logs are also presented.

	Well 7219/9-1T2	Well 7220/7-1	Well 7220/8-1
TR from well log $[\Omega m^2]$	1414	38844	17952
V_p from well log [m/s]	3810	3684	3352
TR model from inversion $[\Omega m^2]$	3932	11640	11994
V_p model from inversion [m/s]	3315	3300	3150
TR misfit $[\Omega m^2]$	-2518	27204	5958
V_p misfit [m/s]	495	384	202
ϕ from well log [-]	0.15	0.18	0.23
S_{HC} from well log [-]	0.07	0.73	0.78

Table 5.9: Case 1: Modeled (synthetic) TR and V_p and model misfits of TR and V_p at the well locations in the map, as well as ϕ and S_{HC} property misfits.

	Well 7219/9-1T2	Well 7220/7-1	Well 7220/8-1
TR model from modeling $[\Omega m^2]$	2450	9953	8298
V_p model from modeling [m/s]	3323	3285	3080
TR model misfit $[\Omega m^2]$	1482	1687	3696
V_p model misfit [m/s]	-8	15	70
ϕ property misfit [-]	-0.25	-0.20	-0.05
S_{HC} property misfit [-]	-0.68	-0.14	-0.03

Table 5.10: Case 2: Modeled (synthetic) TR and V_p and model misfits of TR and V_p at the well locations in the map, as well as ϕ and S_{HC} property misfits.

	Well 7219/9-1T2	Well 7220/7-1	Well 7220/8-1
TR model from modeling $[\Omega m^2]$	529	733	1035
V_p model from modeling [m/s]	3341	3300	3104
TR model misfit $[\Omega m^2]$	3403	10907	10959
V_p model misfit [m/s]	-26	0	46
ϕ property misfit [-]	-0.24	-0.19	-0.05
S_{HC} property misfit [-]	-0.38	0.23	0.31

Table 5.11: Case 3: Modeled (synthetic) TR and V_p and model misfits of TR and V_p at the well locations in the map, as well as ϕ and S_{HC} property misfits.

	Well 7219/9-1T2	Well 7220/7-1	Well 7220/8-1
TR model from modeling $[\Omega m^2]$	2428	8491	7816
V_p model from modeling [m/s]	3725	3662	3321
TR model misfit $[\Omega m^2]$	1504	3149	4178
V_p model misfit [m/s]	-410	-362	-171
ϕ property misfit [-]	-0.07	-0.04	0.03
S_{HC} property misfit [-]	-0.5	-0.04	0.03

Table 5.12: Case 4: Modeled (synthetic) TR and V_p and model misfits of TR and V_p at the well locations in the map, as well as ϕ and S_{HC} property misfits.

	Well 7219/9-1T2	Well 7220/7-1	Well 7220/8-1
TR model from modeling $[\Omega m^2]$	1206	1484	1614
V_p model from modeling [m/s]	3736	3673	3343
TR model misfit $[\Omega m^2]$	2726	10156	10380
V_p model misfit [m/s]	-421	-373	-193
ϕ property misfit [-]	-0.07	-0.04	0.03
S_{HC} property misfit [-]	-0.31	0.28	0.33

Table 5.13: Case 5: Modeled (synthetic) TR and V_p and model misfits of TR and V_p at the well locations in the map, as well as ϕ and S_{HC} property misfits.

	Well 7219/9-1T2	Well 7220/7-1	Well 7220/8-1
TR model from modeling $[\Omega m^2]$	1190	3027	2904
V_p model from modeling [m/s]	3707	3636	3313
TR model misfit $[\Omega m^2]$	2742	8613	9090
V_p model misfit [m/s]	-392	-336	-163
ϕ property misfit [-]	-0.08	-0.05	0.03
S_{HC} property misfit [-]	-0.33	0.1	0.19

Table 5.14: The biggest and smallest model and property misfits for the different cases, as well as the priors and likelihoods.

	Case 1	Case 2	Case 3	Case 4	Case 5
TR model misfit $[\Omega m^2]$	Min	Max			
V_p model misfit [m/s]		Min		Max	
ϕ property misfit [-]	Max		Min	Min	
S_{HC} property misfit [-]	Max			Min	
Prior ϕ	Wide	Wide	Narrow	Narrow	Narrow
Prior S_w	Wide	Narrow	Wide	Narrow	Narrow
Likelihood $logR_v$	Narrow	Wide	Narrow	Wide	Narrow
Likelihood V_p	Narrow	Narrow	Wide	Wide	Narrow-wide

Chapter 6

Discussion

6.1 Work done

6.1.1 Synthetic models

The synthetic results show, as expected, that the Bayesian inversion works pretty well. In this case, the priors for both ϕ and S_w were wide and small noise variance for the models were defined (trusting both the $logR_v$ and V_p models). When defining a big σ for the priors and a small noise variance for the models, the models will find the answer by its own, without the help of the priors.

Looking again at Figure 5.7, the prior here is larger than zero for all combinations of ϕ and S_w. This is good, because every value between 0 and 1 for S_w and between 0 and 0.5 for ϕ has a higher probability than 0. No values of S_w and ϕ are excluded and only the models influence the posterior distributions. This is well illustrated in Figure 5.7 b and c. When comparing the MLH and posterior at 1000 m depth, they look very much the same, and this indicates that the models control the posterior distributions. At 1212.5 m depth, the situation is a bit different. The double maxima in Figure 5.5 d, are visible also in Figure 5.7 e. The posterior distribution chooses the MLH maxima with the highest value. This is a good example showing that the MLH function could also be bimodal and that in this case (because of the bimodal distribution) the prior decides which of the two maxima that is the global one. This also illustrates well how the difference between a unimodal and bimodal distribution is affected by the prior information.

For the unimodal situation, the prior did not influence the posterior result, but for the bimodal situation, the prior helped to find the global maximum. That is why the priors should be defined as accurate as possible, because they can contain information that is important for the posterior distributions. The reason for the bimodal distribution, is how the MLH functions are defined. In this case, a higher noise variance for V_p (for example 150 m/s) would give a unimodal distribution again. In the reservoir zone, a noise variance of 50 m/s was too low to get a unimodal distribution with the model created.

In Figure 5.3 and 5.4 a and c, the MLH distributions of $logR_v$ looks very much the same. This is because m and n in the Archie equation are approximately (1.8 and 2.0, respectively) the same and therefore the Archie equation do not see the difference between ϕ and S_w. On the other hand, the MLH distributions of V_p looks different as they should. The ϕ in Figure 5.6 and 5.7 do not start at 0, but starts at 1%. This is because the minimum ϕ defined in the prior is set to 1% (to avoid to divide with zero in the Archie equation).

6.1.2 Well log data

For the well testing, wide priors for both ϕ and S_w and low noise variance of $logR_t$ and V_p were defined. As for the synthetic models, the data influence the posterior distributions. The results from the tests on well log data, shown that the method works good, but not as good as for the synthetic models. In the overburden, both the property misfit of V_p and model misfits were bad, and this is due to the calibration of the rock physics model. Both the property misfits of $logR_t$ and ρ were very small also in the overburden. This means that the forward model for the V_p needs more attention compared to the other two. The overburden was not taken into account when calibrating the forward model, and in general, this is why the misfits are bigger here compared to the Realgrunnen Gp. The Hekkingen and Fuglen formations (and the overburden) showed bigger than 1σ property misfits for both ϕ and S_w in all the wells and this is due to higher clay content (high gamma response) compared to the Realgrunnen Gp. The clay content is not included in the forward model in a proper way and this is the reason to those misfits. By looking at Appendix A in Figure A.10 to A.12, the gamma response (due to clay content) are clearly higher in the Hekkingen/Fuglen formations and the overburden than in the

Realgrunnen Gp. Experience has shown that the Gassmann equation must be calibrated per formation or group. In the present study, the only focus was on the reservoir formations in the Realgrunnen Gp. The reservoir zones in the two discovery wells are being detected where the S_{HC} increases drastically. This proof that the developed method is able to zones where there is no HC and also able to find HC zones.

For the 7220/8-1 well, by including ρ as a third geophysical parameter, it is possible to make the property misfit for ϕ smaller also in the zones where the amount of clay are high. It seems like the ρ only affect the S_w if the interval is not calibrated to the well logs, but it affects ϕ in both the calibrated and not calibrated zones. This shows the importance of taking ρ into account as a third geophysical parameter. By looking at equation 3.18, it explains why the ρ has such a big influence on the ϕ.

The way to find out if the developed method works nor not, is the tests on the well logs. Here, real data measured directly in the wells are being investigated. Then, it is possible to compare the forward modeled results with what is being measured (data misfit) and the inversion results compared with the well logs calculated from other logs (property misfit). The inversion results are close to the measured values (especially in the zones with low amount of clay) and shows that the method works fine.

6.1.3 Map models

As seen throughout the thesis, there has been some challenges to solve (multi physics challenges). The first challenge is about the different physics behind CSEM and seismic (electric versus elastic). This was solved by a rock-physics framework calibrated at well locations. The uncertainties in the rock-physics models and the possibility that they vary between the well locations can increase the uncertainty in the inversion results. Therefore, a cross-gradient approach is an alternative approach which takes this into account. The second challenge is about the scale. Seismic, CSEM and well log techniques are operated at very different scales, varying from a few cm for the well logs to several hundreds of m for the CSEM method. Again, the solution was to obtain a robust rock-physics framework calibrated at well locations, reducing this uncertainty. The final challenge is about sensitivity. This is (partly) solved by extracting

maps from different depth intervals from the cubes. One more thing to consider regarding the sensitivity is how much the different input models should be trusted (relative weighting). This depends on how small or big the noise variance of the input models that are being defined. These challenges can be summarized as

- Physics: Electric versus elastic.
- Different scales.
- Different sensitivity.

By comparing Figure 5.14 c with the ϕ results in Figure 5.15 to 5.19, a connection between V_p and ϕ could be observed. High V_p areas have low ϕ and opposite. Those areas are also visible in Figure 5.14 a, being deep buried. The deeper buried high V_p zones are more compacted compared to shallower ones, and therefore give rise to higher V_p. A similarly trend is to be observed for the relation between $logR_v$ and S_{HC}. Comparing Figure 5.14 b with the S_{HC} in Figure 5.15 to 5.19, high resistive areas give high S_{HC} and opposite. These examples are showing the connections seen in the theory chapter, where the ϕ are linked to V_p and S_{HC} are linked to R_v. It is possible to see the edge effects from the big faults in the Bjørnøyrenna fault complex as a sudden change in depth in Figure 5.14 a. This is also well shown in Figure 5.14 c (southeast of the high V_p areas). Next to the big faults, there is problematic to get a good V_p model and makes the V_p model less accurate close the faults than far away. Having a look at Figure 5.19 c (as an example), there is, as already mentioned, a high resistive area next to the dry well. This is actually divided into two parts, because of the fault in the area. In this area, the discovery Drivis is being made (well 7220/7-3S). The Drivis discovery is shown in Figure 1.6.

Based on the map results, it seems like that it is not possible to achieve both small property misfits and model misfits at the same time. There is two options, and they are either to achieve small property misfits and big model misfits, or big property misfits and small model misfits. The ideal situation is to let the input models control the posterior distributions and let the prior distributions be wide, but only if the input models can be trusted. Five different cases were tested out in the thesis, and there are two main problems concerning the results. The two main problems are the quality of the input models and the forward model.

The first main problem are the input R_v and V_p models. The V_p are too low in the well locations where the V_p from the map can be compared with the V_p from the wells. The V_p is possibly too low in general, but it is impossible to confirm this without drilling everywhere. The V_p cube is not a perfect match with the wells because it is not calibrated to the wells and because an acoustic FWI workflow is being used. Another parameter that could influence the V_p from FWI is the value of the anisotropy (ε). It could be that the ε is too high, and therefore give lower V_p than the actual case. Another important aspect is how deep FWI could be used. The depth in the 7219/9-1T2 and 7220/7-1 wells are probably too deep to could use the full strength of FWI, and contributes to another error candidate. By looking at Figure B.3 in Appendix B, it is clearly visible that the FWI curve (red) is underestimating quite a lot in the reservoir interval. The area around the Skrugard well is more shallow, and it should not be a problem to get a good image of the subsurface here compared to the deeper areas around the two other wells. This is well illustrated to the left in Figure B.3, where the FWI curve can pick up the sudden change in V_p at 1270 m in the Skrugard well. The aim is, namely, that the FWI should manage to pick up those sudden changes in V_p (within it's resolution requirements to thickness) and therefore makes the V_p model more precise than the tomography V_p (blue). One day, the ultimate goal is that the V_p cube has resolution as close as possible to what is being measured in the well. In the two other deeper wells, the FWI is not able not pick up the rapid increase in V_p and this is probably due to the depth. The FWI cube was not build to fit into this specific workflow and has therefore a lot of improvements. It was originally made for research, and is therefore not calibrated to the wells.

In connection to the V_p cube, the R_v cube has also many possible reasons for the obtained results. As for the V_p, the comparison of TR between what is measured in the well and the extracted value from the well location in the map, is performed. When comparing the difference between the TR based on the well log and from the well location at the map, the differences are huge. The main reason to this is because the calculation of TR from well logs are based on R_t which is the same as the horizontal resistivity (R_h) in a vertical well, while the calculation of TR from well locations in the map are based on R_v. Other reasons are that the inversion is not perfect and the cube has another resolution than the well logs. The CSEM inversion is not able to make the extreme R_v values, because the CSEM method does not see a big difference between 500 Ωm and 1000 Ωm (an example). In the Skrugard well, the well is sitting a bit off the

strongest anomaly that is visible in the map, and this is because Skrugard is relatively narrow and the CSEM has not so good lateral resolution. The main point is that only the anisotropy will make this big TR misfit. One important question is which window to choose when there is no anomaly (as for the dry well). For the discovery wells 7220/7-1 and 7220/8-1, the TR is lower in the map as in the wells. When performing the CSEM inversion, the inversion is often performed in a conservative way, meaning that overestimation is trying to be avoided. The second reason is that the inversion does not manage to create the extreme resistivities (500-1000 Ωm). The response from a 500 Ωm area and from a 1000 Ωm is not always so big. Both 500 Ωm and 1000 Ω are hard to carry current through. There is a factor 2 in difference between the two discovery wells for TR based on the well logs. The values are almost the same for TR in the two wells based on the maps. The inversion can see that the reservoirs have very high resistivity, but the reason for why TR from the maps does not have the factor two in difference is probably because the response from a 500 Ωm or 1000 Ωm is possibly approximately the same when measuring at the surface. The saturation equal to 500 Ωm vs 1000 Ωm is very high, so it does not play a big role anyway. For the discovery wells, the TR is calculated from the Top Stø and down to the OWC. In theory, the TR could be calculated everywhere, but the problem is to know what to sum up. If something has very high resistivity, is relatively thin and big enough laterally, then the cheapest is to send the current vertically through. For the reservoir zones, this is the same as TR, or actually the integral of vertical resistivity, as if there was many series connected resistors in a curcuit. Therefore, it is normally only performed where there is an anomaly, and is used to estimate the saturation. The problem with the dry well without any anomaly, is that it is difficult to know that should be summed up (as for the discovery wells). Therefore, for the calculation of TR, the whole depth interval extracted from the R_v cube, is being used to calculate it. The CSEM inversion itself, smears out the TR from the reservoir with high resistivity over a bigger interval. This is done because it does not find the extreme values found in the discovery wells. Therefore, the whole interval from creation of the map is used to to find TR (no anomaly smeared out). The main reasons for this underestimation are, first, comparing the vertical and the horizontal component of the resistivity, second, the inversion is not able to make the extreme values of the resistivity, and third, because the inversion is performed conservative in order to avoid overestimation. Aspects that will affect the inversion results are how good the

calibration between R_v and the wells are, how close the initial model of R_v is to be the true model of R_v, the type of regularization (and the parameters), and to choose in general, the data that are connected to the wells and the depth intervals of interest.

Even if the TR of the $logR_v$ map is potentially underestimated (see Table 5.8), the S_{HC} are in the well locations, overestimated. As already discussed, the low V_p gives rise to high ϕ. How can underestimated TR give rise to overestimated S_{HC} (at least in the well locations) when the noise variance of the input models are low? At this point, the coupling of the methods plays an important role. By looking at Figure 5.15 c and d, both the ϕ and the S_{HC} are high. When the input V_p model is too low, it gives too high ϕ. The Archie equation tells then that the high resistivites have to be compensated by corresponding lower S_w in order to match those high resistivity responses. If the ϕ is not allowing to be so high (prior information), then the S_w does not have to be so low in order to produce the same resistivity response either. This is a part of the non uniqueness of inversion. Everything is connected, so even if TR is underestimated, the S_{HC} will be affected of the estimate of ϕ (and vice versa). After starting with low noise variance for the input models (the ideal situation is to trust the input models), and realizing that the inversion results are not reasonable, then the next step is to increase the noise variances. The goal is to find suitable values for noise variance in order to find something that gives both small property misfits and model misfits. At this point, the quality of the input models are being realized and in this case, indicating to be not good enough in this specific project.

The second main problem is about the forward modeling. In the forward modeling, the Archie equation is used and is only valid for clean sandstone (no clay). The $logR_v$ map is taken from a big interval (200 m above and 300 m below the Top Stø Fm) and is affected by shale. Both the overburden and the Hekkingen/Fuglen Fm have high shale content. The reservoir units (Stø and Nordmela Fm) have less shale (especially the Stø Fm) compared to the overburden. It is, strictly speaken, not correct to use the Archie equation here. The Waxman-Smits equation should be used instead to account for the shale. However, the Stø Fm is almost clean sandstone, so Archie equation should work here. The problem are the units containing higher amount of shale, as the Nordmela Fm.

The Han-Gassmann forward modeling is tuned in from the wells, while the V_p cube is not. To work with one part of the inversion that is tuned in from the wells and one that is not, makes it less accurate to work with. The V_p should at least be calibrated from the wells in order to get the potential out of it. It seems like that the forward modeling is assuming harder rock frame than the actual case, and if the clay content is accounted for, this will make the rock frame more soft and therefore reduce the modeled V_p.

Until now, the methods and their accuracy at the well locations have been discussed. There are also some minor factors that will affect the results. One of these is the different resolution in the input data. Due to different resolution for the $logRv$ and V_p cubes, different intervals were extracted from the two cubes. In addition to different resolution (frequency content) and the three main challenges discussed (physics, scale and sensitivity), there are other factors that affect the joint inversion of seismic and CSEM. Seismic has geometrical spreading, while CSEM has geometrical spreading and exponential damping. In addition to that, they have two different geometries for the data acquisition. The combination of those factors, makes the joint inversion challenging. Since it is challenging to decide what the optimal depth interval for each of the cubes are for this work, it is probably also a factor of uncertainty. The question is which depth interval should be chosen from the two cubes in order to account for the reservoir response. The depth intervals chosen for $logR_v$ and V_p are definitely of big importance for the outcome. There is high probability that the intervals extracted can be better chosen as in this thesis, by looking deeper into the relative resolution differences between the two methods. The Han-Gassmann model used the regressions from Han's study, but it would be more accurate to make new regression parameters based on logs and cores from the Johan Castberg area. Due to more than 1.5 km of uplift, smectite has been transformed to illite (removed the water from the smectite). All these different clay minerals make the forward modeling more complicated, but makes it even more important to really understand the clay processes happened. The importance the clay minerals have on the reservoir quality (porosity and permeability) is a crucial part of really understanding the reservoir.

6.2 Further work

Two main problems and some minor problems have already been pointed out. That means, that there is still a lot to do as future work to improve the results. First and foremost, the CSEM inversion and FWI workflows, as well as the forward model have to be improved.

Further CSEM inversion work should focus on the calibration to the wells, the initial model, the regularization type (and the parameters belonging to it) and choose data from the specific the wells and intervals of interest.

If, for FWI, TTI anisotropy, workflow for reflection based FWI, elastic forward modeling, multi-parameter updates and absorption modeling and updates could be included, it will give a way more accurate velocity model. This will make the V_p model way better than this acoustic V_p model used in this thesis.

Monte Carlo Markov Chain (MCMC) can be introduced in order to be able to invert for a third geophysical parameter (for example V_{cl}). In this case, a third input model has to be included (for example ρ), because the number of inversion properties and input models has to be the same (number of equations and number of unknowns the same). Archie equation should be replaced with Waxman-Smits (or equivalent) equation in order to account for the clay content. The introduction of cross-gradients could be useful. In this case, the structural similarities between $logR_v$ and V_p are being investigated and observe when the structural similarity between $logR_v$ and V_p reaches their maximum. When they reaches a maximum, the minimum of the cost function is being found, because a cross-gradient regularization is included in the cost function. Maybe even a combination of the approach used in this thesis and the use of cross-gradients will be possible?
More wells should be introduced, in order to tune in the forward modeling code more accurate. The is a strong need for a more robust rock-physics model. The more wells taken into account, the more knowledge about the actual geology in the area are being considered. Only the wells can tell with accuracy how the subsurface look like. More combinations of priors and noise variances of the input models should be tested out, to further improve the posterior distributions. To test out a two or even more stages prior, would be something to consider later on.

That means, vary the prior depending on knowledge knowing prior to the measurements for different depth intervals. There is maybe also possible to do something similar for the $logRv$ forward modeling (use Archie equation in sandstone areas and Waxman-Smits equation where it is shale) as well. As part of the calibration work, try to work further with the well logs. Not physical values should be removed and then only work with values that gives a physical meaning. In the wells, for every location that are logged, find the point that are closest to this point in depth compared to the depth registered on the data point in the well log. The Han-Gassmann model used the regressions from Han's study, but it would be more accurate to make new regression parameters based on logs and cores from the Johan Castberg area.

As seen, ρ improved the well logs results. Therefore, it would have been a good idea to get a ρ cube in order to combine this with the other two cubes. It is not trivial how to get the ρ, but the two options are either from the seismic or FTG. Since ρ made the well log inversion results better, it will probably also help the maps to become better (especially for ϕ). Another advantage by introducing ρ as a third inversion parameter, is that it may be able to distinguish between oil and gas. In this thesis, only water and HC have been considered, but in order to decide whether it is water, oil or gas this may be of huge importance. If V_{cl} could be inverted for (a third property), it would help to improve the forward modeling, because V_{cl} is input to the forward modeling code, and the inverted V_{cl} could be used in the Han-Gassmann velocity equation and Waxman-Smits equation to improve the forward modeling. This will hopefully make the model misfits smaller. A sensitivity analysis would be to recommend. By looking at the relative changes between the different parameters when changing some parameters, this would indicate which requirements would be needed to ask the CSEM inversion and FWI to strive for in order to get an improved inversion result. The relative weighting of the $logR_v$ and V_p models are something that need a closer look. The relative weighting is one of the most difficult things with joint inversion. This is more like experience than science. What is also worth to try out, is to use another inversion scheme than Bayesian inversion. The alternative inversion scheme to try out is the gradient-Hess inversion. This inversion is an optimization inversion algorithm (like CSEM inversion and FWI) and therefore do not use probability distributions. In stead, it is an iterative process minimizing the misfit function. One drawback of this method is that it do not get the posterior variance. In this case, the equivalence between the Bayesian inversion

(statistical) and gradient-Hess inversion (optimalization), is that minimize the misfit function is the same as maximize the probability distributions. In theory, it would be possible to do this joint inversion as one stage and not two stages as done in this thesis. The main drawback here is the computer power.

Chapter 7

Conclusions

The purpose of the thesis has been to investigate the feasibility of combining CSEM inversion and seismic FWI to estimate reservoir properties in petroleum exploration. The thesis has shown that the Bayesian petrophysical joint inversion works good for synthetic models and well log data. The workflow has been tested out, starting with synthetic models via well log data and finally map models. It has shown, for synthetic models, the importance of being careful when defining the noise variance of the input models. A too low noise variance may lead to bimodal MLH distributions. The confirmation of the feasibility of the method comes from the well logs. The Bayesian inversion works for the maps, but the inversion results and modeling results have some improvements. With the models provided, it is not possible for the maps to get small property and model misfits at the same time. Therefore, improvements of the input models of R_v and V_p, and the forward model have to be done. The question is still, if FWI one day will get the resolution required to achieve good enough inversion results. The improvement of the forward modeling is a much easier task, and should not be a problem to improve. If introducing clay in the forward modeling, this will probably improve it a lot. There will still be work to do when it comes to tuning of the parameters used in the Han-Gassmann model and Archie/Waxman-Smits equations. Even a clay free rock-physics model like Archie equation, has shown valuable results. Based on this thesis, it seems like that FWI has the potential to fit into this joint inversion workflow. The question is, will FWI be able to substitute AVO in the future, lets say within 10 years time? This is our prediction, namely that it would be a good candidate to do so, and there will be exciting to see what the future will bring.

Bibliography

Alvarez, P., Marcy, F. A., Vrijlandt, M., Skinnemoen, O., MacGregor, L., Nichols, K., Keirstead, R., Bolivar, F., Bouchrara, S., Smith, M., Tseng, H. W. and Rappke, J. (2018). Multiphysics characterization of reservoir prospects in the Hoop area of the Barents Sea, *Interpretation* **6**(3): 1141–1152.

Archie, G. (1942). Fundamentals of seismic rock physics, *Petroleum Transactions of AIME* **146**: 54–62.

Biot, M. A. (1956). Theory of propagation of elastic waves in a fluid saturated porous solid, I. low frequency case and II. higher-frequency range, *The Journal of Acoustical Society of America* **28**(2): 168–178.

Bjørlykke, K. (2015). *Petroleum Geoscience: From Sedimentary Environments to Rock Physics*, Springer, chapter Well Logs: A Brief Introduction.

Blaich, O. A., Tsikalas, F. and Faleide, J. I. (2017). New insights into the tectono-stratigraphic evolution of the southern Stappen high and its transition to Bjørnøya Basin, SW Barents Sea., *Marine and Petroleum Geology* **85**: 89–105.

Buland, A., Løseth, L., Becht, A., Roudot, M. and Røsten, T. (2011). The value of CSEM data in exploration, *First Break* **29**(4): 69–76.

Carazzone, J., Burtz, J., Green, K. and Pavlov, D. (2005). Three Dimensional Imaging of Marine CSEM Data, *SEG Technical Program Expanded Abstracts* pp. 575–578.

Carcione, L. M., Herman, G. C. and ten Kroode, A. P. E. (2002). Seismic modeling, *Geophysics* **67**(4): 1304–1325.

Castagna, J. P., Batzle, M. L. and Kan, T. K. (1993). *In offset-dependent Reflectivity: Theory and Practice of AVO Analysis*, Society of Exploration Geophysicists, Tulsa, Oklahoma, chapter Rock Physics - The Link Between Rock Properties and AVO Response.

Claerbout, J. F. (1985). *Imaging the Earth's interior*, Blackwell Science Inc.

Clavier, C., Coates, G. and Dumanoir, J. (1984). Theoretical and experimental bases for the dual-water model for interpretation of shaley sands, *Society of Petroleum Engineers Journal* **24**(2): 153–168.

Constable, S. (2010). Ten years of marine CSEM for hydrocarbon exploration, *Geophysics* **75**(5): 75A67–75A81.

Cowell, R., Dawid, P., Lauritzen, S. and Spiegelhalter, D. (2007). *Probabilistic networks and expert systems: exact computational methods for Bayesian networks. In Statistics for engineering and information science series*, Springer, New York, United States.

Dalland, A., Worsley, D. and Ofstad, K. (1988). A lithostratigraphic scheme for the Mesozoic and Cenozoic succession offshore mid- and northern Norway., *Technical report*, NPD.

Devore, J. L. and Berk, K. N. (2012). *Modern Mathematical Statistics with Applications*, Springer, chapter Continuous Random Variables and Probability Distributions.

Dore, A. G. (1995). Barents Sea geology, petroleum resources and commercial potential., *Arctic* **48**(3): 207–221.

Ellingsrud, S., Eidesmo, T., Johansen, S., Sinha, M., MacGregor, L. and Constable, S. (2002). Remote sensing of hydrocarbon layers by seabed logging (SBL): Results from a cruise offshore Angola, *The Leading Edge* **21**(10): 972–982.

Equinor (2018). The Johan Castberg FPSO - sea ice and iceberg risks., *Technical report*, Equinor.

Faleide, J. I., Bjørlykke, K. and Gabrielsen, R. H. (2015). *Petroleum Geoscience: From Sedimentary Environments to Rock Physics*, Springer, chapter Geology of the Norwegian Continental Shelf.

Gallardo, L. A. and Meju, M. A. (2003). Characterization of heterogeneous near-surface materials by joint 2d inversion of dc resistivity and seismic data, *Geophysical Research Letters* **30**(13): 1–4.

Gassmann, F. (1951). Über die Elastizität poröser Medien, *Vierteljahrsschrift der Naturforschenden Gesellschaft in Zürich* **96**: 1–23.

Halland, E., Mujezinovic, J. and Riis, F. (2013). Co2 Storage Atlas Barents Sea., *Technical report*, NPD.

Han, D., Nur, A. and Morgan, D. (1986). Effects of porosity and clay content on wave velocities in sandstones, *Geophysics* **51**(11): 2093–2107.

Harris, P., Du, H., Soleng, H. and MacGregor, L. (2009). Rock physics integration of CSEM and seismic data: A case study based on the Luva gas field, *SEG Technical Program Expanded Abstracts* pp. 1741–1745.

Henriksen, E., Ryseth, A. E., Larssen, G. B., Heide, T., Rønning, K., Sollid, K. and Stoupakova, A. V. (2011). *Arctic Petroleum Geology.*, Geological Society, London, Memoirs, chapter Tectonostratigraphy of the greater Barents Sea: implications for petroleum systems.

Hokstad, K., Tosarova, Z. A., Clark, S. A., Kyrkjebø, R., Duffaut, K., Fichler, C. and Wiik, T. (2017). Radiogenic heat production in the crust from inversion of gravity and magnetic data, *Norwegian Journal of Geology* **97**(3): 191–204.

Hokstad, K. and Tänavsuu-Milkeviciene, K. (2017). Temperature prediction by multigeophysical inversion: Application to the IDDP-2 Well at Reykjanes, Iceland, *GRC Transactions* **41**: 1141–1152.

Hoversten, G. M., Cassassuce, E., Gasperikova, G. A., Newman, J., Chen, Y., Rubin, Z. and Vasco, D. (2006). Direct reservoir parameter estimation using joint inversion of marine seismic AVA and CSEM data, *Geophysics* **71**(3): C1–C13.

Keller, G. V. (1982). *Handbook of Physical Properties of Rocks*, CRC Press, chapter Electrical properties of rocks and minerals.

Krief, M., Garat, J., Stellingwerff, J. and Ventre, J. (1990). A petrophysical interpretation using the velocities of P and S waves (full-waveform sonic), *The Log Analyst* **31**(6): 355–369.

Lundteigen, M. A. and Rausand, M. (2008). Spurious activation of safety instrumented systems in the oil and gas industry: Basic concepts and formulas, *Reliability Engineering and System Safety* **93**: 1208–1217.

Malinverno, A., Andrews, B., Bennett, N., Bryant, I., Prange, M., Savundaraj, P., Bornermann, T., Raw, I., Britton, D. and Peters, J. G. (2002). Real-Time 3D Earth Model Updating While Drilling a Horizontal Well, *SPE* pp. 1–11.

Marfurt, K. J. (1984). Accuracy of finite-difference and finite-element modeling of the scalar and elastic wave equations., *Geophysics* **49**(5): 533–549.

Mavko, G., Mukerji, T. and Dvorkin, J. (2009). *The Rock Physics Handbook*, Cambridge University Press, chapter Seismic wave propagation.

Mondol, N. H. (2015). *Petroleum Geoscience: From Sedimentary Environments to Rock Physics*, Springer, chapter Well Logging: Principles, Applications and Uncertainties.

Nordskag, J. I., Kjøsnes, , Nguyen, A. K. and Hokstad, K. (2013). CSEM exploration in the Barents Sea: Joint CSEM Seismic interpretation., *SEG Technical Program Expanded Abstracts* pp. 810–814.

NPD (2019a). Factpages. Norwegian Petroleum Directorate. Accessed: 2019-02-04.
URL: *http://factpages.npd.no/FactPages/Default.aspx?culture=en*

NPD (2019b). Map of the norwegian continental shelf. Accessed: 2019-01-27.
URL: *http://www.npd.no/Global/Norsk/4-Kart/Sokkelkart2018/Sokkelkartet2018-Arealstatus.pdf*

Nur, A. (1992). Critical porosity and the seismic velocities in rocks, *EOS, Transactions, American Geophysical Union* **73**: 43–66.

Ohm, S. E., Karlsen, D. A. and Austin, T. J. F. (2008). Geochemically driven exploraion models in uplifted areas: Example from the Norwegian Barents Sea., *AAPG Bulletin* **92**(9): 1191–1223.

Salem, H. S. and Chilingarian, G. V. (1999). The cementation factor of archie's equation for shaly sandstone reservoirs, *Journal of Petroleum Science and Engineering* **23**: 83–93.

Sen, M. K. and Stoffa, P. L. (1996). Bayesian inference, Gibbs' sampler and uncertainty estimation in geophysical inversion, *Geophysical Prospecting Journal* **44**: 313–350.

Smith, T. M., Sondergeld, C. H. and Rai, C. S. (2003). Gassmann fluid substitution: A tutorial, *Geophysics* **68**(2): 430–440.

Statoil (2013). Internal.

Statoil (2017). Submitting plan for development and production, and awarding Johan Castberg contracts. Accessed: 2019-01-15.
URL: *https://www.equinor.com/en/news/05dec2017-johan-castberg.html*

Statoil (2018). Oil discovery north of the Johan Castberg field in the Barents Sea - 7220/5-3. Accessed: 2019-02-11.
URL: *http://www.npd.no/en/news/Exploration-drilling-results/2018/72205-3/*

Stefatos, A., Vereshagin, A., Hesthammer, J., Kalstø, T., Sperrevik, K. and Robson, A. (2014). CSEM-driven exploration over the Nordland Ridge., *Interpretation* **2**(3): SH79–SH95.

Tarantola, A. (1987). *Inverse problem theory: Methods for data fitting and model parameter estimation*, Elsevier, United States.

Ulrych, T. J., Sacchi, M. D. and Woodbury, A. (2001). A bayes tour of inversion: A tutorial, *Geophysics* **66**(31): 55–69.

Virieux, J. and Operto, S. (2009). An overview of full-waveform inversion in exploration geophysics, *Geophysics* **74**(6): WCC127–WCC152.

Wang, Z. (2001). Fundamentals of seismic rock physics, *Geophysics* **66**: 398–412.

Waxman, M. H. and Smits, M. J. L. (1968). Electrical conductivities in oil-bearing shaly sands, *SPE Journal* **8**(2): 107–122.

Winsauer, W. O., Shearin, A. M., Masson, P. H. and Williams, M. (1952). Resistivities of brine saturated sands in relation to pore geometry, *Bulletin of the american association of petroleum geologists* **36**(2): 253–277.

Yanagisawa, H., Kawamata, O. and Ueda, K. (2019). Modeling Emotions Associated With Novelty at Variable Uncertainty Levels: A bayesian Approach, *Frontiers in Computational Neuroscience* **13**(2): 1–9.

Zohdy, A. A. R., Eaton, G. P. and Mabey, D. R. (1974). Application of surface geophysics to groundwater investigations, *Technical report*, U.S. Dept. of the Interior, Geological Survey.

Appendix A

Rock-physics modeling

A.1 Forward modeling parameters

Table A.1: Tuning parameters from well logs.

R_w [Ωm]	K_w [Pa]	ρ_g [g/cm^3]	ρ_w [g/cm^3]
0.06	2.93e9	150.5	1061

Table A.2: Parameters in the forward modeling not being tuned from well logs.

Parameter	Value
a [-]	1
n [-]	2.0
m [-]	1.8
β [-]	0.6
K_{oil} [Pa]	1.2e9
ρ_{oil} [g/cm^3]	800
g [m/s^2]	9.82
ρ_{avg} [g/cm^3]	2300
T_g [°C/m]	38e-3
K_g [Pa]	0.83e9
ρ_{ma} [g/cm^3]	2640
K_{ma} [Pa]	38e9

A.2 Forward model calibration and high frequency well logs

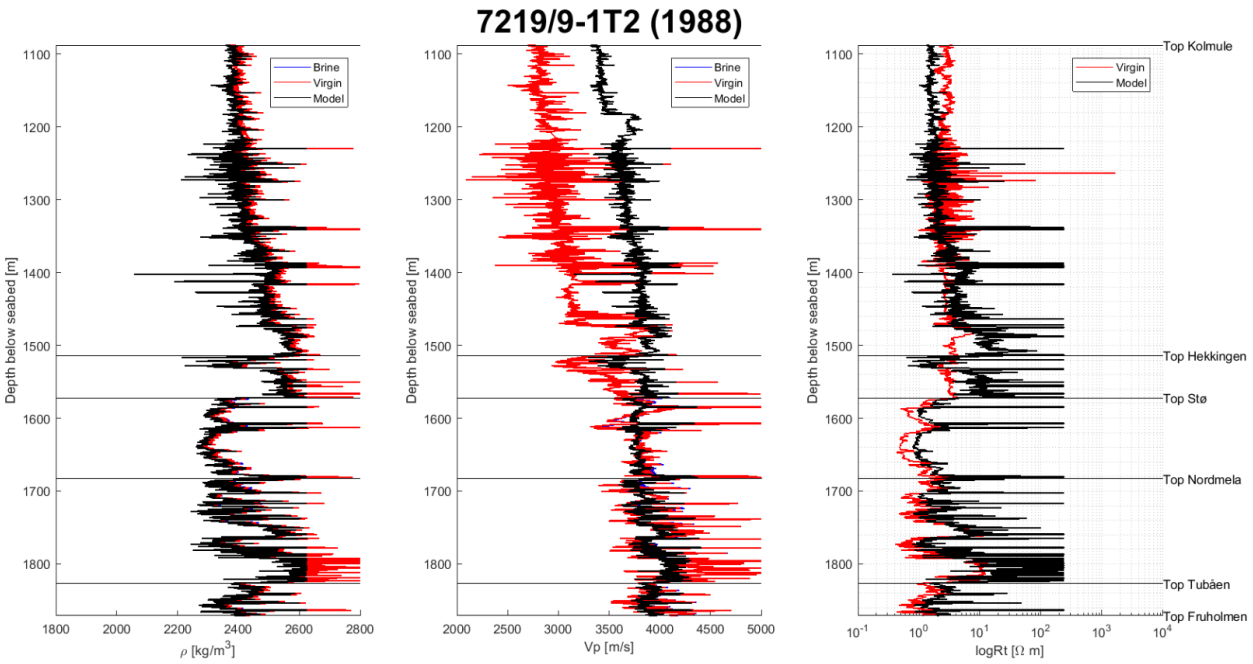

Figure A.1: Well logs of ρ, V_p and $logR_t$ for well 7219/9-1T2. Brine = blue, virgin = red and model = black.

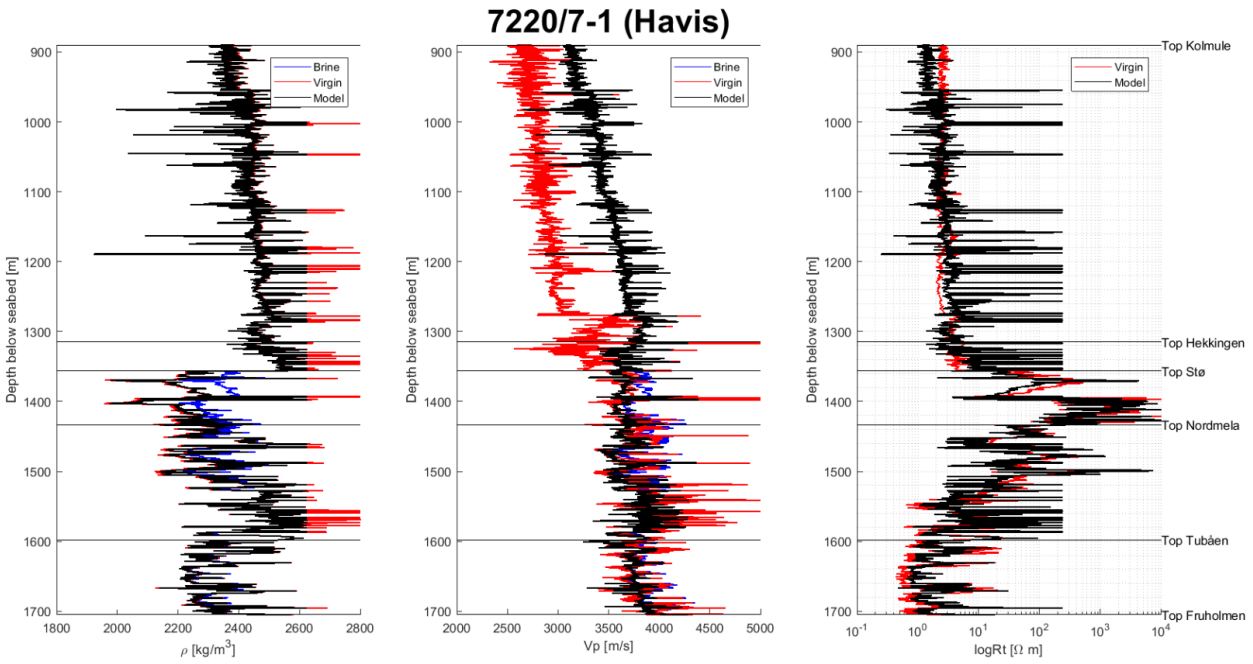

Figure A.2: Well logs of ρ, V_p and $logR_t$ for well 7220/7-1. Brine = blue, virgin = red and model = black.

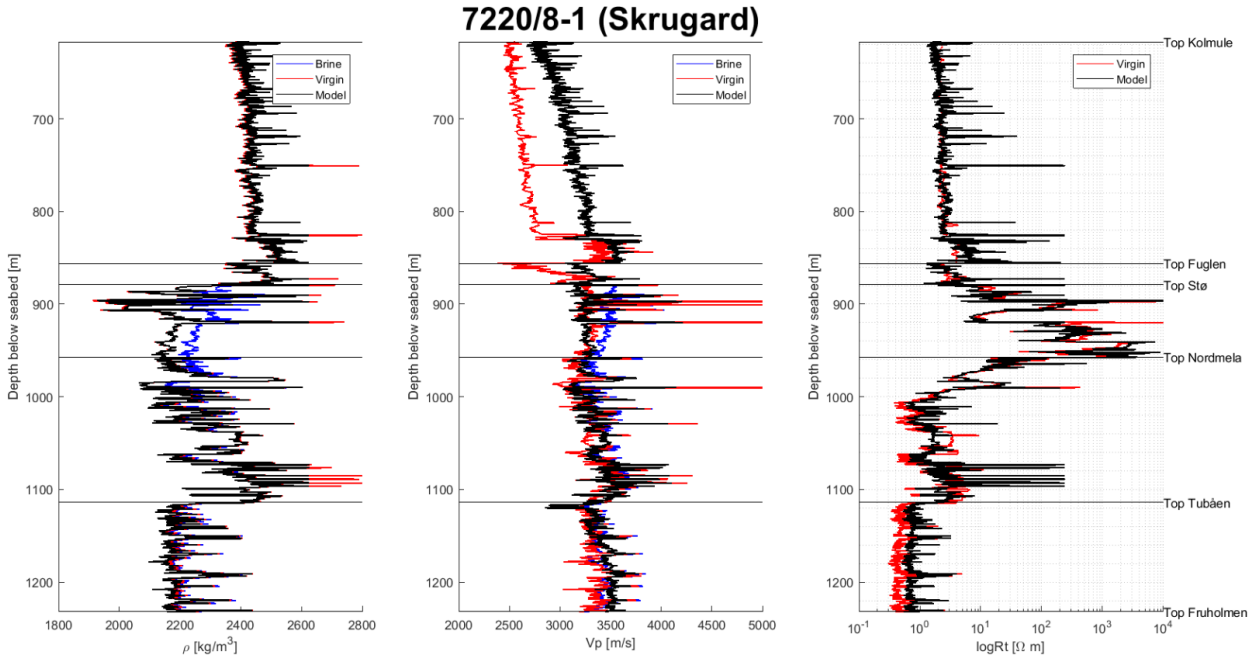

Figure A.3: Well logs of ρ, V_p and $logR_t$ for well 7220/8-1. Brine = blue, virgin = red and model = black.

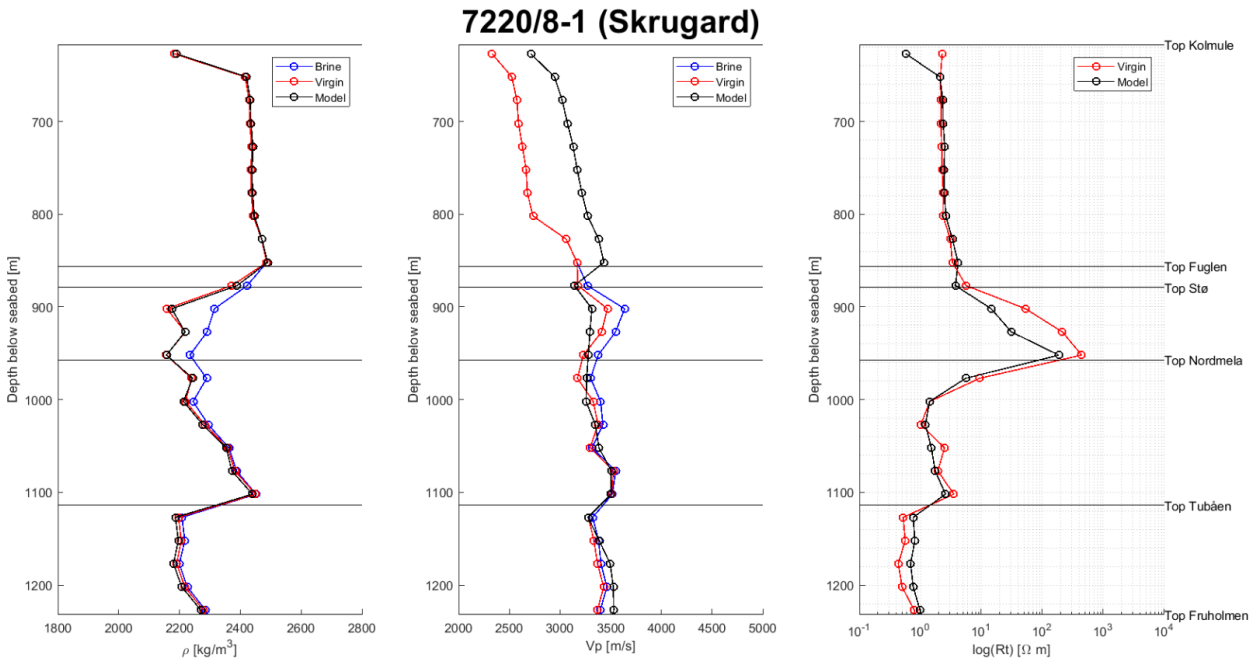

Figure A.4: Regular blocked well logs of ρ, V_p and $logR_t$ for well 7220/8-1. Brine=blue, virgin=red and model=black.

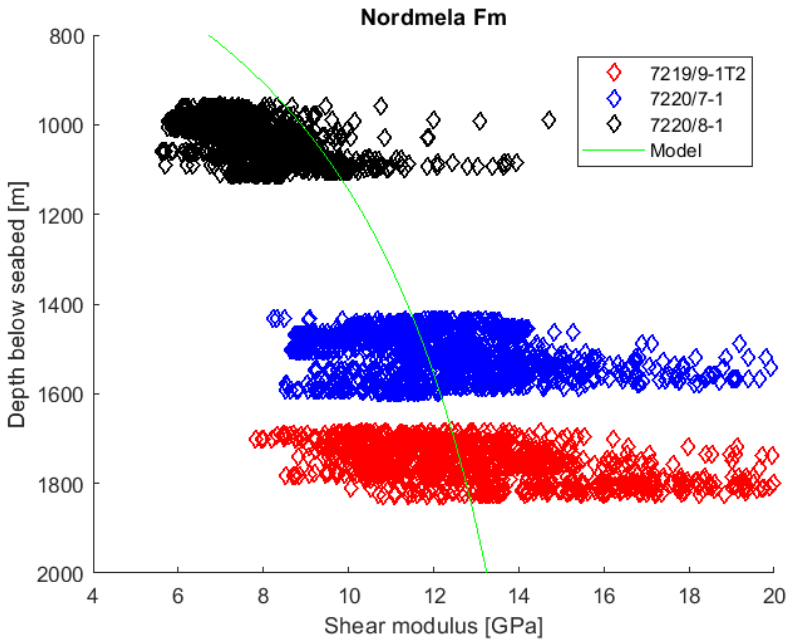

Figure A.5: Shear modulus for the different wells for the Stø Fm. The green model curve is the temperature dependent dry shear modulus.

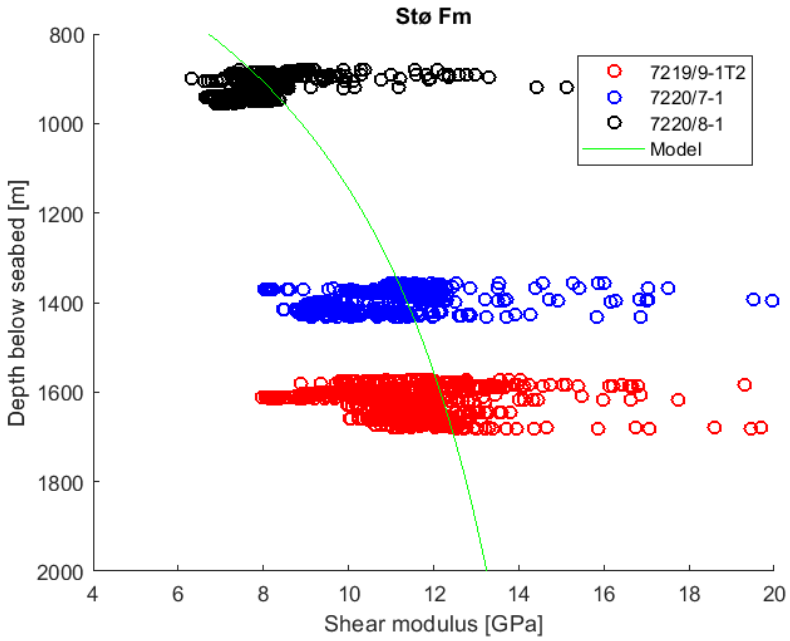

Figure A.6: Shear modulus for the different wells for the Nordmela Fm. The green model curve is the temperature dependent dry shear modulus.

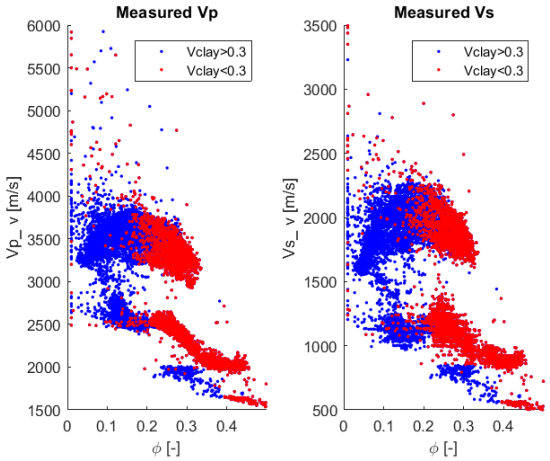

Figure A.7: Measured velocities vs porosity plotted as blue (V_{cl}>0.3) and red (V_{cl}<0.3).

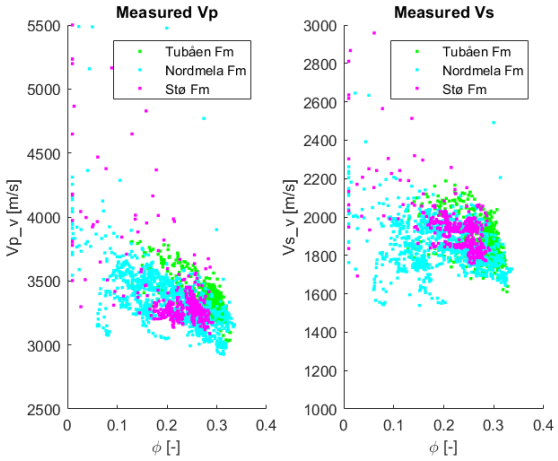

Figure A.8: Measured velocities vs porosity plotted as the formation contributions.

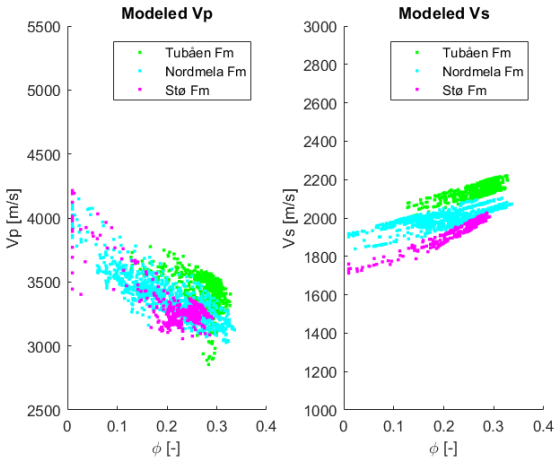

Figure A.9: Modeled velocities vs porosity plotted as the formation contributions.

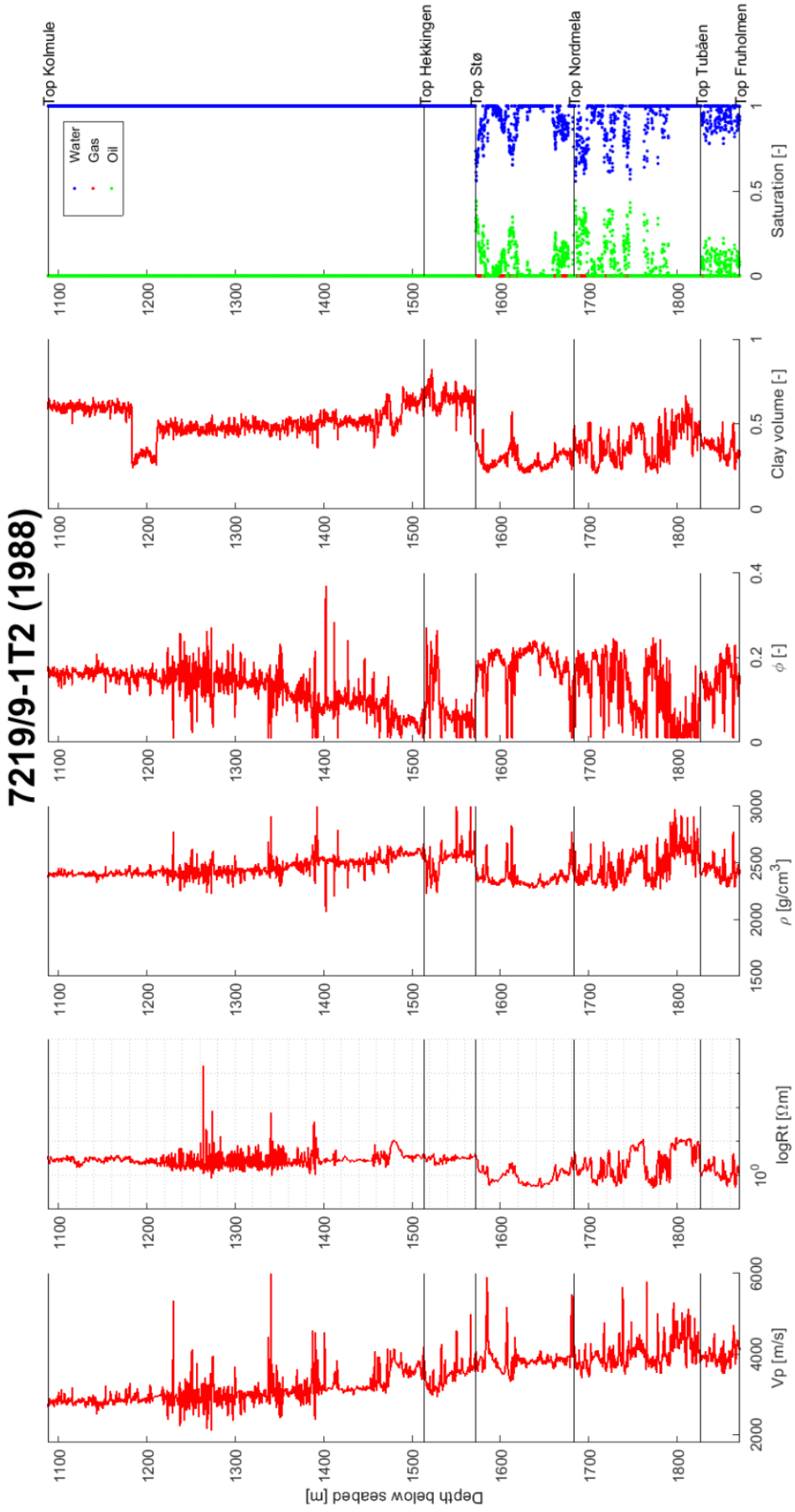

Figure A.10: Well logs for well 7219/9-1T2.

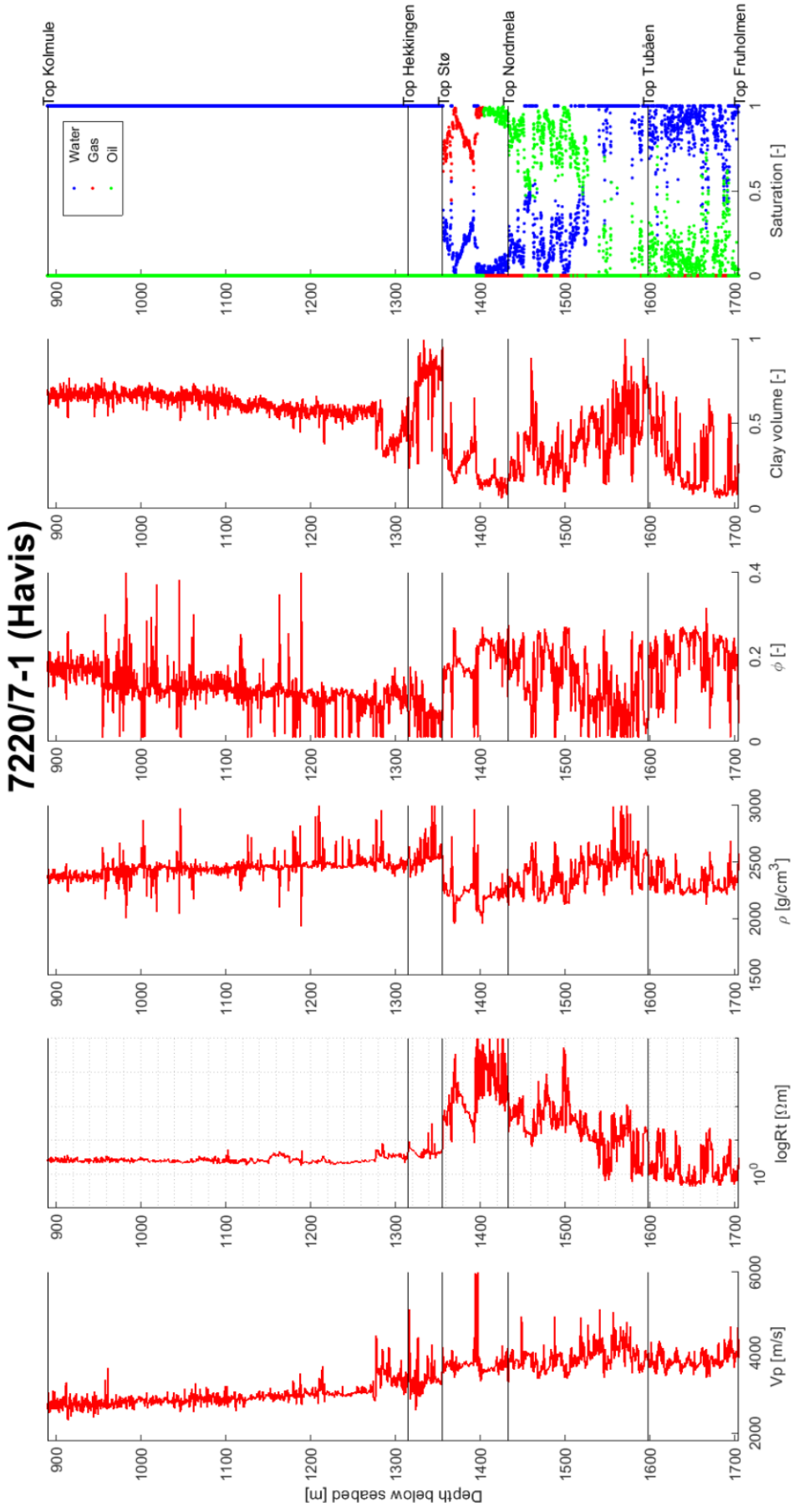

Figure A.11: Well logs for well 7220/7-1.

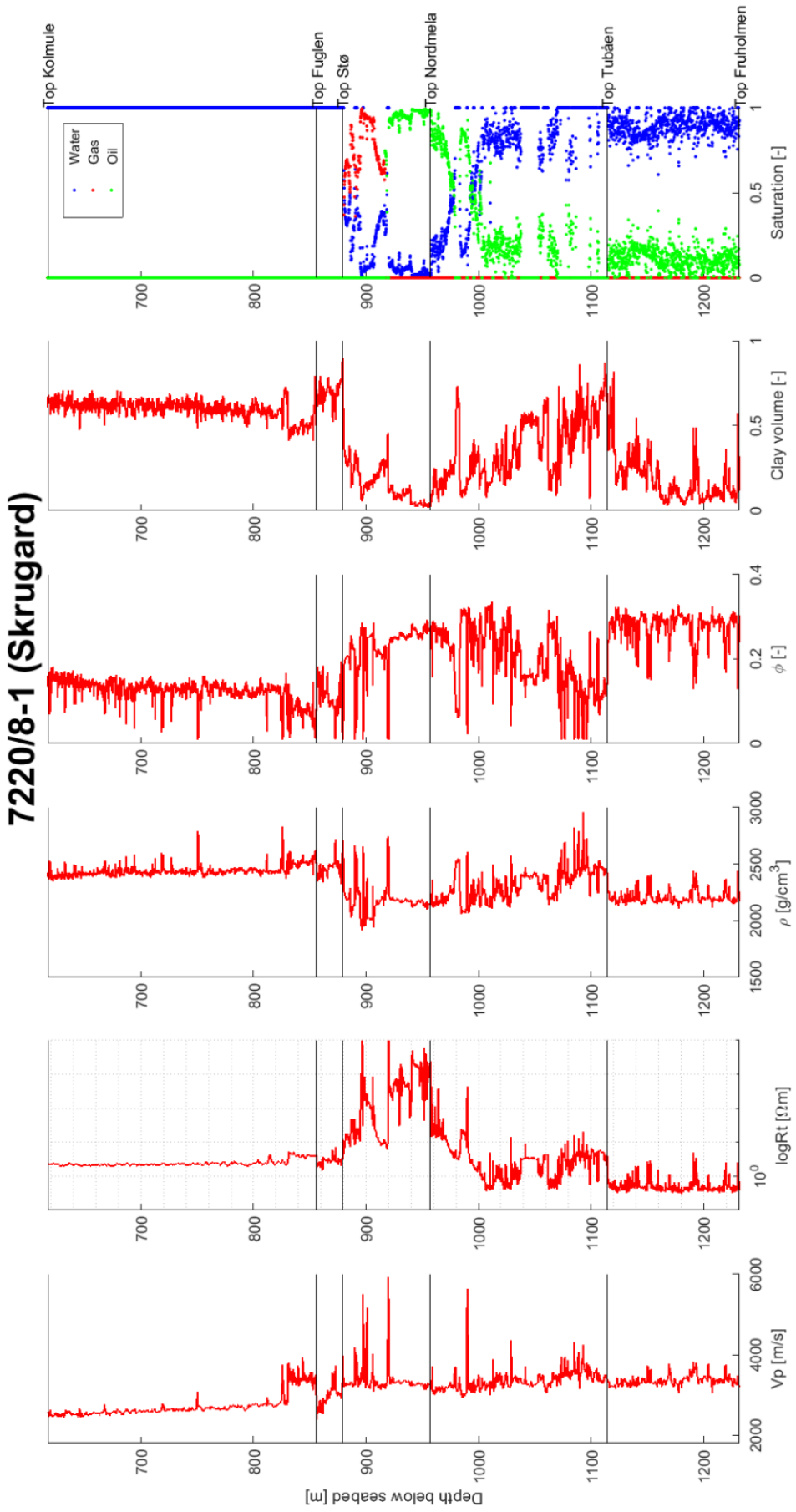

Figure A.12: Well logs for well 7220/8-1.

Appendix B

Analysis of velocity models

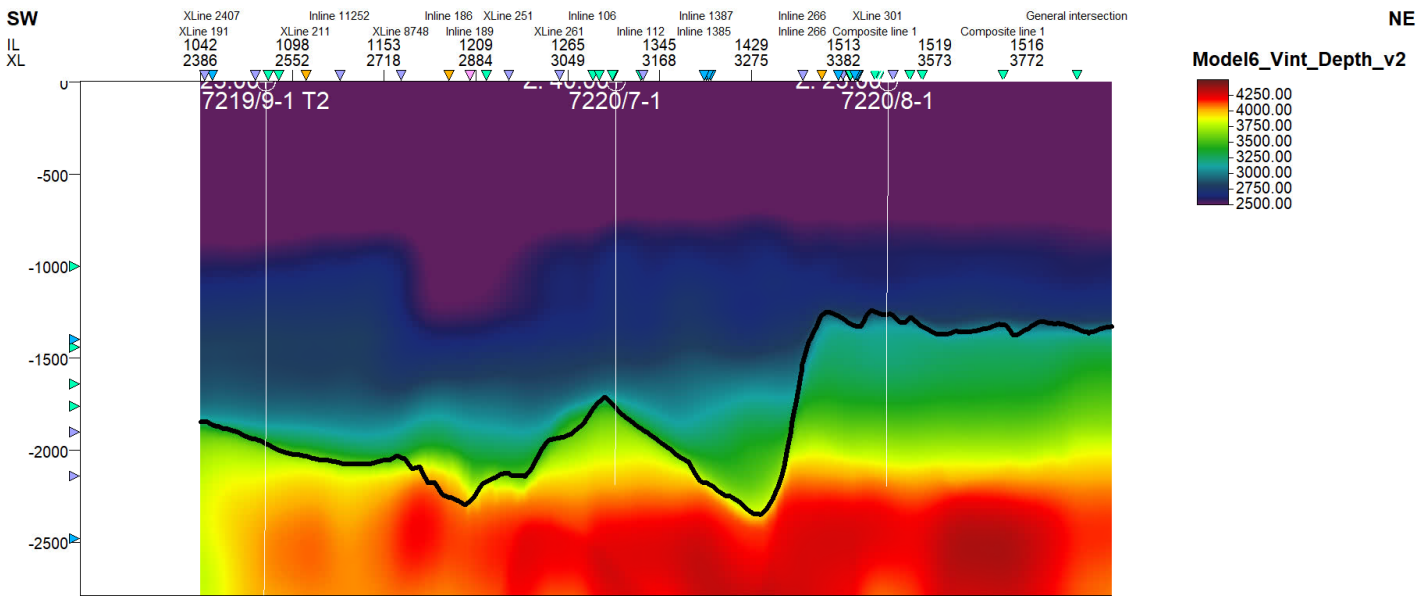

Figure B.1: Tomography interval velocity model (calibrated to the wells).

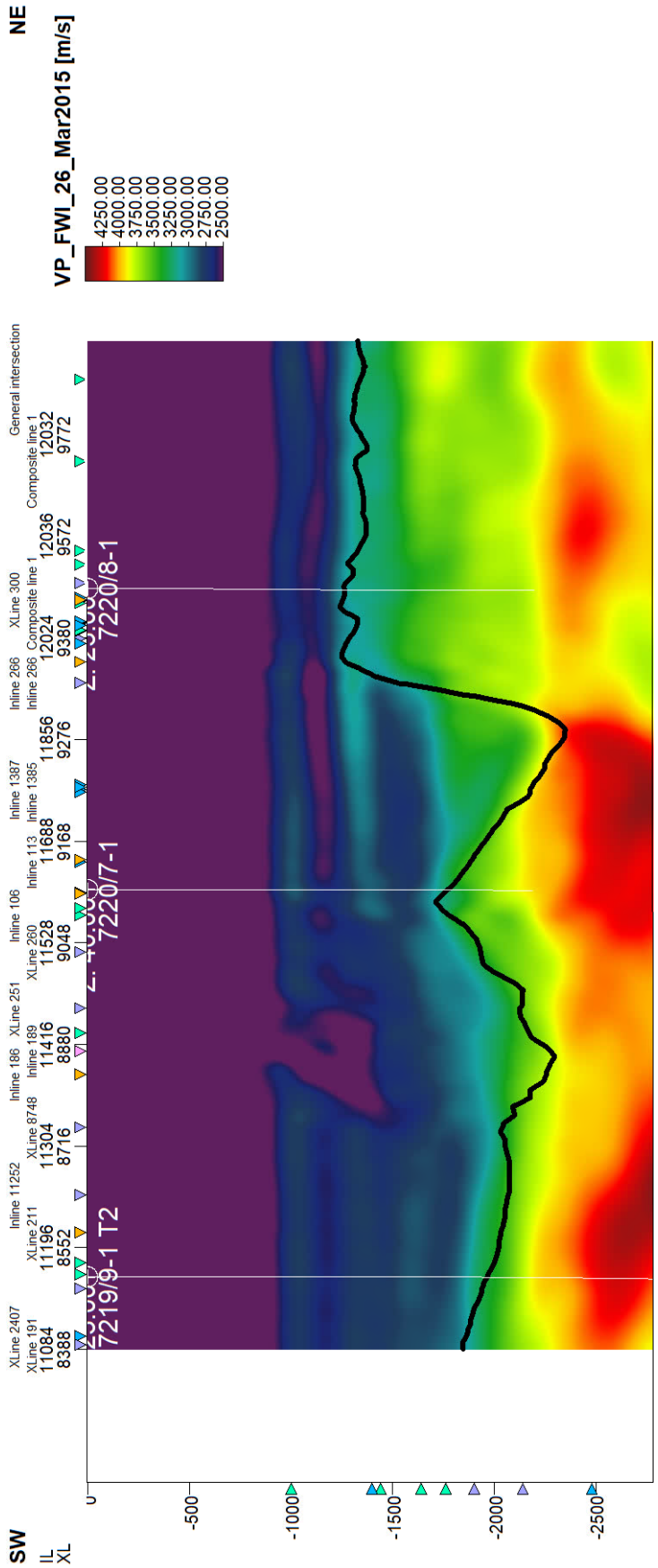

Figure B.2: FWI velocity model (not calibrated to the wells).

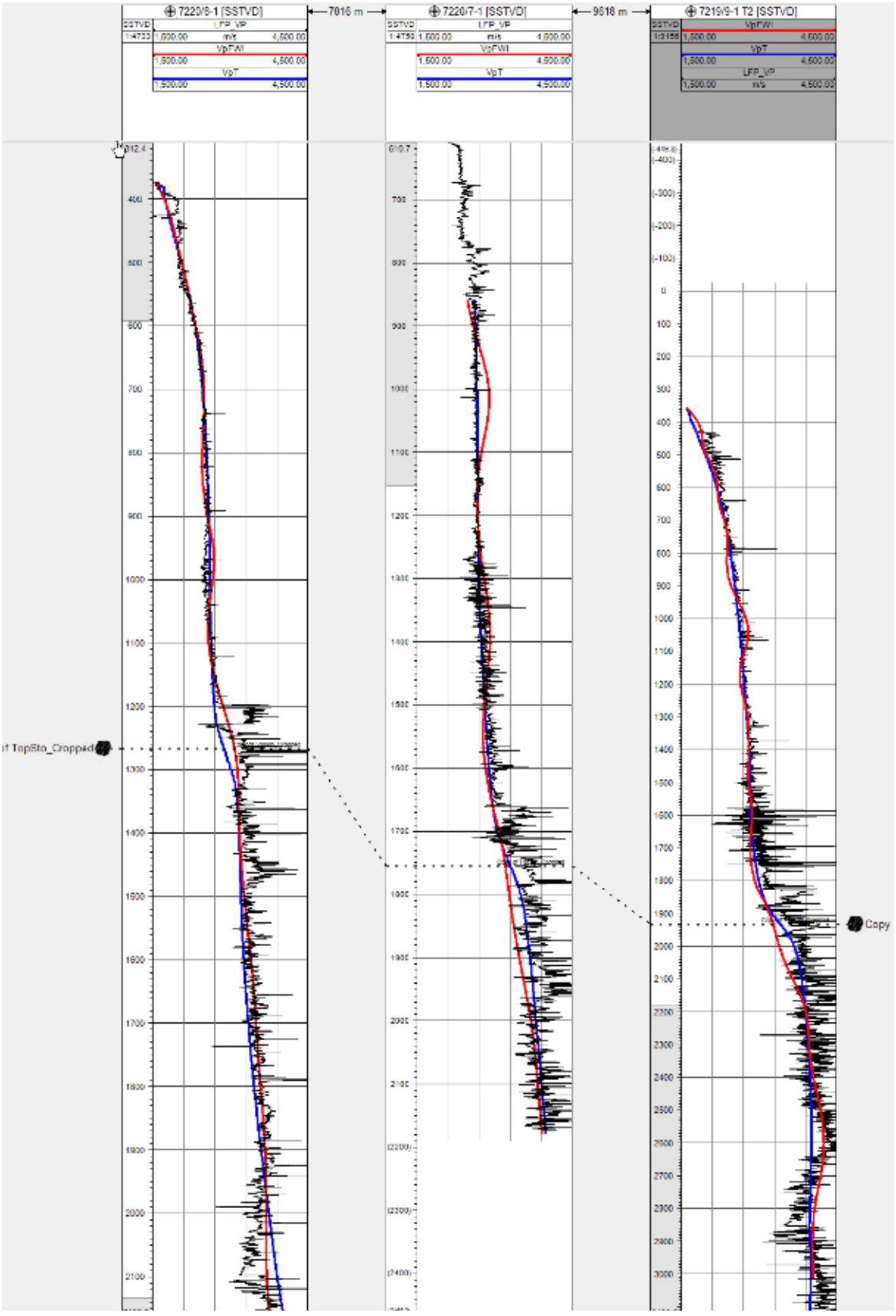

Figure B.3: Comparison of the velocities from tomography (blue), FWI (red) and the well log (black) for the studied wells.

Appendix C

Matlab code

C.1 Synthetic models

C.1.1 Synthetic model

Creates the synthetic model used in the inversion.

```
clear all; % Delete everything
close all; % Close everything

dx = 25; % Horizontal increment length [m]
dz = 12.5; % Vertical increment length [m]
x = 0:dx:800; % Offset [m]
z = 800:dz:1600; % Depth [m]
nx = length(x); % Number of offset increments
nz = length(z); % Number of depth increments
phi = 0.12*ones(nz,nx); % Phi outside the reservoir
phi(30:38,:) = 0.2; % Phi in the reservoir
Sw = ones(nz,nx); % Sw outside the reservoir
Sw(30:38,:) = 0.2; % Sw in the reservoir
SatPor.dx = dx; % dx struct
SatPor.dz = dz; % dz struct
SatPor.nx = nx; % nx struct
SatPor.nz = nz; % nz struct
```

```
SatPor.x = x; % x struct
SatPor.z = z; % z struct
SatPor.phi = phi; % phi struct
SatPor.Sw = Sw; % Sw struct

save ('test.mat', 'SatPor'); % Save as .mat file
```

C.1.2 Forward modeling

Forward modeling of synthetic models.

```
function [logRv, Vp] = Forward_modeling_synt(S_water, phi)
%  Forward model using Archie and Gassmann models, calculating Vp and
%  logRv. Valid for clean sandstone.
%
%   Input:
%      S_water: Water saturation
%      phi: Porosity
%
%   Output:
%      Vp: P-wave velocity
%      logRv: Vertical resistivity

logRv=0; Vp=0; % Initial values

% Archie parameters (fixed)
a = 1.0; % Turtousity factor
R_water = 0.06; % Water resistivity
sig_water = 1/R_water; % Water conductivity
n = 2.0; % Saturation exponent
m = 1.8; % Porosity exponent

% Gassmann parameters (fixed)
K_matrix = 38e9; % Mineral bulk modulus sandstone
K_oil = 1.20e9; % Bulk modulus oil
```

```
25 K_water = 2.93e9; % Bulk modulus water
26 rho_matrix = 2640; % Mineral density sandstone
27 rho_water = 1061; % Water density
28 rho_oil = 800; % Oil density
29
30 % Independent of fluid:
31 mu_dry = 2.88e9; % Corresponding to Vs=1200 and rho=2000
32 K_gas = 0.83e9; % Just a guess
33 rho_gas = 150.5; % Gas density
34 B = 0.80; % Biot coefficient
35
36 K_dry = (1-B)*K_matrix; % Dry rock sandstone
37
38 for k=1:length(S_water)
39    S_HC(k) = 1.0*(1-S_water(k)); % HC saturation
40
41    % Compute Archie
42    R_sat(k) = (a*R_water)/(phi(k)^m*S_water(k)^n); % True formation ...
          resistivity
43    logRv(k) = log10(R_sat(k)); % log(R_sat)
44
45    % Compute Gassmann
46    rho_fluid_gas = S_water(k)*rho_water + S_HC(k)*rho_gas; % Density water ...
          and gas
47    rho_fluid_oil = S_water(k)*rho_water + S_HC(k)*rho_oil; % Density water ...
          and oil
48    rho_sat_gas(k) = (1-phi(k))*rho_matrix + phi(k)*rho_fluid_gas; % Bulk ...
          density gas
49    rho_sat_oil(k) = (1-phi(k))*rho_matrix + phi(k)*rho_fluid_oil; % Bulk ...
          density oil
50    KI_fluid_gas = S_water(k)/K_water + S_HC(k)/K_gas; % Bulk modulus fluid ...
          mixture
51    KI_fluid_oil = S_water(k)/K_water + S_HC(k)/K_oil; % Bulk modulus fluid ...
          mixture
52    K_sat_gas = K_dry + B*B/((B-phi(k))/K_matrix + phi(k)*KI_fluid_gas); % ...
          Bulk modulus gas
```

```
53    K_sat_oil = K_dry + B*B/((B-phi(k))/K_matrix + phi(k)*KI_fluid_oil); % ...
          Bulk modulus oil
54    Vp_sat_gas(k) = sqrt((K_sat_gas + (4/3)*mu_dry)/rho_sat_gas(k)); % Vp ...
          for gas
55    Vp_sat_oil(k) = sqrt((K_sat_oil + (4/3)*mu_dry)/rho_sat_oil(k)); % Vp ...
          for oil
56    Vp(k) = Vp_sat_oil(k); % P-wave velocity for oil used as input for ...
          inversion
57    Vs_sat_gas(k) = sqrt((mu_dry)/rho_sat_gas(k)); % Vs for gas
58    Vs_sat_oil(k) = sqrt((mu_dry)/rho_sat_oil(k)); % Vs for oil
59    VpVs_sat_gas(k) = Vp_sat_gas(k)/Vs_sat_gas(k); % Vp/Vs ratio for gas
60    VpVs_sat_oil(k) = Vp_sat_oil(k)/Vs_sat_oil(k); % Vp/Vs ratio for oil
61    IP_sat_gas(k) = rho_sat_gas(k)*Vp_sat_gas(k); % Acoustic impedance for gas
62    IP_sat_oil(k) = rho_sat_oil(k)*Vp_sat_oil(k); % Acoustic impedance for oil
63    end % for
64 end % function
```

C.1.3 Inversion

Inversion of the synthetic models.

```
1  %  Synthetic case:
2  %  Calculating water saturation (Sw) and porosity (phi) from resistivity ...
       (Rv) and P-wave velocity (Vp)
3
4  clear all; % Delete everything
5  close all; % Close everything
6
7  %-------------------
8  % Load the inputs
9  %-------------------
10
11 load test % load the model
12
13 % Add 5% noise to Sw
```

```
noisesigma_Sw = 0.05*SatPor.Sw;
SatPor.Sw = SatPor.Sw + noisesigma_Sw.*randn(size(SatPor.Sw));
SatPor.Sw(SatPor.Sw>1) = 1;
SatPor.Sw(SatPor.Sw<0.01) = 0.01;

% Add 5% noise to phi
noisesigma_phi = 0.05*SatPor.phi;
SatPor.phi = SatPor.phi + noisesigma_phi.*randn(size(SatPor.phi));
SatPor.phi(SatPor.phi>1) = 1;
SatPor.phi(SatPor.phi<0.01) = 0.01;

% Calculate logRv and Vp
for iz = 1:SatPor.nz
   [SatPor.logRv(iz,:), SatPor.Vp(iz,:)] = ...
      Forward_modeling_synt(SatPor.Sw(iz,:), SatPor.phi(iz,:));
end % for

%-----------
%  Tests
%-----------

% Relevant for joint inversion
% ktest = 1; % Use logRv only
% ktest = 2; % Use Vp only
  ktest = 3; % Use Vp and logRv (all models)

disp(strcat('ktest=',num2str(ktest))); % Write to the screen which test

%-----------------------------------------
%  Make one mesh for Sw and one for phi
%-----------------------------------------

Swmin = 0.01; % Minimum Sw
Swmax = 1; % Maximum Sw
MC.nSw = 100; % Number of elements for Sw
MC.dSw = (Swmax-Swmin)/(MC.nSw-1); % Increment length
```

```
MC.Sw = [Swmin:MC.dSw:Swmin+(MC.nSw-1)*MC.dSw]'; % Sw
phimin = 0.01; % Minimum phi
phimax = 0.5; % Maximum phi
MC.nphi = 50; % Number of elements for phi
MC.dphi = (phimax-phimin)/(MC.nphi-1); % Increment length
MC.phi = [phimin:MC.dphi:phimin+(MC.nphi-1)*MC.dphi]'; % Phi

% Make grid of all model parameter combinations (not only pairwise)
[AA,BB] = meshgrid(MC.Sw,MC.phi);
aa = reshape(AA,size(AA,1)*size(AA,2),1); % Reshape grid into vector
bb = reshape(BB,size(BB,1)*size(BB,2),1);
MC.Sw = aa;
MC.phi = bb;

%---------------------------------
%   Simulate once and for all
%---------------------------------

[ MC.logRv, MC.Vp] = Forward_modeling_synt(MC.Sw, MC.phi);

%---------------------------------
%  Prior for Sw
%---------------------------------

PRI.muSw = 0.7;  % Prior mean for Sw
PRI.stdSw = 0.5; % Prior std.dev for Sw
PRI.pdfSw = mvnpdf(MC.Sw,PRI.muSw,PRI.stdSw^2); % Multivariate normal ...
    probability density function for Sw

%-------------------------
%  Prior for phi
%-------------------------

PRI.muphi = 0.2; % Prior mean for phi
PRI.stdphi = 0.3; % Prior std.dev for phi
```

```
83 PRI.pdfphi = mvnpdf(MC.phi,PRI.muphi,PRI.stdphi^2); % Multivariate normal ...
       probability density function for phi
84
85 % Reshape pdf back to grid shape
86 PRI.pdfSw = reshape(PRI.pdfSw,size(AA,1),size(AA,2));
87 PRI.pdfphi = reshape(PRI.pdfphi,size(AA,1),size(AA,2));
88
89 %------------------------
90 %  Error distributions
91 %------------------------
92
93 muErrlogRv = 0; % Mean error for logRv
94 muErrVp = 0; % Mean error for Vp
95 stdErrlogRv = 0.2; % Standard deviation logRv
96 stdErrVp = 50; % Standard deviation Vp
97 MLH.stdErrM1 = stdErrlogRv;
98 MLH.stdErrM2 = stdErrVp;
99
100 %---------------------------------------
101 %  Compute likelihoods and posteriors
102 %---------------------------------------
103
104 % Output struct (Multi Geophysical Inversion):
105 MGI.nx = SatPor.nx; MGI.nz = SatPor.nz; % Puts input struct (nx, nz, x and ...
       z) into output struct
106 MGI.x = SatPor.x;  MGI.z  = SatPor.z;
107 MGI.muSw = zeros(MGI.nz,MGI.nx); % Mean of Sw initialised with zeros
108 MGI.mapSw = zeros(MGI.nz,MGI.nx); % Map of Sw initialised with zeros
109 MGI.sigSw = zeros(MGI.nz,MGI.nx); % Std.dev of Sw initialised with zeros
110 MGI.label = 'Water saturation'; % Label output struct
111 MGI.muphi = zeros(MGI.nz,MGI.nx);
112 MGI.mapphi = zeros(MGI.nz,MGI.nx);
113 MGI.sigphi = zeros(MGI.nz,MGI.nx);
114 MGI.label = 'Porosity'; % Label output struct
115
116 % Number of data and model types:
```

```
117 DD.nd = 2; % New mesh DD
118
119 % Outer loop over depth
120 for kk = 1:SatPor.nz
121 DD.d1 = SatPor.logRv(kk,:); % logRv
122 DD.d2 = SatPor.Vp(kk,:); % Vp
123 DD.n = SatPor.nx;
124
125 for jj=1:DD.n
126     % Calculate maximum likelihoods
127     MLH.pdfM1 = mvnpdf((MC.logRv)'-DD.d1(jj),0,MLH.stdErrM1^2); % logRv
128     MLH.pdfM2 = mvnpdf((MC.Vp)'-DD.d2(jj),0,MLH.stdErrM2^2); % Vp
129
130     if     ktest == 1 % logRv
131        MLH.pdfM1 = reshape(MLH.pdfM1,size(AA,1),size(AA,2));
132        MLH.pdfAll = MLH.pdfM1;
133     elseif ktest == 2 % Vp
134        MLH.pdfM2 = reshape(MLH.pdfM2,size(AA,1),size(AA,2));
135        MLH.pdfAll = MLH.pdfM2;
136     elseif ktest == 3 % logRv and Vp
137        MLH.pdfM1 = reshape(MLH.pdfM1,size(AA,1),size(AA,2));
138        MLH.pdfM2 = reshape(MLH.pdfM2,size(AA,1),size(AA,2));
139        MLH.pdfAll = MLH.pdfM1.*MLH.pdfM2;
140     end % if
141
142     % Normalize MLH
143     rn = MC.dSw*MC.dphi*sum(sum(MLH.pdfAll));
144     MLH.pdfAll = MLH.pdfAll/rn;
145
146     % Posterior distribution
147     POST.pdf = PRI.pdfSw.*PRI.pdfphi.*MLH.pdfAll;
148     rn = MC.dSw*MC.dphi*sum(sum(POST.pdf));
149     POST.pdf = POST.pdf/rn;
150
151     % Compute mean, map and variance
152     POST.muSw(jj) = sum(sum(AA.*POST.pdf))*MC.dSw*MC.dphi; % Mean for Sw
```

```
153     POST.muphi(jj) = sum(sum(BB.*POST.pdf))*MC.dSw*MC.dphi; % Mean for phi
154     maxVal = max(max(POST.pdf)); % MAP
155     [indX,indY] = find(POST.pdf == maxVal);
156     POST.mapSw(jj) = AA(indX,indY);
157     POST.mapphi(jj) = BB(indX,indY);
158     POST.varSw(jj) = ...
            sum(sum(((AA-POST.muSw(jj)).^2).*POST.pdf))*MC.dSw*MC.dphi; % ...
            Variance for Sw
159     POST.varphi(jj) = ...
            sum(sum(((BB-POST.muphi(jj)).^2).*POST.pdf))*MC.dSw*MC.dphi; % ...
            Variance for phi
160     POST.stdSw(jj) = sqrt(POST.varSw(jj)); % Convert to standard deviation ...
            for Sw
161     POST.stdphi(jj) = sqrt(POST.varphi(jj)); % Convert to standard ...
            deviation for phi
162
163     %jjc = 21; kkc = 17; jf0 = 600; % Choose a point outside the reservoir
164     jjc = 21; kkc = 34; jf0 = 700; % Choose a point in the reservoir
165     if(jj==jjc & kk==kkc)
166        MGI.pdfPostSw = sum(POST.pdf,1)*MC.dphi;
167        MGI.pdfPriSw = sum(PRI.pdfSw,1)*MC.dphi;
168        MGI.pdfPostphi = sum(POST.pdf,2)*MC.dSw;
169        MGI.pdfPriphi = sum(PRI.pdfphi,2)*MC.dSw;
170        MGI.pdfMLHm1_Sw = sum(MLH.pdfM1,1)*MC.dphi;
171        MGI.pdfMLHm2_Sw = sum(MLH.pdfM2,1)*MC.dphi;
172        MGI.pdfMLHm1_phi = sum(MLH.pdfM1,2)*MC.dSw;
173        MGI.pdfMLHm2_phi = sum(MLH.pdfM2,2)*MC.dSw;
174        MGI.pdfMLH_Sw = sum(MLH.pdfAll,1)*MC.dphi;
175        MGI.pdfMLH_phi = sum(MLH.pdfAll,2)*MC.dSw;
176        MGI.pdfPOST = POST.pdf;
177        MGI.pdfMLHm1 = MLH.pdfM1;
178        MGI.pdfMLHm2 = MLH.pdfM2;
179        MGI.pdfMLH = MLH.pdfAll;
180        MGI.pdfPri = PRI.pdfSw.*PRI.pdfphi;
181        MGI.xc = MGI.x(jjc);
182        MGI.zc = MGI.z(kkc);
```

```
183         MGI.Swtrue = SatPor.Sw(kkc,jjc);
184         MGI.phitrue = SatPor.phi(kkc,jjc);
185     end % if
186 end % for
187 
188 % Some output parameters
189 MGI.muSw(kk,:) = POST.muSw;
190 MGI.mapSw(kk,:) = POST.mapSw;
191 MGI.stdSw(kk,:) = POST.stdSw;
192 MGI.muphi(kk,:) = POST.muphi;
193 MGI.mapphi(kk,:) = POST.mapphi;
194 MGI.stdphi(kk,:) = POST.stdphi;
195 end % for
```

C.2 Blocking of well logs

Function for blocking of well logs.

```
1  function [ data2 ] = blockLog( z1, data1, z2 )
2  %
3  %  data2 = blockLog( z1, data1, z2 )
4  %
5  %  Purpose: Block a log curve
6  %
7  %  Input:
8  %       z1    : Input log sample depthw
9  %       data1: Input log sample values
10 %       z2    : Output blocked log sample depthw
11 %
12 %  Output:
13 %       data2: Output blocked log sample values
14 
15 %--- Allocate and initiate:
16 data2 = nan(size(z2));
```

```
17
18 %--- First output sample:
19 jj=1;
20 zfw = (z2(jj+1)+z2(jj))/2;
21 ind = find( z1≤zfw );
22 rwrk = data1(ind);
23 ind2 = find(¬isnan(rwrk));
24 data2(jj) = mean(rwrk(ind2));
25
26 %--- Loop over 2 to nz-1:
27 for jj=2:length(z2)-1
28    zbw = (z2(jj)+z2(jj-1))/2;
29    zfw = (z2(jj+1)+z2(jj))/2;
30    ind = find( z1>zbw & z1≤zfw );
31    rwrk = data1(ind);
32    ind2 = find(¬isnan(rwrk));
33    data2(jj) = mean(rwrk(ind2));
34 end
35
36 %--- Last output sample:
37 jj=length(z2);
38 zbw = (z2(jj)+z2(jj-1))/2;
39 ind = find( z1>zbw );
40 rwrk = data1(ind);
41 ind2 = find(¬isnan(rwrk));
42 data2(jj) = mean(rwrk(ind2));
```

C.3 Rock-physics calibration

Rock-physics calibration for the studied wells.

```
%  Try to combine Han model with Gassmann fluid substitution
%  Calibration to Skrugard, Havis and 7219/9-1T2

clear all; % Delete everything
close all; % Close everything

% Real well logs from .mat files
load Wells_Lasfiles

dzBlock = 25; % Block length [m]
kblock = 1; % Block regular
%kblock = 2; % Block averaged on formations

%----------------------------
%  Get some more log curves
%----------------------------

jj=1; % 7219/9-1T2 (old dry well)
WL(jj).zsf = 356; % Water depth
WL(jj).elev = 23; % Kelly bushing
WL(jj).tvdss = WR(jj).wlog.curves(:,2); % True Vertical Depth measured ...
    from Mean Sea Level
WL(jj).lfp_rhob_b = 1e3*WR(jj).wlog.curves(:,75); % rho bulk brine
WL(jj).lfp_vp_b = WR(jj).wlog.curves(:,149); % vp brine
WL(jj).lfp_vs_b = WR(jj).wlog.curves(:,167); % vs brine

jj=2; % 7220/7-1 (Havis)
WL(jj).zsf = 385; % Water depth
WL(jj).elev = 40; % Kelly bushing
WL(jj).tvdss = WR(jj).wlog.curves(:,182); % True Vertical Depth measured ...
    from Mean Sea Level
```

```
30 WL(jj).lfp_rhob_b = 1e3*WR(jj).wlog.curves(:,75); % rho bulk brine
31 WL(jj).lfp_vp_b = WR(jj).wlog.curves(:,149); % vp brine
32 WL(jj).lfp_vs_b = WR(jj).wlog.curves(:,167); % vs brine
33
34 jj=3; % 7220/8-1 (Skrugard)
35 WL(jj).zsf = 373; % Water depth
36 WL(jj).elev = 23; % Kelly bushing
37 WL(jj).tvdss = WR(jj).wlog.curves(:,2); % True Vertical Depth measured ...
       from Mean Sea Level
38 WL(jj).lfp_rhob_b = 1e3*WR(jj).wlog.curves(:,71); % rho bulk brine
39 WL(jj).lfp_vp_b = WR(jj).wlog.curves(:,145); % vp brine
40 WL(jj).lfp_vs_b = WR(jj).wlog.curves(:,163); % vs brine
41
42 %--------------------
43 %  Some well tops
44 %--------------------
45
46 jj = 1; % 7219/9-1T2 (old dry well) (Measured depth (MD))
47 WL(jj).Tops.tvd = [483, 1467, 1893, 1951, 2062, 2206, 2250] - WL(jj).elev;
48 WL(jj).Tops.name = {'Top Torsk','Top Kolmule','Top Hekkingen','Top ...
       St ','Top Nordmela','Top Tub en','Top Fruholmen'};
49
50 jj = 2; % Havis (True vertical depth (TVD))
51 WL(jj).Tops.tvd = [445, 1275, 1700, 1741, 1818, 1983, 2090];
52 WL(jj).Tops.name = {'Top Torsk','Top Kolmule','Top Hekkingen','Top ...
       St ','Top Nordmela','Top Tub en','Top Fruholmen'};
53
54 jj = 3; % Skrugard (Measured depth (MD))
55 WL(jj).Tops.tvd = [455, 1013, 1252, 1275, 1353, 1510, 1628] - WL(jj).elev;
56 WL(jj).Tops.name = {'Top Torsk','Top Kolmule','Top Fuglen','Top St ','Top ...
       Nordmela','Top Tub en','Top Fruholmen'};
57
58 for jj=1:length(WL)
59    WL(jj).lfp_logrt = log10(WL(jj).lfp_rt); % logRt
60 end
61
```

```
%---------------------
%  Block more logs
%---------------------

for jj=1:length(WL)
   if     (kblock==1)
      WB(jj).tvd = 1000:dzBlock:2200; % Regular sampling
   elseif (kblock==2)
      WB(jj).tvd = WL(jj).Tops.tvd + [diff(WL(jj).Tops.tvd),0]/2; % ...
         Average over formations
   end

   WB(jj).depth = WB(jj).tvd; % Depth
   WB(jj).zsf = WL(jj).zsf; % Water depth
   WB(jj).lfp_phit = blockLog(WL(jj).tvd,WL(jj).lfp_phit,WB(jj).tvd); % ...
      Total porosity
   WB(jj).lfp_sgt = blockLog(WL(jj).tvd,WL(jj).lfp_sgt,WB(jj).tvd); % Gas ...
      saturation total
   WB(jj).lfp_sot = blockLog(WL(jj).tvd,WL(jj).lfp_sot,WB(jj).tvd); % Oil ...
      saturation total
   WB(jj).lfp_swt = 1 - WB(jj).lfp_sgt - WB(jj).lfp_sot; % Water ...
      saturation total
   WB(jj).lfp_vp_v = blockLog(WL(jj).tvd,WL(jj).lfp_vp_v,WB(jj).tvd); % ...
      P-wave velocity virgin
   WB(jj).lfp_vs_v = blockLog(WL(jj).tvd,WL(jj).lfp_vs_v,WB(jj).tvd); % ...
      S-wave velocity virgin
   WB(jj).lfp_rhob_v = blockLog(WL(jj).tvd,WL(jj).lfp_rhob_v,WB(jj).tvd); ...
      % Bulk density virgin
   WB(jj).lfp_vp_b = blockLog(WL(jj).tvd,WL(jj).lfp_vp_b,WB(jj).tvd); % ...
      P-wave velocity brine
   WB(jj).lfp_vs_b = blockLog(WL(jj).tvd,WL(jj).lfp_vs_b,WB(jj).tvd); % ...
      S-wave velocity brine
   WB(jj).lfp_rhob_b = blockLog(WL(jj).tvd,WL(jj).lfp_rhob_b,WB(jj).tvd); ...
      % Bulk density brine
   WB(jj).lfp_logrt = blockLog(WL(jj).tvd,WL(jj).lfp_logrt,WB(jj).tvd); % ...
      log true resistivity
```

```
86    WB(jj).lfp_rt = blockLog(WL(jj).tvd,WL(jj).lfp_rt,WB(jj).tvd); % True ...
          resistivity
87    WB(jj).vcl = blockLog(WL(jj).tvd,WL(jj).vcl,WB(jj).tvd); % Clay volume
88    WB(jj).Tops = WL(jj).Tops; % Well tops
89    WB(jj).name = WL(jj).name; % Well names
90
91    % Remove the nans
92    ind = find(isnan(WB(jj).lfp_vp_v)); WB(jj).lfp_vp_v(ind) = 6000;
93    ind = find(isnan(WB(jj).lfp_rhob_v)); WB(jj).lfp_rhob_v(ind) = 3000;
94    ind = find(isnan(WB(jj).lfp_rt)); WB(jj).lfp_rt(ind) = 1;
95    ind = find(isnan(WB(jj).lfp_logrt)); WB(jj).lfp_logrt(ind) = 0;
96 end
97
98 %-------------------------------
99 %  Han-Gassmann-Archie model
100 %-------------------------------
101
102 for jj=1:length(WL)
103    Sg = WL(jj).lfp_sgt; So = WL(jj).lfp_sot; % Virgin case
104    %So = zeros(size(WL(jj).lfp_sot)); Sg = zeros(size(WL(jj).lfp_sot)); % ...
          Brine case
105    cec = zeros(size(WL(jj).vcl)); % Cation exchange capacity
106    zzz = WL(jj).tvd-WL(jj).zsf; % Depth below seabed
107    [ WL(jj).synt_logrt, WL(jj).synt_vp, WL(jj).synt_vs, WL(jj).synt_rho] = ...
          RockPhysSeisEMsimp(So,Sg,WL(jj).lfp_phit,WL(jj).vcl,cec,zzz);
108
109    Sg = WB(jj).lfp_sgt; So = WB(jj).lfp_sot; % Virgin case
110    %So = zeros(size(WB(jj).lfp_sot)); Sg = zeros(size(WB(jj).lfp_sot)); % ...
          Brine case
111    cec = zeros(size(WB(jj).vcl)); % Cation exchange capacity
112    zz2 = WB(jj).tvd-WB(jj).zsf; % Depth below seabed
113    [ WB(jj).synt_logrt, WB(jj).synt_vp, WB(jj).synt_vs, WB(jj).synt_rho] = ...
          RockPhysSeisEMsimp(So,Sg,WB(jj).lfp_phit,WB(jj).vcl,cec,zz2);
114 end % for
115
116 %--------------
```

```
%  Save logs
%--------------

save Wells_WithAllLogs WL
if     kblock == 1
   save Wells_Blocked_Regular WB
elseif kblock == 2
   save Wells_Blocked_Formations WB
end
```

C.4 Well log data

C.4.1 Inversion of well logs

Inversion of the well logs.

```
%  Inversion of well logs:
%  Calculating Sw and phi from logRv, Vp and rho

clear all; % Delete everything
close all; % Close everything

%--------------------
%  Load the inputs
%--------------------

kblock = 1; % Block regular
%kblock = 2; % Block averaged on formations

if kblock == 1 % Block regular
   load Wells_Blocked_Regular
elseif kblock == 2 % Block averaged on formations
   load Wells_Blocked_Formations
end % if
```

```
19
20 %---------
21 %  Tests
22 %---------
23
24 % Relevant for joint inversion
25 % ktest = 1; % Use Rv only
26 % ktest = 2; % Use Vp only
27 %ktest = 3; % Use Vp and Rv
28 ktest = 4; % Use Vp, Rv and rho
29
30 UP.ktest = ktest; % Put ktest into struct
31 disp(strcat('ktest=',num2str(ktest))); % Write to the screen which test
32
33 %------------------------------
34 %  Prior for water saturation
35 %------------------------------
36
37 PRI.muSw = 0.9; % Prior mean for Sw
38 PRI.stdSw = 0.3; % Prior std.dev for Sw
39
40 %----------------------
41 %  Prior for porosity
42 %----------------------
43
44 PRI.muphi = 0.2; % Prior mean for phi
45 PRI.stdphi = 0.3; % Prior std.dev for phi
46
47 %----------------------
48 %  Error distributions
49 %----------------------
50
51 MC.muErrlogRv = 0; % Mean error logRv
52 MC.muErrVp = 0; % Mean error Vp
53 MC.muErrRho = 0; % Mean error rho
54 MC.sigErrlogRv = 0.5; % Standard deviation logRv
```

```
55 MC.sigErrVp = 150; % Standard deviation Vp
56 MC.sigErrRho = 50; % Standard deviation rho
57
58 %--------------------------------------
59 %  Compute likelihoods and posteriors
60 %--------------------------------------
61
62 for kk=1:length(WB)
63    ind = find(isnan(WB(kk).vcl)); WB(kk).vcl(ind) = 0.5; % Remove the NaN's
64    disp(['Analyzing well ',WB(kk).name]); % Write to screen which well is ...
          being analyzed
65    dz = WB(kk).tvd(2) - WB(kk).tvd(1); % Depth increment
66
67    % Number of data and model types
68    DD.vcl = WB(kk).vcl; % Take clay content into account
69    DD.vcl = min(DD.vcl,0.6); % Max Vcl is set to 0.6
70    DD.z = WB(kk).tvd-WB(kk).zsf; % Calculate the depth from the seabed
71    DD.n = length(WB(kk).tvd); % New mesh DD
72
73    if     ktest==1
74       DD.d1 = log10(WB(kk).lfp_rt); % logRv
75    elseif ktest==2
76       DD.d2 = WB(kk).lfp_vp_v;      % Vp
77    elseif ktest==3
78       DD.d1 = log10(WB(kk).lfp_rt); % logRv
79       DD.d2 = WB(kk).lfp_vp_v;      % Vp
80    elseif ktest==4
81       DD.d1 = log10(WB(kk).lfp_rt); % logRv
82       DD.d2 = WB(kk).lfp_vp_v;      % Vp
83       DD.d4 = WB(kk).lfp_rhob_v;    % rho
84    end % if
85
86    disp('%-- Bayesian calculations') % Write to screen
87    [WP(kk).POST] = inversion(DD,MC,PRI,UP); % Posterior distributions ...
          (inversion itself)
88
```

```
89      % Input to the rock physics model
90      Sw = WP(kk).POST.mapSw;
91      So = 0.5*(1-WP(kk).POST.mapSw); % 50% of HC is oil
92      Sg = 0.5*(1-WP(kk).POST.mapSw); % 50% of HC is gas
93      phi = WP(kk).POST.mapphi;
94      vcl = DD.vcl;
95      CEC = zeros(size(phi));
96
97      % Do the forward modeling
98      [ WP(kk).synt_logrt, WP(kk).synt_vp, WP(kk).synt_vs, WP(kk).synt_rho] = ...
            RockPhysSeisEMsimp(So,Sg,phi,vcl,CEC,DD.z); % Calculate the models ...
            of log resistivity, vp and rho.
99  end % for
100     disp('%-- Finished Bayesian calculations') % Write to screen
```

C.4.2 Forward modeling well logs and maps

Forward modeling for well logs and maps.

```
1   function [logRv, vp, vs, rho] = RockPhysSeisEMsimp(So,Sg,phi,vcl,CEC,zzz)
2   %  Simplified seismic part, using combined Han model and
3   %  Gassmann fluid substitution.
4
5   %  Inputs: arrays should be same size or a scalar
6   %      So  : Oil saturation
7   %      Sg  : Gas saturation
8   %      phi : Porosity
9   %      vcl : Clay fraction
10  %      CEC : Cation exchange capacity
11  %      zzz : Depth below seabed
12
13  %  Outputs:
14  %      logRv : Log10(Resistivity)
15  %      Vp    : P-wave velocity
16  %      Vs    : S-wave velocity
```

```
%     rho   : Density

%-------------------------------------------------------
%   Set some fixed parameters for mineral sand fluids
%-------------------------------------------------------

% Archie parameters (fixed)
a = 1; % Turtousity factor
R_water = 0.06; % Water resistivity, from LFP_RW
n = 2.0; % Saturation exponent
m = 1.8; % Porosity exponent

% Waxman-Smits parameters (fixed)
%R_water = 0.30; % Water resistivity
sig_water = 1/R_water; % Water conductivity
B_waxman = 4.6*(1-0.6*exp((-sig_water)/1.3)); % Equivalent conductance per ...
    cation
rho_0 = 2700; % Mineral grain density
%CEC = 30; % Cation exchange capacity

%---------------------------------------
%   Fluid with partial/mixed saturation
%---------------------------------------

Sw = 1 - So - Sg; % Water saturation
Sw = max(Sw,0.001); % Make sure we dont divide by zero in Archie's law

%-------------------------------------------
%   Archie equation
%-------------------------------------------

R_sat = a*R_water./(phi.^m.*Sw.^n); % Resistivity saturated rock
logRv = log10(R_sat); % Vertical resistivity (log)

%----------------
%   Waxman-Smits
```

```
52 %-----------------
53
54 %F = a*phi.^(-m); % Formation factor
55 %Qv = (CEC.*(1-phi).*rho_0)./phi; % Charge per unit pore volume ...
       (indicative of shaliness of a formation)
56 %sig = (1./F).*(sig_water + (B_waxman.*Qv)); % Conductivity
57 %logRv = log10(1./sig); % Log vertical resistivity
58
59 %------------------------
60 %   Gassmann parameters
61 %------------------------
62
63 % Matrix (quartz)
64 rhoQz = 2640; % Density quartz.
65 KQz = 38e9; % Bulk modulus quartz.
66 muQz = 44e9; % Shear modulus quartz
67 KCl = 20.9e9; % Bulk modulus clay
68 muCl = 6.85e9; % Shear modulus clay
69
70 Biot = 0.60; % Biot coefficient (Quartzitic sandstone)
71 pscl = 1.00;
72 sscl = 0.45;
73 rho_matrix = rhoQz; % Density matrix
74 mu_matrix = muQz; % Shear modulus matrix
75 K_matrix = KQz; % Bulk modulus matrix
76
77 % Gassmann parameters (fluids)
78 K_gas = 0.83e9; % Tuning
79 K_oil = 1.200e9; % Just guessing
80 K_water = 2.93e9; % From LFP_KFLW
81 rho_gas = 150.5; % Gas density from LFP_RHOG
82 rho_oil = 800; % Oil density
83 rho_water = 1061; % Water density from LFP_RHOW
84
85 %-------------
86 %  Density
```

```
87 %-------------
88
89 rho_fluid = Sw.*rho_water + So.*rho_oil + Sg.*rho_gas; % Fluid density
90 rho_sat = (1-phi).*rho_matrix + phi.*rho_fluid; % Density of saturated rock
91 rho = rho_sat; % Density returned by function
92
93 %-----------------------------------------
94 %   Han model for Vp and Vs (brine filled)
95 %-----------------------------------------
96
97 % Data from Han
98 sigHan = [5, 10, 20, 30, 40, 100]; % Effective stress
99 ApHan  = [5.26, 5.39, 5.49, 5.55, 5.59, 5.59];
100 BpHan  = [7.08, 7.08, 6.94, 6.96, 6.93, 6.93];
101 CpHan  = [2.02, 2.13, 2.17, 2.18, 2.18, 2.18];
102 AsHan  = [3.16, 3.29, 3.39, 3.47, 3.52, 3.52];
103 BsHan  = [4.77, 4.73, 4.73, 4.84, 4.92, 4.92];
104 CsHan  = [1.64, 1.74, 1.81, 1.87, 1.89, 1.89];
105
106 % Approximate effective stress
107 gz = 9.82; % Acceleration of gravity
108 rhoAvg = 2300; % Approx avg bulk density
109 nn = Biot; % Biot coefficient: 0<nn<1
110 sigEff = 1e-6*gz*(rhoAvg-nn*rho_water)*zzz; % Effective stress [MPa]
111
112 % Interpolate:
113 Ap = 1.00e3*interp1(sigHan,ApHan,sigEff);
114 Bp = 1.00e3*interp1(sigHan,BpHan,sigEff);
115 Cp = 1.00e3*interp1(sigHan,CpHan,sigEff);
116 As = 1.00e3*interp1(sigHan,AsHan,sigEff);
117 Bs = 1.00e3*interp1(sigHan,BsHan,sigEff);
118 Cs = 1.00e3*interp1(sigHan,CsHan,sigEff);
119
120 % Velocities from Han model
121 vpHan = Ap - Bp.*phi - Cp.*vcl;
122 vsHan = As - Bs.*phi - Cs.*vcl;
```

```
123
124 % Water saturated density
125 rhoHan = (1-phi).*rho_matrix + phi.*rho_water;
126
127 %-----------------------------------------------
128 %   Gassmann fluid substitution around Gassmann
129 %-----------------------------------------------
130
131 % Temperature effect on shear modulus
132 Tg = 38e-3; % Thermal gradient
133 aa = 18.8;  % Tuning parameter
134 stemp = (1-aa./(Tg*zzz));
135 mu_dry = (1-Biot)*stemp*mu_matrix; % Shear modulus dry
136
137 % Bulk properties for brine filled rock (from Han model)
138 Ks1 = rhoHan.*(vpHan.^2 - (4/3)*vsHan.^2);
139 Kf1 = K_water;
140
141 % Bulk modulus of HC
142 Kf2 = 1./(Sg./K_gas + So./K_oil + Sw./K_water); % Uniform saturation
143 %Kf2 = Sg.*K_gas + So.*K_oil + Sw.*K_water; % Patchy saturation
144
145 % Fluid substitution
146 vs = sqrt(mu_dry./rho); % S-wave velocity
147 a1 = Ks1./(K_matrix-Ks1);
148 f1 = Kf1./(K_matrix-Kf1);
149 f2 = Kf2./(K_matrix-Kf2);
150 gg = (a1+(1./phi).*(f2-f1));
151 Ks2 = (gg./(1+gg)).*K_matrix;
152 vp = sqrt((Ks2 + (4/3)*mu_dry)./rho); % P-wave velocity
153 end % function
```

C.4.3 Inversion

Inversion code for well logs and maps.

```
function [POST] = inversion(DD,MC,PRI,UP)
%
%  Inversion code
%  Bayesian inversion of Rv, Vp (and density)
%
%  Input:
%      DD: Blocked well log data
%      MC: Error distributions
%     PRI: Prior (mean and std.dev) for water saturation and porosity
%      UP: Which test
%
%  Output:
%    POST: Posterior distribution

% ---------------------
%    Water saturation
% ---------------------

Swmin = 0.01; % Minimum Sw
Swmax = 1; % Maximum Sw
MC.nSw = 50; % Number of elements for Sw
MC.dSw = (Swmax-Swmin)/(MC.nSw-1); % Increment length
MC.Sw = [Swmin:MC.dSw:Swmin+(MC.nSw-1)*MC.dSw]'; % Sw

% --------------
%    Porosity
% --------------

phimin = 0.01; % Minimum phi
phimax = 0.5; % Maximum phi
MC.nphi = 50; % Number of elements for phi
MC.dphi = (phimax-phimin)/(MC.nphi-1); % Increment length
```

```
33 MC.phi = [phimin:MC.dphi:phimin+(MC.nphi-1)*MC.dphi]'; % phi
34
35 % Make grid of all model parameter combinations (not only pairwise)
36 [AA,BB]=meshgrid(MC.Sw,MC.phi);
37 aa=reshape(AA,size(AA,1)*size(AA,2),1); % Make a vector
38 bb=reshape(BB,size(BB,1)*size(BB,2),1); % Make a vector
39 MC.Sw=aa;
40 MC.phi=bb;
41 MC.So = 0.5*(1-MC.Sw); % 50% oil
42 MC.Sg = 0.5*(1-MC.Sw); % 50% gas
43
44 %---------------
45 %   Prior pdf
46 %---------------
47
48 PRI.pdfSw = mvnpdf(MC.Sw,PRI.muSw,PRI.stdSw^2); % Multivariate normal ...
      probability density function for Sw
49 PRI.pdfphi = mvnpdf(MC.phi,PRI.muphi,PRI.stdphi^2); % Multivariate normal ...
      probability density function for phi
50
51 % Reshape pdf back to grid shape
52 PRI.pdfSw = reshape(PRI.pdfSw,size(AA,1),size(AA,2));
53 PRI.pdfphi = reshape(PRI.pdfphi,size(AA,1),size(AA,2));
54
55 %-------------------------
56 %   Error distributions
57 %-------------------------
58
59 MLH.stdErrM1 = MC.sigErrlogRv; % MLH mesh with std.dev of Model 1 (logRv)
60 MLH.stdErrM2 = MC.sigErrVp; % MLH mesh with std.dev of Model 2 (Vp)
61 %MLH.stdErrM4 = MC.sigErrRho; % MLH mesh with std.dev of Model 4 (density)
62
63 %--------------------------------------
64 %   Compute likelihoods and posteriors
65 %--------------------------------------
66
```

```
indCalc = []; % Create an empty vector
POST.mapSw = nan(size(DD.d1)); % To get the right size of the vector
POST.mapphi = nan(size(DD.d1)); % To get the right size of the vector

for jj = 1:DD.n

    MC.vcl = 0.5*DD.vcl(jj)*ones(size(MC.phi)); % Clay content
    %MC.CEC = zeros(size(MC.phi)); % Cation exchange capacity
    MC.zzz = DD.z(jj)*ones(size(MC.phi)); % Depth below seabed

    % Do the forward modeling
    [ MC.m1, MC.m2, MC.m3, MC.m4 ] = ...
        RockPhysSeisEMsimp(MC.So,MC.Sg,MC.phi,MC.vcl,MC.CEC,MC.zzz);

    % Calculate (maximum)likelihoods
    MLH.pdfM1 = mvnpdf((MC.m1)-DD.d1(jj),0,MLH.stdErrM1^2); % logRv
    MLH.pdfM2 = mvnpdf((MC.m2)-DD.d2(jj),0,MLH.stdErrM2^2); % Vp
    %MLH.pdfM4 = mvnpdf((MC.m4)-DD.d4(jj),0,MLH.stdErrM4^2); % Density
    MLH.pdfAll = ones(size(PRI.pdfSw));

    if isfield(DD,'d1')
       MLH.pdfM1 = mvnpdf((MC.m1)-DD.d1(jj),0,MLH.stdErrM1^2); % logRv
       MLH.pdfM1 = reshape(MLH.pdfM1,size(AA,1),size(AA,2));
       MLH.pdfAll = MLH.pdfAll.*MLH.pdfM1;
    end

    if isfield(DD,'d2')
       MLH.pdfM2 = mvnpdf((MC.m2)-DD.d2(jj),0,MLH.stdErrM2^2); % Vp
       MLH.pdfM2 = reshape(MLH.pdfM2,size(AA,1),size(AA,2));
       MLH.pdfAll = MLH.pdfAll.*MLH.pdfM2;
    end

    if isfield(DD,'d4')
       MLH.pdfM4 = mvnpdf((MC.m4)-DD.d4(jj),0,MLH.stdErrM4^2); % Density
       MLH.pdfM4 = reshape(MLH.pdfM4,size(AA,1),size(AA,2));
       MLH.pdfAll = MLH.pdfAll.*MLH.pdfM4;
```

```
102     end
103
104     % Normalize MLH
105     rn = MC.dSw*MC.dphi*sum(sum(MLH.pdfAll));
106     MLH.pdfAll = MLH.pdfAll/rn;
107
108     % Posterior distribution
109     POST.pdf = PRI.pdfSw.*PRI.pdfphi.*MLH.pdfAll;
110     rn = MC.dSw*MC.dphi*sum(sum(POST.pdf));
111     POST.pdf = POST.pdf/rn;
112
113     % Compute mean, map and variance
114     POST.muSw(jj) = sum(sum(AA.*POST.pdf))*MC.dSw*MC.dphi; % Mean for Sw
115     POST.muphi(jj) = sum(sum(BB.*POST.pdf))*MC.dSw*MC.dphi; % Mean for phi
116     maxVal = max(max(POST.pdf)); % MAP
117     [indX,indY] = find(POST.pdf==maxVal,1,'first');
118     if (¬isempty(indX) & ¬isempty(indY))
119        POST.mapSw(jj) = AA(indX,indY);
120        POST.mapphi(jj) = BB(indX,indY);
121     end % if
122     POST.varSw(jj) = ...
           sum(sum(((AA-POST.muSw(jj)).^2).*POST.pdf))*MC.dSw*MC.dphi; % ...
           Variance for Sw
123     POST.varphi(jj) = ...
           sum(sum(((BB-POST.muphi(jj)).^2).*POST.pdf))*MC.dSw*MC.dphi; % ...
           Variance for phi
124     POST.stdSw(jj) = sqrt(POST.varSw(jj)); % Convert to standard deviation ...
           for Sw
125     POST.stdphi(jj) = sqrt(POST.varphi(jj)); % Convert to standard ...
           deviation for phi
126     POST.z = DD.z;
127
128    % Choose a point in the reservoir and outside
129     %jjc = 14; % Reservoir in Skrugard
130     jjc = 9; % Outside reservoir Skrugard
131     if(jj==jjc)
```

```
132         POST.pdfPostSw = sum(POST.pdf,1)*MC.dphi;
133         POST.pdfPriSw = sum(PRI.pdfSw,1)*MC.dphi;
134         POST.pdfPostphi = sum(POST.pdf,2)*MC.dSw;
135         POST.pdfPriphi = sum(PRI.pdfphi,2)*MC.dSw;
136         POST.pdfPri = PRI.pdfSw.*PRI.pdfphi;
137         POST.pdfMLH = MLH.pdfAll;
138         POST.pdfPOST = POST.pdf;
139         POST.Sw = MC.Sw;
140         POST.phi = MC.phi;
141         POST.zc = DD.z(jjc);
142     end % if
143 end % for
144 end % function
```

C.5 Map models

Inversion of the maps.

```
1  %  Inversion maps:
2  %  Calculating Sw and phi from logRv and Vp
3
4  clear all; % Delete everything
5  close all; % Close everything
6
7  load wells_las_test
8
9  % Load the input data
10 TopRealgrunnen = ...
       dlmread('Z:\Students\Sondre\MapTests\Surfaces_FirstPass\Z.xyz',' '); % ...
       Read the interpretation of top Realgrunnen
11 Seabed = dlmread(
12 'Z:\Students\Sondre\MapTests\Surfaces_FirstPass\seabed.xyz',' '); % Read ...
       seabed
13 Rv = dlmread(
```

```
'Z:\Students\Sondre\MapTests\Surfaces_ThirdPass\Rv_TRealg_200U_300D.xyz',' ...
    '); % Read Rv
Vp = dlmread(
'Z:\Students\Sondre\MapTests\Surfaces_ThirdPass\FWI_TRealg_50D.xyz',' '); ...
    % Read Vp FWI
X = Seabed(:,1); % Easting
Y = Seabed(:,2); % Northing
Z = TopRealgrunnen(:,3) - Seabed(:,3); % Burial depth
Rv = Rv(:,3); % Rv
VpX = Vp(:,1);
VpY = Vp(:,2);
indZero = find(Vp(:,3)~=0);
VpInt = scatteredInterpolant(Vp(indZero,1),Vp(indZero,2),Vp(indZero,3));
Vp = VpInt(X,Y);
Vp = Vp; % Vp

%---------
%  Tests
%---------

% Relevant for joint inversion
% ktest = 1; % Use logRv only
% ktest = 2; % Use Vp only
ktest = 3; % Use Vp and logRv

UP.ktest = ktest; % Put ktest into struct
disp(strcat('ktest=',num2str(ktest))); % Write to the screen which test we use

%--------------------------------
%  Prior for water saturation
%--------------------------------

PRI.muSw = 0.7; % Prior mean for Sw
PRI.stdSw = 0.5; % Prior std.dev for Sw

%-----------------------
```

```
%  Prior for porosity
%-----------------------

PRI.muphi = 0.2; % Prior mean for phi
PRI.stdphi = 0.2; % Prior std.dev for phi

%-------------------------
%  Error distributions
%-------------------------

MC.muErrlogRv = 0; % Mean error for logRv
MC.muErrVp = 0; % Mean error for Vp
MC.muErrRho = 0; % Mean error for rho
MC.sigErrlogRv = 0.8; % Std.dev error logRv
MC.sigErrVp = 300; % Std.dev error Vp
%MC.sigErrRho = 50; % Std.dev error rho

%--------------------------------------
%  Compute likelihoods and posteriors
%--------------------------------------

for kk=1:1 %length(WB)
   DD.z = Z; % Calculate the depth from the seabed
   DD.n = length(Z); %length(WB(kk).tvd); % New mesh DD
   DD.vcl = 0.15*ones(size(Z)); % Clay content
   vcl = DD.vcl;

   if     ktest==1
      DD.d1 = log10(Rv); % logRv
   elseif ktest==2
      DD.d2 = Vp; % Vp
   elseif ktest==3
      DD.d1 = log10(Rv); % logRv
      DD.d2 = Vp; % Vp
   end % if

```

```
84      disp('%-- Bayesian calculations') % Write to screen
85      [WP(kk).POST] = inversion(DD,MC,PRI,UP); % Posterior distributions
86
87      % Input to the rock physics model
88      Sw = WP(kk).POST.mapSw;
89      So = 0.5*(1-WP(kk).POST.mapSw); % 50% of HC is oil
90      Sg = 0.5*(1-WP(kk).POST.mapSw); % 50% of HC is gas
91      phi = WP(kk).POST.mapphi;
92      vcl = 0.15*ones(size(phi));
93      %CEC = zeros(size(phi));
94
95      % Do the forward modeling
96      [WP(kk).synt_logrt, WP(kk).synt_vp, WP(kk).synt_vs, WP(kk).synt_rho] = ...
            RockPhysSeisEMsimp(So,Sg,phi,vcl,CEC,DD.z); % Calculate the models ...
            of logRv, Vp and rho.
97  end
98  disp('%-- Finished Bayesian calculations') % Write to screen
```